Hierarchical Multiscale Modelling of CoCu Catalyst in CO Hydrogenation

Bridge the Gap between Microscopic and Mesoscopic Systems

Zur Erlangung des akademischen Grades eines
DOKTORS DER NATURWISSENSCHAFTEN
(Dr. rer. nat)

von der KIT-Fakultät für Chemie und Biowissenschaften
des Karlsruher Instituts für Technologie (KIT)

genehmigte
DISSERTATION
von

M.Eng. Shenjun Zha

1. Referent:	Prof. Dr. Felix Studt
2. Referent:	PD Dr. Sebastian Höfener
Tag der mündlichen Prüfung:	19.07.2022

Abstract

Heterogeneous catalysis, one cornerstone of modern society, gradually evolves to meet our demand for chemical solutions. Starting from the beginning of the nineteenth century, the discovery of new catalytic processes has never stopped, such as ammonia synthesis, catalytic cracking, polymerization, exhaust catalysis, etc. All these discoveries will not happen without the integration of underlying theories and trial-and-error experiments.

One of the most exciting changes in theoretical chemistry is the development of computational methods. With the dramatically developed computational hardware in the past two decades, computation nowadays allows the quantitative interpretation of the specific catalytic system. Computation in catalysis, the bridge between theory and experiment, reveals a similar trend as experimental investigations. Rather than the idealized catalyst surfaces and reaction conditions, more “operando” information is called to be provided from the computational perspective. As a result, many new computational techniques were developed, e.g., global optimization techniques, microkinetic simulations, machine learning based methods, and *ab initio* thermodynamics.

In this thesis, we thoroughly investigated the CoCu catalysts in CO hydrogenation. First, with the help of the machine learning based Monte Carlo method, large CoCu particles are allowed to be scrutinized directly, and the explicit Co@Cu core-shell structure was confirmed without compromise in accuracy. Afterwards, the interaction of intermediates with CoCu surfaces was quantified via global optimization. Based on the segregation direction of different intermediates, a fast prediction scheme for segregation preference was proposed. Second, using the microkinetic simulations, two fully segregated Cu/Co(111) and Co/Cu(111), namely the surfaces existing at the early and late stages of the reaction, are explored. The results indicate one type of active site with proper adsorption of CO will be adequate for the formation of C_2 oxygenates. Third, by using *ab initio* thermodynamics, the phase diagrams suggest a partially segregated CoCu surface with a high CO coverage during the reaction. On top of that, the quantitively consistent kinetic results were obtained from both mean-field theory (MFT) and kinetic Monte Carlo (kMC) simulations.

Kurzfassung

Die heterogene Katalyse stellt einen Grundpfeiler der modernen Gesellschaft dar und deckt nach und nach den Bedarf an chemischen Lösungen. Die Geschichte der Katalyse begann bereits im neunzehnten Jahrhundert und hat sich fortlaufend weiterentwickelt. Daraus entstanden unter anderem die Ammoniaksynthese, das katalytisches Cracking, die Polymerisation und die Abgaskatalyse. All diese Entdeckungen stützen sich auf theoretischem Hintergrundwissen und Trial-and Error-Experimenten.

Eine der aufregendsten Veränderungen in der theoretischen Chemie ist die Entwicklung der Rechenverfahren. Mit der dramatisch entwickelten Computerhardware in den letzten zwei Jahrzehnten ermöglichen sie heute die Berechnung und damit die quantitative Interpretation spezifischer katalytischen Systemen. Rechenverfahren in der Katalyse, die Brücke zwischen Theorie und Experiment, zeigen ähnliche Trends wie experimentelle Untersuchungen. Anstelle von idealisierten Katalysatoroberflächen und Reaktionsbedingungen stellet die rechnerische Perspektive eher „operando“-Informationen bereit. Infolgedessen wurden viele neue Techniken entwickelt, z. B. globale Optimierungstechniken, mikrokinetische Simulationen, auf maschinellem Lernen basierende Methoden und ab initio Thermodynamik.

In dieser Arbeit haben wir die CoCu-Katalysatoren für CO Hydrierung untersucht. Als erstes konnten große CoCu-Partikel zunächst mit Hilfe von auf maschinellem Lernen basierendem Monte Carlo-Methode ohne Kompromisse in der Genauigkeit untersucht werden und die Co@Cu-Kern-Schale Struktur direkt bestätigt werden. Zweitens wurde das Zusammenspiel von Zwischenprodukten mit den CoCu-Oberflächen über globale Optimierung quantifiziert. Basierend auf der Trennungsrichtung unterschiedlicher Zwischenprodukte wurde ein schnelles Vorhersageschema für die Segregationspräferenz vorgeschlagen. Danach wurden die zwei vollständig entmischten Cu/Co(111) und Co/Cu(111) Oberflächen, die bei Beginn und Ende der Reaktion bestehen, untersucht. Die Ergebnisse weisen auf einen einzigen Typ aktiven Zentrums mit geeigneter CO Adsorption für die Bildung von C_2-Oxygenaten hin. Drittens, durch die Verwendung von ab initio Thermodynamik, deuten die Phasendiagramme auf eine teilweise entmischte CoCu-Oberfläche mit hoher CO-Bedeckung während der Reaktion hin. Zudem waren die erhaltenen kinetischen Ergebnisse sowohl aus der Mean-Field-Theorie als auch aus der Monte-Carlo-Methode Simulationen quantitativ konsistent.

Contents

1. Introduction

1.1 CO as the Intermediate Resource

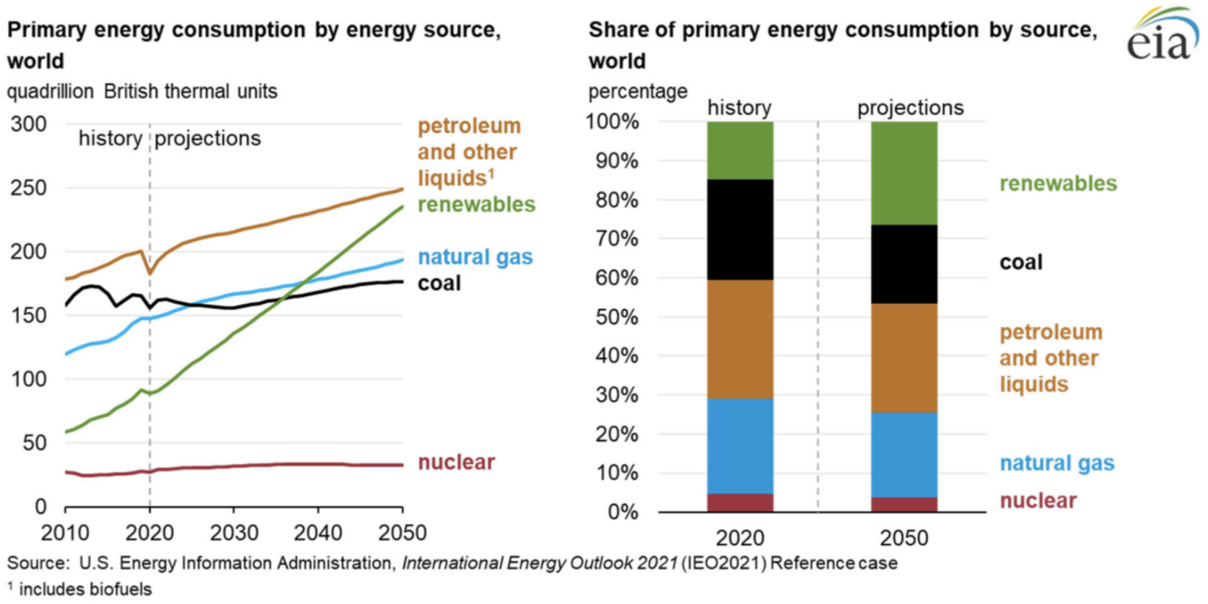

Source: U.S. Energy Information Administration, *International Energy Outlook 2021* (IEO2021) Reference case

¹ includes biofuels

Figure 1.1 Primary energy consumption by energy source worldwide. Image provided by Energy Information Administration.[1]

Energy, a cornerstone of modern society, powers the industrial, residential, commercial, and transportation end-user sectors. According to the report from U.S. Energy Information Administration, our society now is still heavily relying on fossil fuels (~81% in Figure 1.1). Although renewable energy consumption grows from ~15% to ~26% through the projection period, there is no end to reliance on fossil fuels in the near future (~70% in 2050). The huge concern that emission of greenhouse gas released by fossil fuels will still be lingering.[2] How to utilize fossil fuel efficiently and greenly will still be a major challenge for our generation.

Table 1.1 The production of syngas.

Process	Reaction	ΔH^{o}_{298} (kJ mol^{-1})
Steam reforming	$CH_4 + H_2O \rightleftharpoons CO + 3H_2$	+206
	$C_nH_m + nH_2O \rightleftharpoons nCO + \left(n + \frac{m}{2}\right) H_2$	> 0
Partial oxidation	$CH_4 + 0.5O_2 \rightleftharpoons CO + 2H_2$	-35.9
Water-gas shift reaction	$CO + H_2O \rightleftharpoons CO_2 + H_2$	-41

Syngas ($CO + H_2$), a crucial intermediate resource, offers some sustainable routes to utilize these fossil fuels. Syngas itself can be produced from natural gas, coal, oil residue, biomass, or virtually any hydrocarbon feedstocks by reacting with steam or oxygen.[3] The related reactions are steam reforming, partial oxidation, and gasification.[4] The steam reforming shown in Table 1.1 is a large-scale chemical process to produce hydrogenation. It is an endothermic reaction operating at high temperatures (up to 1000 °C) and moderate pressures (25-35 bar). Partial oxidation is an alternative to steam reforming to produce a smaller amount of hydrogen. The gasification of either biomass or coal is also a possible way to obtain syngas.

Table 1.2 The application of syngas.

Process	Reaction	ΔH^{o}_{298} (kJ mol^{-1})
Methanol synthesis	$CO + 2H_2 \rightleftharpoons CH_3OH$	-91
Fischer-Tropsch synthesis	$nCO + (2n + 1)H_2 \rightleftharpoons C_nH_{2n+2} + nH_2O$	
	$nCO + 2nH_2 \rightleftharpoons C_nH_{2n} + nH_2O$	

The chemical transformation of syngas is also versatile, including Fischer-Tropsch (FT) synthesis, methanol synthesis, higher alcohol synthesis, dimethyl ether synthesis, methanol to hydrocarbons, polyoxymethylene synthesis, and biological processes. The methanol synthesis shown in Table 1.2 is an exothermic reaction. The industrial process is operating at 50-100 bar and 500-550 K with a mixed $H_2/CO_2/CO$ (90:5:5) over $Cu/ZnO/Al_2O_3$ catalysts.[5] The FT synthesis is a highly exothermic reaction.[6] Iron and cobalt catalysts are typically used for this reaction.

1.2 The Synthesis of Higher Alcohol

Higher alcohols are important compounds with widespread applications in the chemical, pharmaceutical, and energy sectors. Currently, they are mainly produced by sugar fermentation (ethanol and isobutanol) or hydration of petroleum-derived alkenes (heavier alcohols). However, the direct synthesis from syngas would be a more environment-friendly, and economical alternative.

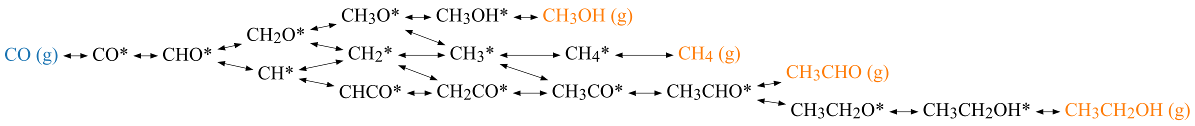

Figure 1.2 The reaction network from CO to methane, methanol, acetaldehyde, and ethanol.

To some extent, higher alcohol synthesis can be viewed as the combination of two competitions as shown in Figure 1.2.[7–12] The first one is between CH_XO* (CHO*, CH_2O*, or CH_3O*) hydrogenation and dissociation. The hydrogenation of CH_XO* leads to the production of CH_3OH(g), while the dissociation of CH_XO* provides the CH_X* intermediates (including CH*, CH_2*, or CH_3*) as the precursors to C_2 oxygenates. With the formation of CH_X* intermediates, they can accept the insertion of CO*, which leads to CH_XCO* (CHCO*, CH_2CO*, or CH_3CO). In the meantime, the hydrogenation of CH_X* will be the competitor of the insertion process. Once CH_XCO* intermediates have formed, the later hydrogenation to C_2 oxygenates (CH_3CHO (g) and CH_3CH_2OH (g)) is generally considered comparably feasible. Owing to the two existing competitions, bi-functionality of the catalyst is needed for higher alcohol synthesis, where one site is for CH_XO* dissociation and CO* insertion while the other one is for hydrogenation. Catalysts containing only one metal have rarely achieved a promising performance.

The catalysts for higher alcohol synthesis can be classified into four categories: Rh-based, Mo-based, modified FT synthesis, and modified methanol synthesis systems.[13] In general, the C_{2+} oxygenates yield can be ranked as modified FT synthesis catalysts > Mo-based catalysts ≈ Rh-based catalysts > modified methanol synthesis catalysts.[13]

1.2 CoCu alloy as Catalyst

Supported metal catalysts with varied sizes (from single atoms to clusters and nanoparticles) are among the most widely used catalysts with applications ranging from oxidation to hydrogenation reactions.[14] The latter are thought to play a key role in future renewable chemistry scenarios through the conversion of CO or CO_2 to methanol[15], hydrocarbons through the FT process[15,16], and higher alcohols[13]. Similarly, bimetallic alloys are extensively investigated as they often show advanced catalytic performance and can be seen as a compromise in terms of activity between the constituting metals. CuCo-based alloys for the synthesis of higher alcohols are such an example.

CoCu catalyst, a kind of modified FT synthesis catalyst, has been comprehensively investigated due to its low cost and high efficiency.[17–23] A metal with hydrogenation activity towards methanol as the simplest alcohol (Cu) is combined with a typical Fischer-Tropsch catalyst (Co) responsible for chain growth, pointing towards a dual-site mechanism.[13,24] Although this mechanism is generally accepted, the exact nature of the active site of CoCu catalysts on the atomic scale is still being intensely debated.[13,24] Part of the reason lies in the complex segregation behavior of this bimetallic alloy and its dependence on Cu:Co ratio, particle size, support as well as interaction with the gaseous environment (e.g. CO).

Plenty of experimental work has been carried out on CoCu catalysts, providing plentiful evidence about the CoCu structures. After activating in argon or H_2, Kruse et al. found the formation of Co@Cu core-shell structure showing a high alcohol selectivity in CO hydrogenation.[21] Somorjai et al. discovered the segregated CoCu particle after redox conditioning at 350 °C characterized by STEM/EDS phase-map.[25] However, when using $LaFeO_3$ as the support, the process of H_2 reduction leads to the Cu@Co core-shell structure and mixed CoCu structure, which has been shown in TEM micrographs.[19] The formation of Co@Cu[21] and Cu@Co[19] core-shell structures, as well as segregated and mixed CoCu structures[18] have all been observed experimentally.

The CoCu particles have also been extensively investigated in theoretical calculations with empirical interatomic potentials. Zhao et al. used genetic algorithm with a Gupta-type many-body potential to investigate the geometrical and magnetic properties of CoCu clusters with different CoCu ratios. Co@Cu icosahedral clusters were found, such as $Cu_{12}Co_1$, $Cu_{17}Co_2$, $Cu_{42}Co_{13}$,

$Cu_{92}Co_{55}$, $Cu_{54}Co_1$, $Cu_{69}Co_2$, and $Cu_{134}Co_{13}$.[26] Shim et al. utilized Monte Carlo simulation with a modified embedded atom method to explore the phase separation behavior of CoCu particles. After 500 step Monte Carlo steps, most Co atoms aggregated near the particle center.[27] Similar method was also utilized by Dzhurakhalov et al. and onion-like Co-Cu configurations are found, which can be tuned by monitoring the interplay between composition (5%, 20%, 30%, 50%, and 80% Co) and temperature (100 K, 300 K and 500 K).[28] Computational modeling typically based on Density Functional Theory (DFT) has been used to the atomic-scale surface structure of CoCu catalysts and their dynamics with respect to changing reaction conditions.[29] For catalysts with sizes ranging from a single atom to small subnanometer-sized clusters, a cluster model or embedded cluster approach is typically used in the simulations.[30] The computational time, however, grows quite rapidly with the size of the CoCu particles, making a thorough investigation with DFT rather infeasible.[31]

Integrating all the experiential and theoretical works, four common structures[32] i.e., core-shell, segregated, mixed, and onion-like structures have all been suggested for CoCu catalysts. On top of this, the mechanism of CO hydrogenation has been looked over from an atomic perspective, e.g., pure Cu(211)[7], pure Co(111)[11], mixed CoCu(111) and CoCu(211)[12], Co-doped Cu(211)[9], pure Co(0001) and Cu doped Co(0001)[8]. Although all these well-defined models are originated from the possible CoCu structures during CO hydrogenation reaction. Three kinds of significant surfaces were neglected, i.e., the Cu terminated CoCu catalyst at the early stage of reaction, the partially segregated CoCu catalyst during the reaction, and the Co terminated CoCu catalyst at the late stage of the reaction.[22]

1.3 Scope of the Thesis

This thesis aims at investigating the CoCu catalysts in CO hydrogenation using multiscale simulation techniques.

Chapter 3, Modeling CoCu Nanoparticles Using Neural Network Accelerated Monte Carlo Simulations: In this chapter, we focus on the exploration of the CoCu catalysts without and with adsorbates. The key questions are what drives the formation of core-shell structures, and how the surface terminations depend on the CoCu ratios, particle sizes, and adsorbates. We use the machine learning accelerated Monte Carlo method to model clean CoCu particles up to the size of 3.6 nm. Besides, the genetic algorithm method is used to reveal the segregation behavior of CoCu surfaces with adsorbates.

Chapter 4, Insights into the Mechanism of CO Hydrogenation on Segregated CoCu Catalysts: In this chapter, we shed light on the reactivity of these two kinds of rarely studied surfaces from an atomic perspective. Cu terminated Cu/Co(111) and Cu_{2ML}/Co(111) are used to represent Cu segregated surfaces at the early stage of reaction and Co terminated Co/Cu(111) and Co_{2ML}/Cu(111) are used to represent Co segregated surfaces at the late stage of the reaction.

Chapter 5, Kinetic Assessment of Partially Segregated CoCu Catalysts for CO Hydrogenation: In this chapter, we investigate the reactivity of the real surface during the reaction. By incorporating the partially segregated CoCu/Co(111) with a high CO coverage from the analysis of phase diagrams, we use both MFT and kMC to explore the kinetics of the realistic surface during the reaction.

2. Methodology

2.1 Density Functional Theory

2.1.1 The Schrödinger Equation

The solution of the Schrödinger equation can provide all the information of a system. The time-independent, non-relativistic Schrödinger equation is given by

$$\hat{H}\Psi(r,R) = E\Psi(r,R) \tag{2.1.1}$$

where $\hat{H}$, $\Psi(r,R)$, and E are the Hamilton operator, the wave function, and the energy of state described by the wave function. The $\hat{H}$, Hamilton operator, operates on the wave function that depends on the coordinates of electrons (r) and nuclei (R).

$$\hat{H} = -\sum_{A=1}^{N_{nuclei}} \frac{1}{2M_A}\nabla_A^2 - \sum_{i=1}^{N_{elec}} \frac{1}{2}\nabla_i^2 - \sum_{A=1}^{N_{nuclei}} \sum_{i=1}^{N_{elec}} \frac{Z_A}{|R_A - r_i|}$$

$$+\sum_{i=1}^{N_{elec}} \sum_{j>i}^{N_{elec}} \frac{1}{|r_i - r_j|} + \sum_{A=1}^{N_{nuclei}} \sum_{B>A}^{N_{nuclei}} \frac{Z_A Z_B}{|R_A - R_B|} \tag{2.1.2}$$

The first two terms are the kinetic energies of nuclei and electrons, respectively. The last three terms are the potential energies of nucleus-electron attractive interaction, electron-electron repulsive interaction, and nucleus-nucleus repulsive interaction.

However, the full solution of the Schrödinger equation is nearly impossible, and approximations are always required. The most famous approximation, the Born-Oppenheimer approximation, treats nuclei and electrons separately considering the huge difference between nuclei and electrons in mass. Thus, the nuclei can be assumed to be stationary, and the electrons move around the fixed nuclei. As a result of the approximation, the kinetic energy is zero, and the strength of nucleus-nucleus repulsive interaction is constant. The Hamilton operator and the Schrödinger equation can be reduced to

$$\widehat{H}_{\mathrm{elec}} = -\sum_{i=1}^{N_{elec}} \frac{1}{2}\nabla_i^2 - \sum_{A=1}^{N_{nuclei}} \sum_{i=1}^{N_{elec}} \frac{Z_A}{|R_A - r_i|} + \sum_{i=1}^{N_{elect}} \sum_{j>i}^{N_{elec}} \frac{1}{|r_i - r_j|} \tag{2.1.3}$$

$$\widehat{H}_{elec}\Psi_{elec}(r,R) = E_{elec}\Psi_{elec}(r,R) \tag{2.1.4}$$

where E_{elec} is the electronic energy. Then the total energy of the system can be derived by the summation of E_{elec} and E_{nuclei}.

$$E_{tot} = E_{elec} + E_{nuclei} \tag{2.1.5}$$

2.1.2 The Kohn-Sham Approach

Density functional theory turned the focus from ware function Ψ to electron density $\rho(r)$. The foundation of the DFT is built upon the two Hohenberg-Kohn Theorems.[33] The first theorem states the ground state energy from the Schrödinger equation is a unique functional of the electron density. The second theorem states the electron density that minimizes the energy is corresponding to the true ground state electron density. The practical way to use the Hohenberg-Kohn Theorems is introduced by the Kohn-Sham equation:

$$E[\rho] = T_S[\rho] + E_{Ne}[\rho] + J[\rho] + E_{XC}[\rho] \tag{2.1.6}$$

where T_S is the non-interacting kinetic energy; E_{Ne} is the energy due to the interaction with the external potential; J is the Hartree energy; E_{XC} is the exchange-correlation energy. The exchange-correlation functional contains not only a portion of the kinetic energy, but also the non-classical effects of self-interaction correction, exchange, and correlation. To solve the Kohn-Sham equation, the exchange-correlation functional must be specified. However, the exact exchange-correlation functional is unknown. The criterion to evaluate the exchange-correlation functional is to compare with the accurate reference data, which is empirical.

The simplest exchange-correlation functional is the local density approximation (LDA). It's based on the hypothesis of the uniform electron gas.

$$E_{XC}^{LDA}[\rho] = \int f[\rho(r)]dr \tag{2.1.7}$$

The LDA did a successful job in determining equilibrium structure, harmonic frequencies, and charge moments. However, it has poor performance in energy.[34]

The second approach is the generalized gradient approximation (GGA). GGA functionals e.g., PW91[35], PBE[36], and RPBE[37] include the gradient of the density.

$$E_{XC}^{GGA}[\rho] = \int f[\rho(r), \nabla\rho(r)]dr \tag{2.1.8}$$

Meta-GGA functionals e.g., TPSS[38] include second derivatives of the density. Hybrid functionals e.g., B3LYP[39] and PBE0[40] include different percentages of the explicit Hartree-Fock exchange to reduce the Coulomb self-interaction error.

2.2 Global Optimization

2.2.1 Basics

Global optimization is a kind of technique to local the global minimum. In the field of heterogeneous catalysis, global optimization is used to find the lowest-energy structure for a system with a given composition, which is a common and important goal. The lowest-energy structure is corresponding to the global minimum of the potential energy surface (PES). Theoretically, the lowest-energy structure found in the simulation is the most probable candidate formed in experiments. Although, depending on experimental conditions, the structures observed experimentally may be kinetic, rather than thermodynamic products.[41] In general, the structures under low temperature and pressure are more likely to be reproduced by global optimization techniques.

In heterogeneous catalysis, there are three fields of global optimization that produced fruitful results.[42]

1. The optimization of clusters and particles under vacuum conditions.[41,43–47]
2. The determination of stable, catalytically important surfaces.[29,48–50]
3. The adsorption, growth, and migration of particles upon the substrate.[51]

Two widely used global optimization approaches will be covered in detail in the next two sections i.e., basin hopping, and genetic algorithm,

2.2.2 Basin Hopping

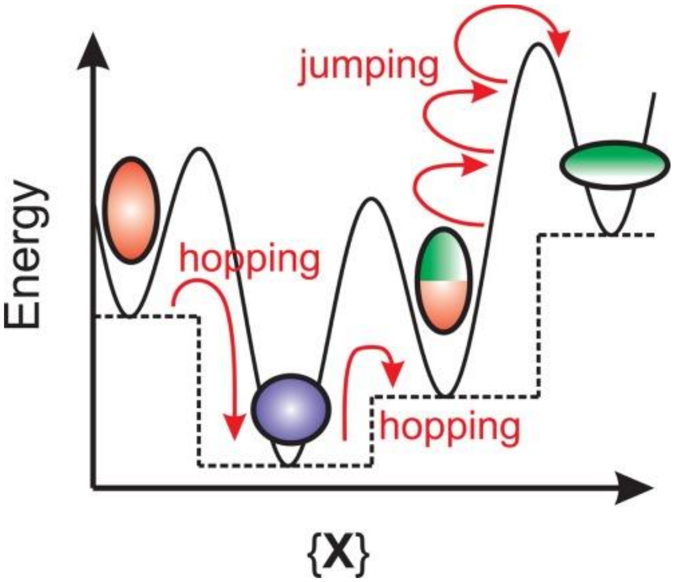

Figure 2.1 Schematic representation of the basin hopping. Reprinted from Ref.[52] with permission from Wiley-VCH. The solid line is the original continuous potential energy surface, and the dashed line is the transformed discrete potential energy surface.

Basin hopping, also known as Monte Carlo (MC) method was initially developed by Wales as shown in Figure 2.1.[43] The underlying idea of this method is transforming continuous potential energy surface into discrete local minima. By combing a search strategy, the configuration can move from one basin into another.[53] The basic Monte Carlo steps using a canonical ensemble are listed below:

1. Randomly pick one structure.
2. Generate a new structure by random displacement or permutation.
3. Calculate the energy difference between the original and new structure.
4. Following the Metropolis criterion, the new structure will be either accepted or rejected.
5. If the structure is accepted, it will be used for the next loop. Otherwise, the last accepted structure will be used.

The key problem of basin hopping is the balance between the local and global search of the energy landscape. The local optimization serves to local the configuration corresponding to the local minima, which needs to be done efficiently and accurately at the same time. Using empirical interatomic potentials or DFT as the workhorse will either be inaccurate or inefficient. Luckily, by incorporating the trained potential into the local optimization process, the newly emerging machine-learning accelerated approaches make the basing hopping method more promising.[54–56].

2.2.3 Genetic Algorithm

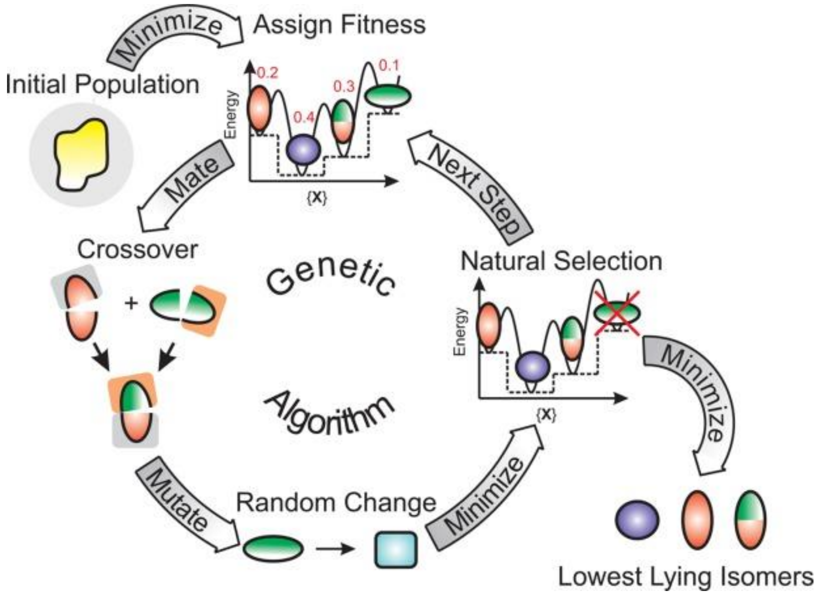

Figure 2.2 Schematic representation of the genetic algorithm. Reprinted from Ref.[52] with permission from Wiley-VCH.

Genetic algorithm is a strategy inspired by the Darwinian evolution process shown in Figure 2.2. According to the pioneering work fulfilled by Deaven and Ho[57], the genetic algorithm starts with a population of candidate structures, and relaxes these candidates to the local minimum. Then, using the relaxed energies as the criteria of fitness, a fraction of the population is selected as "parents". The next generation of candidate structure is produced by mating these parents. The process is repeated until the ground state structure is located.

Although this method cannot be validated mathematically, genetic algorithm has been widely used and proven effective. Another problem genetic algorithm faced is similar to basin hopping, i.e., the local minimization is hard to archive the accuracy and efficiency simultaneously. Similarly, machine-learning accelerated techniques have also been proven successful.[58]

2.3 ACSF Method

2.3.1 Basics

The general idea behind machine learning here is to automate the model discovery step. Instead of fitting the parameters of a predefined model to reference data, an appropriate model able to describe the feature-space of input data shall be automatically determined and parametrized by the machine learning method.[59] There exist various architectures of these models, which can be broadly split into two categories:[60] 1. Descriptor-based models, which take a predefined representation of the system as input. 2. End-to-end architectures, that learn a representation directly from atom types and positions.

2.3.2 ACSF Method

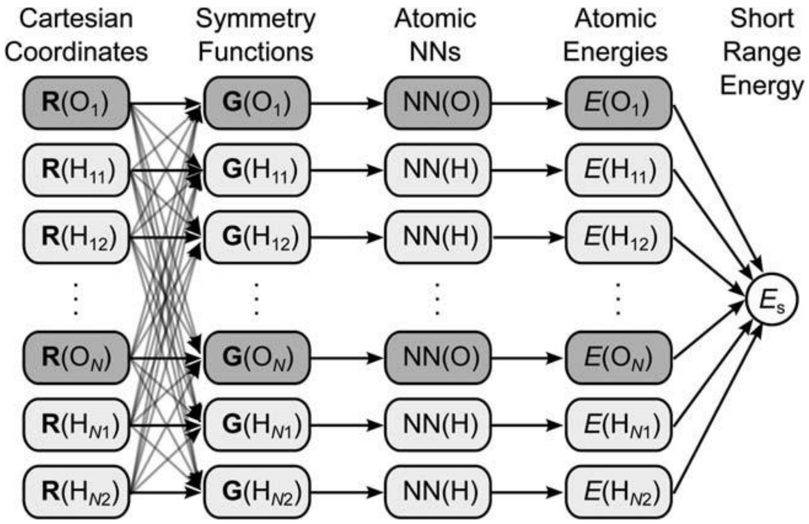

Figure 2.3 The schematic of the ACSF method. Reprinted from Ref.[61] with permission from Wiley-VCH.

The descriptor-based atom-centered symmetry functions (ACSF) method developed by Behler et al. shown in Figure 2.3 is one of the most widespread methods in the field of heterogeneous catalysis[61–63] Within the framework ACSF method, the potential energy surface is described as a function of the atomic nuclei under Born-Oppenheimer approximation.[61] The atomic energy contributions depend on the local environments up to a cutoff radius R_C. Within the range of the cutoff sphere, the atomic environment consisting of the positions of all atoms is described by the symmetry functions. To provide a sufficient resolution of geometric features, a set of two-body radial and three-body angular symmetry functions will be collected.[63]

Radial ACSF is given by

$$G_i^{rad} = \sum_{j \neq i}^{N} e^{-\eta\left(r_{ij}-\mu\right)^2} f_c\left(r_{ij}\right) \tag{2.3.1}$$

$$f_c\left(r_{ij}\right) = \begin{cases} \frac{1}{2}\left[\cos\left(\frac{\pi r_{ij}}{r_c}\right)+1\right], & r_{ij} \leq r_c \\ 0, & r_{ij} > r_c \end{cases} \tag{2.3.2}$$

where N is the number of atoms and r_{ij} is the distance between atom i and j. η and μ are the parameters related to the width and position of the Gaussian function. f_c is the cutoff function.

Angular ACSF is given by

$$G_i^{ang} = 2^{1-\zeta} \sum_{j \neq i}^{N} \sum_{k \neq i,j}^{N} \left(1+\lambda\cos\theta_{ijk}\right)^{\zeta} e^{-\eta\left(r_{ij}-\mu\right)^2} e^{-\eta(r_{ik}-\mu)^2} e^{-\eta\left(r_{jk}-\mu\right)^2} f_{ij} f_{ik} f_{jk} \tag{2.3.3}$$

where θ_{ijk} is the angle created by atoms i, j, and k. λ and ζ control the distribution of angular symmetry functions. All these symmetry functions will be normalized before being fed into the neural network as the fingerprints illustrated in Figure 2.3. Once the atomic energies are obtained from the neural network, the total energies of the system can be derived from the summation of the atomic energies.

The biggest limitation of the ACSF method is using separate neural networks to treat different elements, which leads to undesirable scaling of computational time with the increasing number of varied elements. To overcome the limitations, the weighted atom-centered symmetry functions (wACSF) method incorporates the atomic number into the symmetry function, which requires fewer neural networks to achieve better performance.[64]

Radial wACSF is given by

$$G_i^{rad} = \sum_{j \neq i}^{N} g(Z_j) e^{-\eta(r_{ij}-\mu)^2} f_c(r_{ij}) \tag{2.3.4}$$

Angular wACSF is given by

$$G_i^{ang} = 2^{1-\zeta} \sum_{j \neq i}^{N} \sum_{k \neq i,j}^{N} h(Z_j, Z_k)(1 + \lambda \cos \theta_{ijk})^{\zeta} e^{-\eta(r_{ij}-\mu)^2} e^{-\eta(r_{ik}-\mu)^2} e^{-\eta(r_{jk}-\mu)^2} f_{ij} f_{ik} f_{jk} \tag{2.3.5}$$

The wACSF method enables to train models on small systems within the reach of *ab initio* approaches, then use these potentials to investigate large, and complex systems such as interfaces, surfaces, grain boundaries, and amorphous materials.[56,58,65–69]

2.4 Thermodynamics and Kinetics

2.4.1 Thermodynamics

The key concept in thermodynamics is the Gibbs energy which is defined as

$$\mathrm{G = H - TS} \tag{2.4.1}$$

where *H*, *T*, and *S* are enthalpy, temperature, and entropy, respectively.

The change in Gibbs energy determines whether a catalytic reaction will proceed.[70] In a gas-solid heterogeneous catalytic reaction, the two typical states of the reactants are the gas phase and adsorbate.

2.4.1.1 Ideal Gas Approximation

The gas phase is handled by the ideal gas approximation.[3,71] In ideal gas approximation, all the transitional, rotational, and vibrational degrees of freedom are considered. The enthalpy of an ideal gas was calculated by extrapolating the energy from 0 K to the real temperature.

$$H(T) = E_{elec} + E_{ZPE} + \int_0^T C_P dT \tag{2.4.2}$$

where E_{elec}, E_{ZPE}, C_P are the electronic energy, zero-point energy (ZPE), and constant-pressure heat capacity respectively.

$$\mathrm{E_{ZPE}} = \sum_{i=1}^{N_{modes}} \frac{1}{2}\mathrm{h\omega_i} \tag{2.4.3}$$

$$C_P = k_B + C_{V,trans} + C_{V,rot} + C_{V,vib} + C_{V,elec} \tag{2.4.4}$$

The translational constant-volume heat capacity is 1.5 k_B. If the molecule is monatomic, linear, or nonlinear, the rotational heat capacity will be 0, 1 k_B, or 1.5 k_B, respectively. For nonlinear and linear molecules, *3N-6* and *3N-5* degrees of freedom are used for the vibrational heat capacity, separately. The vibrational heat capacity is given by

$$\int_0^T C_{V,vib} dT = \sum_{i}^{vib\ DOF} \frac{\epsilon_i}{e^{\epsilon_i/k_B T} - 1} \tag{2.4.5}$$

The entropy of ideal gas is given by

$$S(T,P) = S(T,P^o) - k_B \ ln\frac{P}{P^o} = S_{trans} + S_{rot} + S_{elec} + S_{vib} - k_B \ ln\frac{P}{P^o} \tag{2.4.6}$$

$$S_{trans} = k_B \left\{ \ln\left[\left(\frac{2\pi M k_B T}{h^2} \right)^{3/2} \frac{k_B T}{P^o} \right] + \frac{5}{2} \right\} \tag{2.4.7}$$

If the molecule is monatomic,

$$S_{rot} = 0 \tag{2.4.8}$$

If the molecule is linear,

$$S_{rot} = k_B \left[\ln\left(\frac{8\pi^2 I k_B T}{\sigma h^2} \right) + 1 \right] \tag{2.4.9}$$

If the molecule is nonlinear,

$$S_{rot} = k_B \left\{ \ln\left[\frac{\sqrt{\pi I_A I_B I_C}}{\sigma} \left(\frac{8\pi^2 k_B T}{h^2} \right)^{3/2} \right] + \frac{3}{2} \right\} \tag{2.4.10}$$

$$S_{elec} = k_B \ln[2 \times (total\, spin) + 1] \tag{2.4.11}$$

$$S_{vib} = k_B \sum_{i}^{vib\, DOF} \left[\frac{\epsilon_i}{k_\mathrm{B} T (e^{\epsilon_i / k_\mathrm{B} T} - 1)} - \ln\left(1 - e^{-\epsilon_i / k_\mathrm{B} T}\right) \right] \tag{2.4.12}$$

By combining the enthalpy, temperature, and entropy, the Gibbs free energy is given by

$$G(T, P) = H(T) - TS(T, P) \tag{2.4.13}$$

2.4.1.2 Harmonic Approximation

The adsorbates are handled by the harmonic approximation.[3] All the degrees of freedom are treated harmonically.

$$U(T) = E_{elec} + E_{ZPE} + \sum_{i}^{harm\, DOF} \frac{\epsilon_i}{e^{\epsilon_i / k_B T} - 1} \tag{2.4.14}$$

$$S = k_B \sum_{i}^{harm\, DOF} \left[\frac{\epsilon_i}{k_\mathrm{B} T (e^{\epsilon_i / k_\mathrm{B} T} - 1)} - \ln\left(1 - e^{-\epsilon_i / k_\mathrm{B} T}\right) \right] \tag{2.4.15}$$

$$F(T) = U(T) - TS(T) \tag{2.4.16}$$

If the pV in $H = U + pV$ is assumed negligible,

$$G(T) = U(T) - TS(T) \tag{2.4.17}$$

2.4.2 Kinetics

The calculation of the free energy enables the determination of equilibrium. However, the catalytic process is more about how much the catalyst speeds up the reaction, i.e., the kinetics.[70] In heterogeneous catalysis, the study of kinetics consists of three different aspects: kinetics for design purposes, kinetics for mechanistic details, and kinetics as a consequence of a reaction mechanism.[72] The last aspect is the least explored one, and it requires the thermodynamic profiles of all the elementary reactions.

An elementary reaction describes the transition from a molecule to an adsorbate and vice versa or from an adsorbate to an adsorbate. Depending on the description of the surface, two routes are available. The first one assumes all sites are equivalently distributed on a homogeneous surface, which leads to the mean-field theory and the rate equation. The second one explicitly represents the lattice, which yields the lattice Monte Carlo and Master equation.[73]

The shared fundamental concept for both MFT and kMC is the rate constant[70]

$$k = \frac{k_B T}{h} \exp\left(\frac{-\Delta G^{\ddagger}}{k_B T}\right) \tag{2.4.18}$$

where $-\Delta G^{\ddagger}$ is the free energy difference between the transition state (TS) and the initial state (IS).

2.4.2.1 Mean-field Theory

The MFT consists of five assumptions: 1. The surface is homogeneous; 2. All sites are equivalent. 3. Each site can hold at most one adsorbate; 4. The diffusion is infinitely fast. 5. There are no explicit interactions between adsorbates.[74]

The reaction rates of the whole reaction network are obtained by solving the mean-field model to the steady state. The differential equations[74] are given by

$$r_i = k_i^{+} \prod_j \theta_{ij} \prod_j p_{ij} - k_i^{-} \prod_l \theta_{ij} \prod_l p_{il} \tag{2.4.19}$$

$$\frac{\partial \theta_i}{\partial t} = \sum_j s_{ij} r_j \tag{2.4.20}$$

where r_i is the rate of each elementary step, k_i is the forward/reverse rate constant, θ_{ij} and p_{ij} are the surface coverage and unitless pressure for elementary step *i*, and s_{ij} are coefficients for the stoichiometry of species *i* in elementary step *j*. The solution to the steady state is given by

$$\frac{\partial \theta_i}{\partial t} = 0 \tag{2.4.21}$$

Where θ is normalized and the summation of θ_i is 1.

2.4.2.2 Kinetic Monte Carlo

In some cases, the lateral interaction of the adsorbates is significant, which calls the kinetic Monte Carlo simulations.[75] In kMC, the surface is represented by a lattice where each lattice point corresponds to a surface site.[76] The lattice with values is called a configuration. An elementary reaction will move the configuration to a new one. This state-to-state jumps of the system is a so-called Markov chain that enables to meet the rate events in a significantly reduced time scale.[77]

The evolution of the system is described by the Markovian master equation

$$\frac{dP_i(t)}{dt} = -\sum_{i \neq j} k_{ij} P_i(t) + \sum_{i \neq j} k_{ji} P_j(t) \tag{2.4.22}$$

Where k_{ij} is the rate constant of the elementary step from state *i* to state *j*, $P_i(t)$ is the possibility to be in state *i* at time *t*.

The system has a possibility to keep unchanged after a short increment of time, and the probability that teh system has not yet escaped from state *i* is given by

$$\frac{P(t + dt) - P(t)}{dt} = -kP(t) \tag{2.4.23}$$

By solving the equation above, the time needed to transit to another state is given by

$$t_{\mathrm{transit}} = \frac{-\ln(\rho)}{k} \qquad (2.4.24)$$

where ρ is a random number and located between 0 and 1.

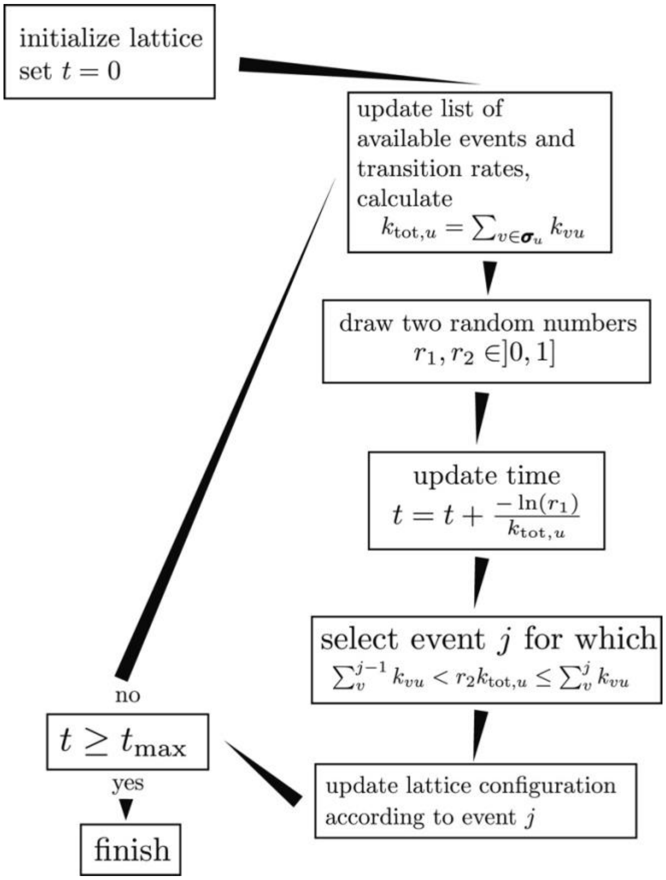

Figure 2.4 The general workflow of kinetic Monte Carlo simulations using the variable step-size method.[78] Reprinted from Ref.[79] with permission from Elsevier.

The variable step-size method (VSSM)[79] used for kMC simulations is illustrated in Figure 2.4. For VSSM, all the available events are collected, and the total rate constant is calculated. The time is advanced by $t_{transit}$, and one of the available events was chosen with a possibility weighted by its rate constant. The lattice configuration is updated according to the event selected. This loop continues until the simulation time was met.

3. Modeling CoCu Nanoparticles Using Neural Network Accelerated Monte Carlo Simulations[1]

3.1 Introduction

The machine learning techniques[63,65,66,56,69] are representing an exciting new avenue as they often reach accuracy close to DFT while being computationally orders of magnitude faster as they typically scale linearly with system size[63].

In this chapter, we will focus on the first step, the exploration of the CoCu catalysts without any adsorbates. The key questions are what drives the formation of core-shell structures vs mixed structures, and how the surface terminations depend on the CoCu ratios, and the particle sizes. Addressing these questions with DFT calculations is still limited to the extrapolations originating from extended surface models,[29] especially when many configurations of large particles need to be calculated. Herein we use the weighted atom-centered symmetry function based method[64] to model CoCu particles up to the size of 3.6 nm. By introducing neural networks, the high-dimensional potential energy surfaces can be described accurately and effortlessly.[56] The wACSF model is trained and validated using DFT calculations on CoCu structures with sizes of 0.5 nm. Inspired by work from Kitchin et al[54], we furthermore introduce Monte Carlo simulations to investigate the structure of CoCu particles as a function of CoCu ratio, size, and temperature.

---

[1] This chapter is based on the following publications: [1] Zha, S.; Sharapa, D.; Liu, S.; Zhao, Z.-J.; Studt, F. Modeling CoCu Nanoparticles Using Neural Network Accelerated Monte Carlo Simulations, submitted. [2] Liu, S.; Zhao, Z.-J.; Yang, C.; Zha, S.; Neyman, K. M.; Studt, F.; Gong, J. Adsorption Preference Determines Segregation Direction: A Shortcut to More Realistic Surface Models of Alloy Catalysts. ACS Catal. 2019, 9 (6), 5011–5018.

3.2 Methods

Density Functional Theory Calculations. The Vienna Ab initio Simulation Package (VASP 5.4.4)[80,81] was used in conjunction with the Bayesian error estimation functional with van der Waals correlation (BEEF-vdW)[82,83]. Core electrons were treated using the projector augmented-wave (PAW) method.[84,85] Valence electrons were described using a plane-wave basis set with cut-off energy of 400 eV. Calculations were performed at the Γ-point in the reciprocal space with 0.15 eV smearing and the total energies were evaluated by extrapolating to the zero broadening. All calculations were spin-polarized and vacuum spacing larger than 16 Å was applied.

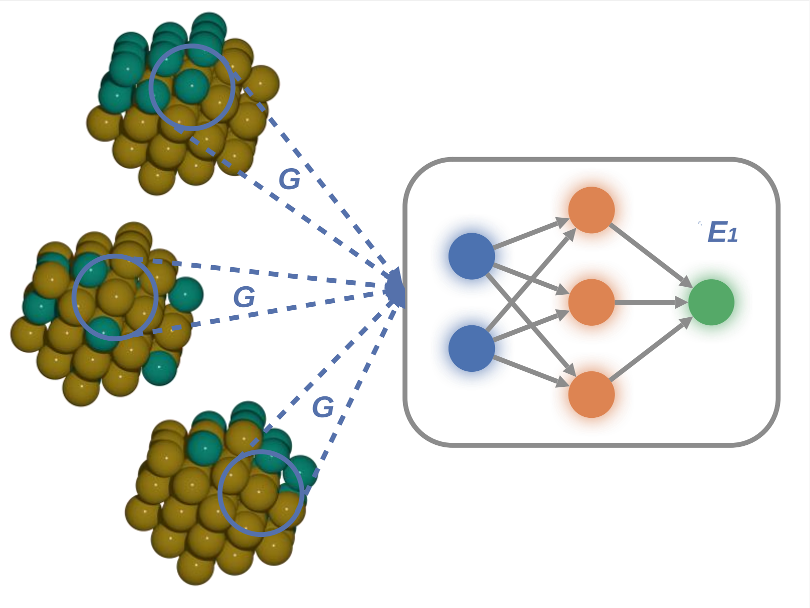

Figure 3.1 Schematic illustration of the wACSF method. Co atoms are in green and Cu atoms are in Bronze.

Neural Network Potential. The wACSF method[64] illustrated in Figure 3.1 originates from the atom-centered symmetry functions (ACSF) approach[62,63], while it incorporates the atomic number into the symmetry functions (G in Figure 3.1) to achieve comparable performance with fewer neural networks. The atomic energy contributions depend on the local environments up to a cutoff radius R_C that was set to 6.0 Å. This value was found to be adequate in previous works of similar systems,[54,65] with a larger cutoff not showing noticeable improvements. Within the range of the cutoff sphere, the positions of the neighboring atoms are described by a set of many-body symmetry functions. After the normalization, all these symmetry functions are fed into the neural network as fingerprints. Once the atomic energies are obtained from the network, the total energies of the system can be derived from the summation of the atomic energies. All wACSF calculations were performed using the SchNetPack[60] package. The parametrization of symmetry functions in this chapter is based on the method suggested by Gastegger et al.[64] and the detailed parameters for radial and angular symmetry functions can be found in Table A1.1 and Table A1.2. After tuning the hyperparameters (Figure A1.1 and Figure A1.2), we used a network containing 3 hidden layers and 10 nodes and a learning rate of 0.03 as the default option.

784 cuboctahedral particles of $Co_{13}Cu_{42}$ (Co:Cu ratio close to 1:3) were generated and divided into 3 sets: a training set (70%), a validation set (15%), and a test set (15%). The validation set was used to detect overfitting during training, while the test set is independent of the training process. No optimizations were performed on the particles. Thus, the position of each atom is fixed while chemical ordering is variable. Interatomic distances were kept fixed to the value of optimized (BEEF-vdW functional) pure Cu (2.584 Å).

Monte Carlo Simulations. Neural network accelerated MC (wACSF-MC) simulations were performed using a canonical ensemble. The simulations were performed by randomly picking one input structure, permutating two atoms with different elements, calculating the potential energy using the wACSF model, and obtaining the energy difference between the two structures. Following the Metropolis criterion, the structure was either accepted or rejected. Accepted structures were considered for the next loop. Otherwise, a new permutation was performed using the last accepted structure.

3.3 Results

3.3.1 Accuracy of wACSF

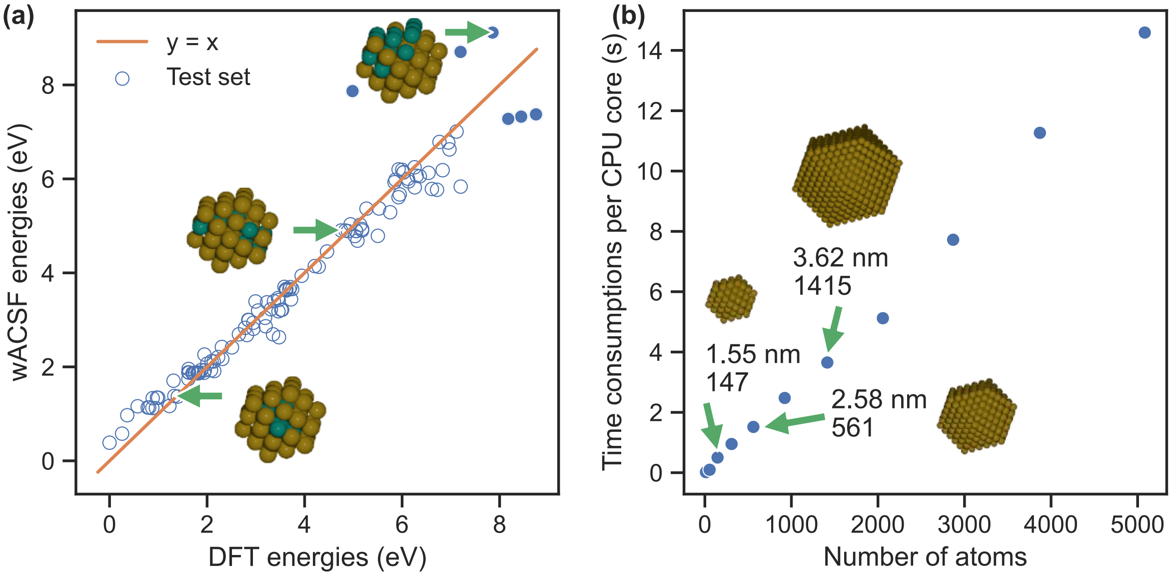

Figure 3.2 (a) Correlation between DFT and wACSF energies in the test set consisting of 117 cuboctahedral $Co_{13}Cu_{42}$ particles. The mean absolute error is 0.18 eV. Solid data points indicate subcluster segregated alloys (i.e., Janus-like particles). (b) The efficiency of the wASCF model. The time consumption of an energy calculation is given as a function of the number of atoms of the Cu cuboctahedral particles. The nanoparticle with 5000 atoms is approximately 5.7 nm in diameter.

Figure 3.2a compares energies from full DFT calculations with those obtained from the wACSF model for 117 different cuboctahedral $Co_{13}Cu_{42}$ particles in the test set. While we find that the majority of structures exhibit a rather good correlation between DFT and wACSF energies, we note that there are a few outliers for structures with high energy (> 4.5 eV, with filled markers). All these structures were found to be subcluster segregated alloys (Janus-like particles) which are comparatively very high in energy and thus not expected to play a role in the following discussion. For the other structures of the test set with lower energies, the wACSF model shows a high accuracy (MAE= 0.18 eV, RMSE= 1.69 meV/atom vs MAE= 0.28 eV, RMSE= 3.25 meV/atom of the whole set). Figure 3.2b shows the efficiency of the wACSF method by calculating cuboctahedral Cu particles with sizes from 13 atoms to 5,083 atoms. Importantly, we found a linear increase of calculational time with the number of atoms of the cuboctahedral particles for the entire range considered here. Note that the Cu_{5083} particle is 5.7 nm in diameter. The linear scaling of the method thus allows the investigation of nanoparticles that are in the range of typically supported transition metal catalysts.

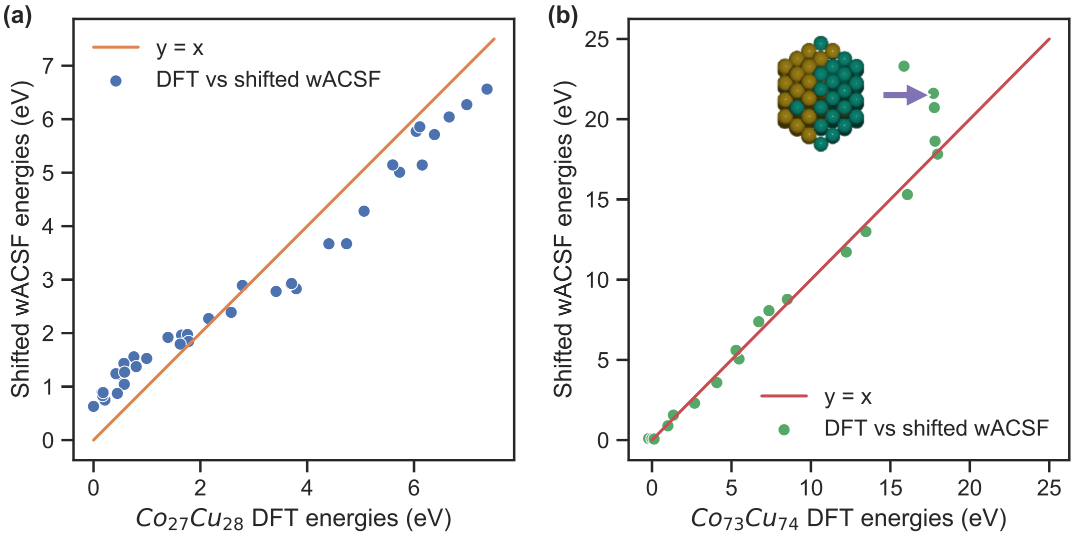

Figure 3.3 Correlation between relative DFT and wACSF energies when the $Co_{13}Cu_{42}$-trained model is applied to (a) $Co_{27}Cu_{28}$ and (b) $Co_{73}Cu_{74}$.

The concept of atom-centered symmetry functions implemented in the wACSF method enables us to apply the trained model to investigate systems whose sizes and atomic compositions differ from the training set.[65] First, the transferability of our wACSF model with different CoCu ratios was examined. The wACSF model trained on $Co_{13}Cu_{42}$ particles was applied to 39 randomly generated $Co_{27}Cu_{28}$ particles shown in Figure 3.3a. While in the case of the same composition (Figure 3.2a), the wACSF model directly reproduces the DFT energies. In the case of different compositions (Co:Cu ratios), a systematic shift of the predicted energies was observed (see Figure A1.3a). The relative energies, however, are still accurately reproduced. This confirms the transferability of the trained wACSF models to systems with different CoCu ratios. In addition, the same wACSF model from $Co_{13}Cu_{42}$ was applied to 20 randomly generated $Co_{73}Cu_{74}$ particles demonstrated in Figure

3.3b. Similarly, when considering the energy difference between DFT and wACSF (see Figure A1.3b), the DFT energies are well reproduced by the wACSF model, especially for the most stable nanoparticles (up to 16 eV). Again, the outliers are due to particles with subcluster segregation that are neglected in this contribution. In summary, the results in Figure 3.2 and Figure 3.3 show the ability of the wACSF model to reproduce the DFT results quite accurately.

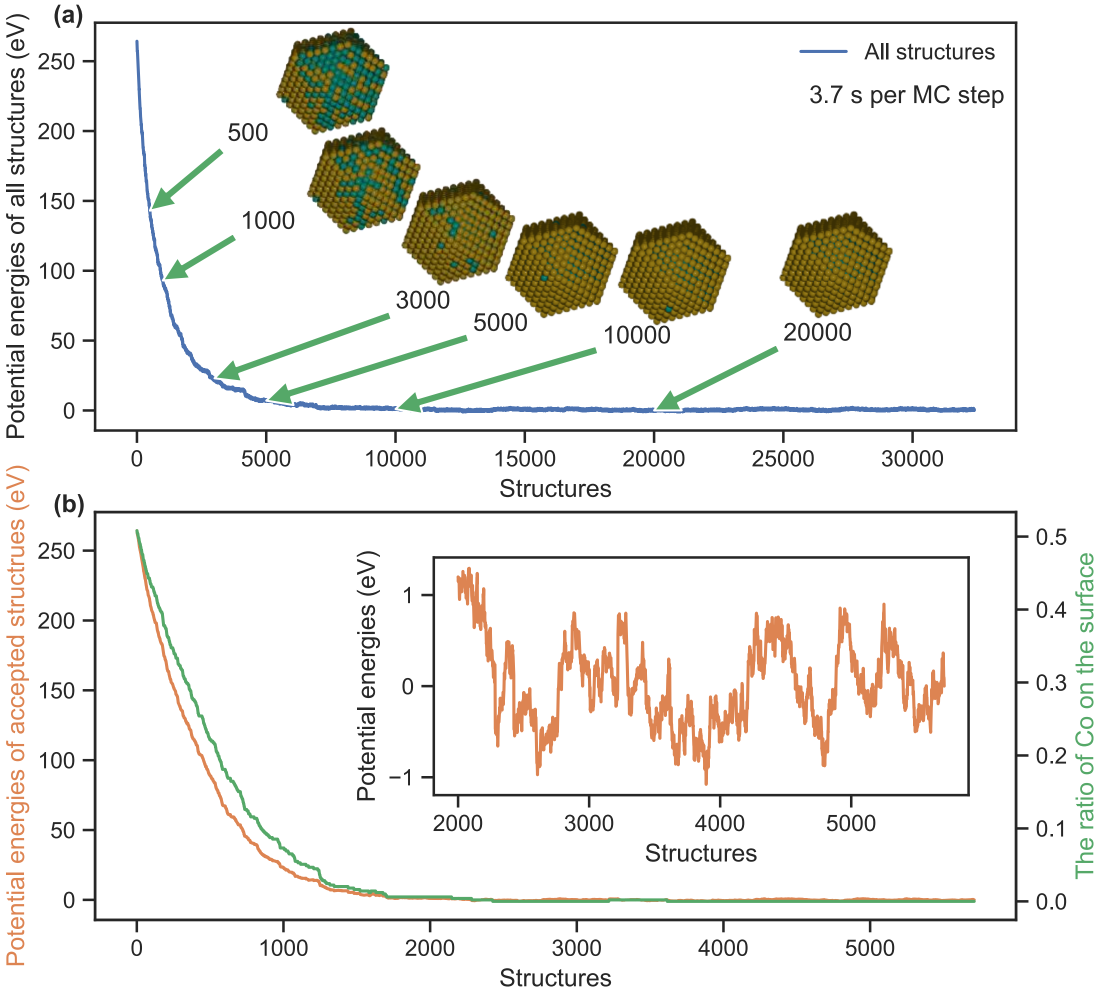

Figure 3.4 (a) All the structures, and (b) the accepted structures in neural network accelerated MC simulation (orange data) and the ratio of surface Co atoms (green data) for a $Co_{707}Cu_{708}$ particle simulated at 600 K.

3.3.2 Monte Carlo Simulations

Having established that the wACSF model can quite accurately reproduce DFT calculations for a variety of CoCu nanoparticles, we now turn to investigate the segregation behaviors of CoCu alloys. We use Monte Carlo simulations of cuboctahedral particles with varying Co:Cu ratios, particle sizes, and temperatures. The MC simulation of a $Co_{707}Cu_{708}$ particle at 600 K is shown as an example in Figure 3.4. The initial particle has been arbitrarily generated and exhibits a large proportion of Co atoms on the surface. At the beginning of the MC simulation, a large fraction of structures is accepted (Figure A1.4), and swapping Co atoms from the surface to the core significantly decreases the potential energy of the particle. After about 10,000 steps (about 2,193 accepted steps), the surface of the particle contains almost exclusively Cu atoms, and the potential energy reaches a plateau. After the 20,000th step, the $Co_{707}Cu_{708}$ surface is entirely consisting of Cu atoms, with all Co located in the bulk of the particle. In total, 30,000 steps were performed to assure the convergence of the MC simulation. In Figure 3.4b, the potential energies of accepted structures decrease simultaneously with the ratio of Co on the surface. No more changes in both potential energies and Co ratio on the surface occurred in our MC simulations confirming the convergence.

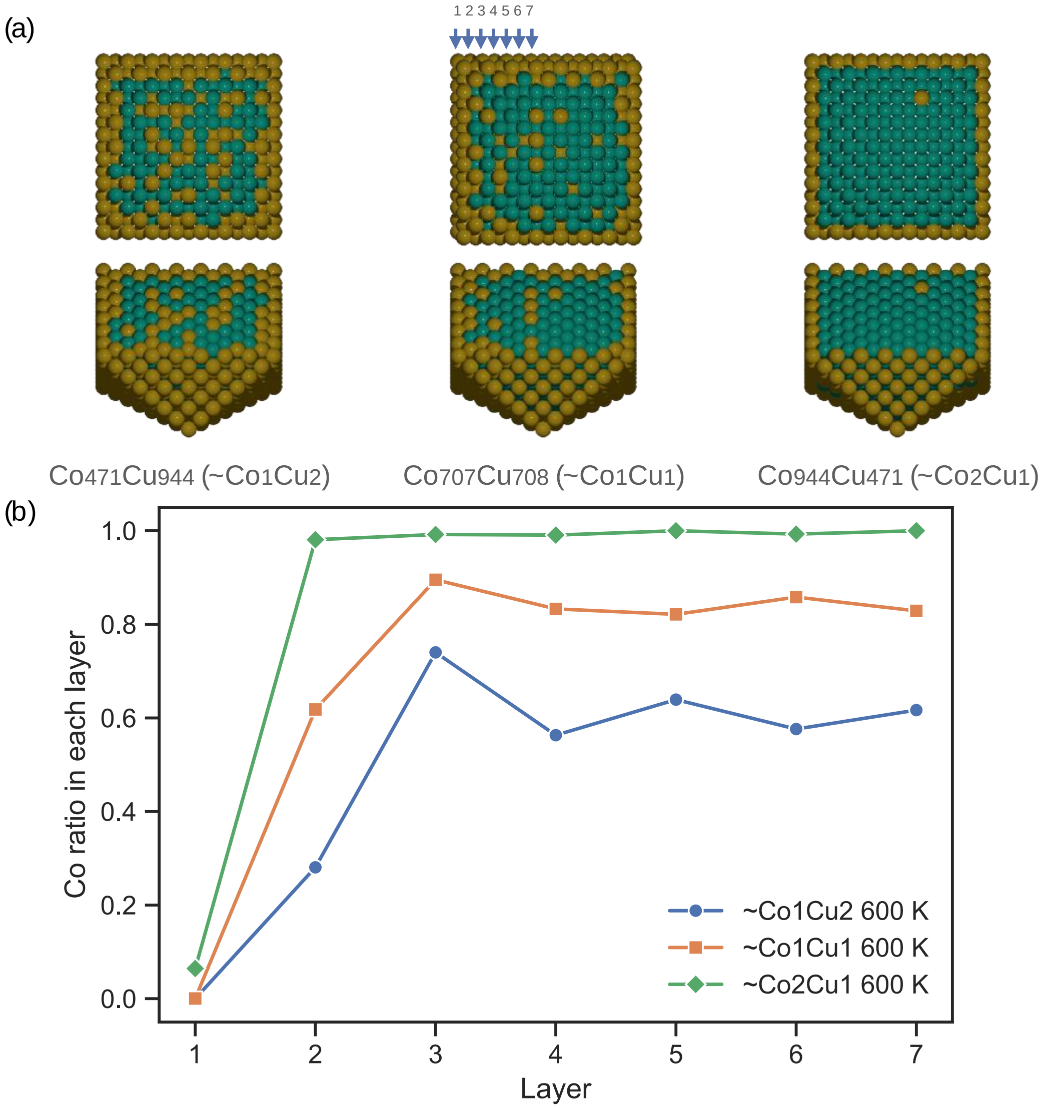

Figure 3.5 Segregation behaviors changed with different CoCu ratios in particles with 1415 atoms according to wACSF-MC. (a) optimized configurations and (b) average Co ratios for 10 converged structures in each layer.

We start by discussing the results of neural network accelerated MC simulations with different CoCu ratios. We chose three CoCu ratios (1:2, 1:1, and 2:1) to investigate the effect of atomic composition during the segregation process in cuboctahedral particles, using the same particle size as in Figure 3.4 (1415 atoms; diameter of about 3.6 nm) and a temperature of 600 K. The three most thermodynamically preferred structures obtained from the MC simulations are shown in Figure 3.5a. It can be seen that copper prefers to enrich the surface as well as the subsurface of the particles, forming a core-shell structure. Only if enough copper is present in the particle, such that the first two surface layers are saturated with Cu, a randomly mixed CoCu core will form (see $Co_{471}Cu_{944}$). These data indicate that the outer two layers play a dominant role in understanding the segregation phenomenon of CoCu particles.

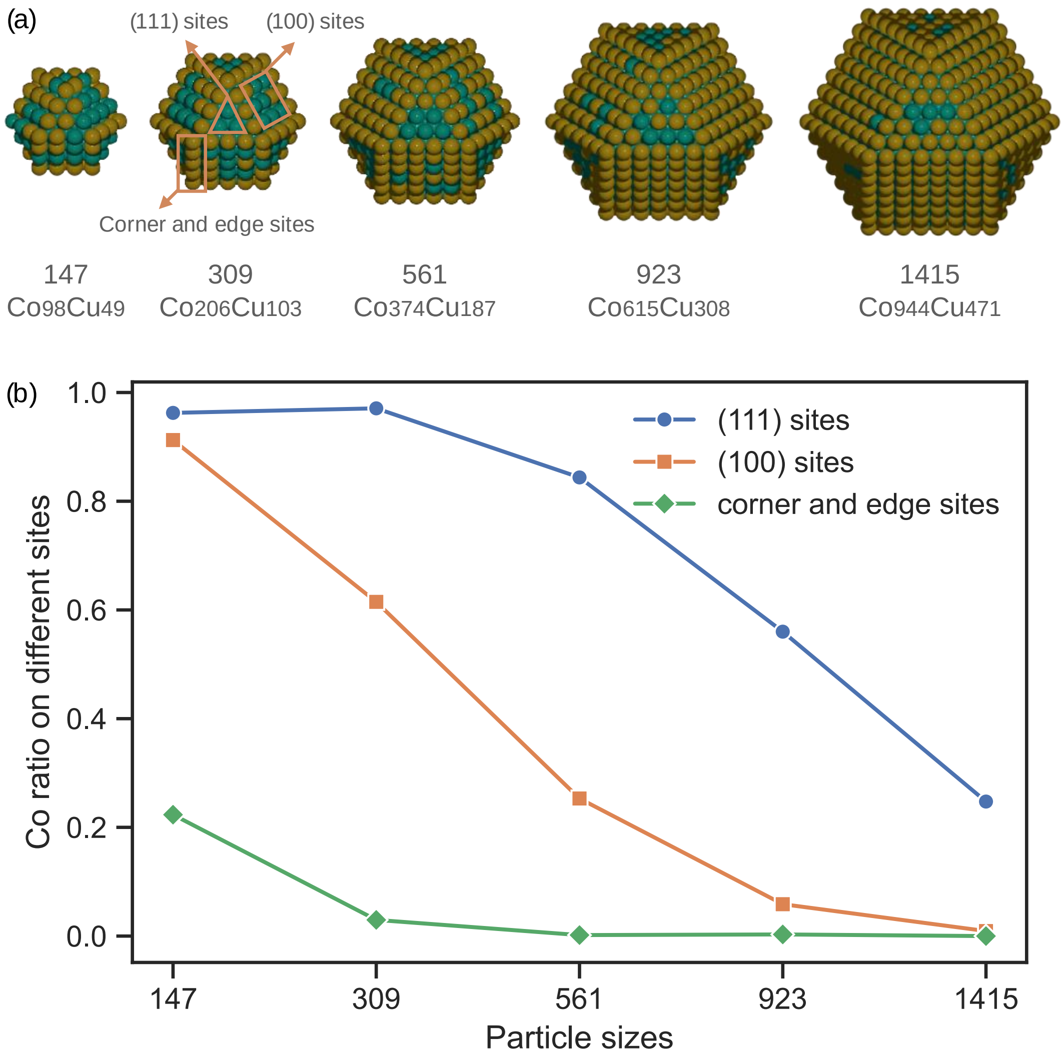

Figure 3.6 Surface distribution of Co in ~Co_2Cu_1 nanoparticles of different sizes at 600 K. Segregation behavior with different sizes according to wACSF-MC. (a) optimized configurations and (b) average Co ratios for 10 converged structures on different sites.

Next, a series of cuboctahedral particles (Co:Cu ratio close to 2:1) with different sizes were investigated (see Figure 3.6). Using this variation in sizes allowed us to disentangle the tendency of Cu segregation towards different surface sites, e.g. (111), (100), as well as edges and corners. For $Co_{944}Cu_{471}$, where only a few Co atoms are located at the surface of the nanoparticle (as there is not enough Cu to cover the entire surface layer) Co atoms are predominantly located on (111) sites. As the ratio of surface to bulk atoms increases with decreasing particle size, more Co atoms constitute the surface layer. As can be seen from Figure 3.6, these Co atoms tend to be located on the close-packed surfaces with the preference being (111) > (100) > edges & corners. To conclude, if surface segregation occurs for CoCu particles, Cu atoms tend to cover corner and edge sites first, then (100) and (111) sites. We also investigated the effect of temperature on the distribution of Co and Cu atoms in the particles and found very little effect of temperature on the chemical ordering of particles (see Figure A1.5, and Figure A1.6).

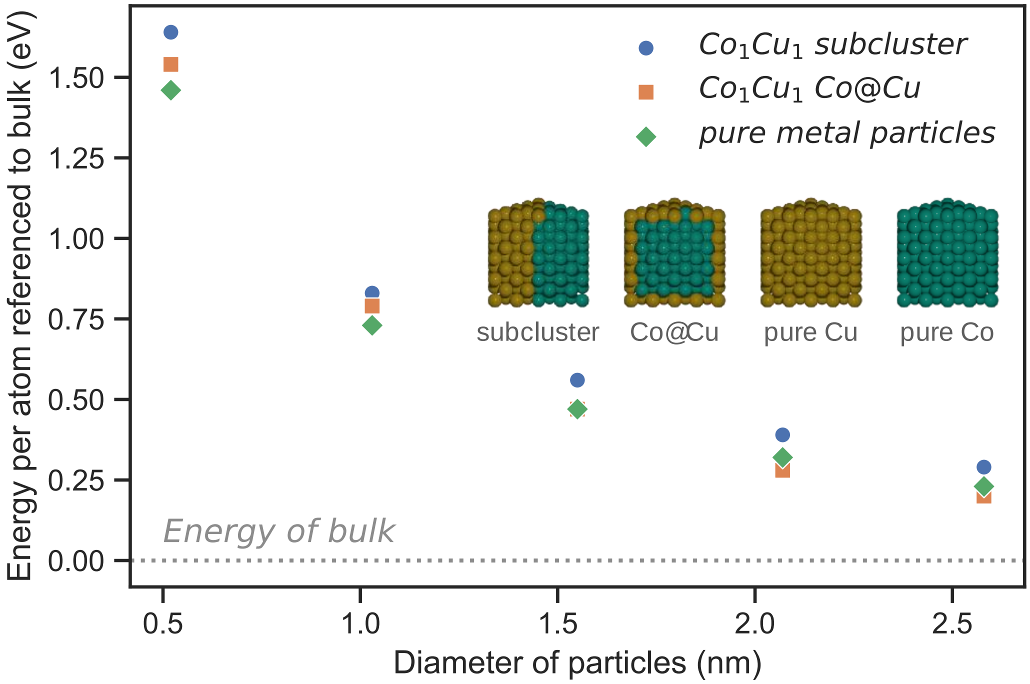

Figure 3.7 The relative stability among CoCu subclusters, Co@Cu core-shell particles, and Co and Cu pure particles.

Using the obtained core-shell structures when investigating the size effect, we calculated the DFT single point energies of these structures, the results of which are shown in Figure 3.7 Comparing the DFT single point energies of the Co_1Cu_1 subclusters, the energies of core-shell structures are always lower. This confirmed our MC simulation results that core-shell structures are always preferred when alloys are formed. An interesting transition was found when comparing the stability of the core-shell particles with those of pure Co and Cu particles. This is interesting since Co and Cu are immiscible and not known to form alloys. However, the phenomenon changes with the size of particles. When the diameter of the particle is smaller than ~1.5 nm, the formation energy of Co_1Cu_1 alloys is positive, and Co_1Cu_1 alloy is not stable in agreement with the phase diagram of bulk Co and Cu. Interestingly though, when particles with a diameter larger than 1.5 nm are considered, we notice the Co@Cu core-shell alloys are stabler than pure Co and Cu particles, providing theoretical proof that these core-shell structures might indeed form and be stable. This turning point is also found for Co_1Cu_2 (~1.0 nm) and Co_2Cu_1 (~2.1 nm) particles. We observe the stable nanoparticles up to a size of 2.5 nm, which is the limit at which we can perform DFT calculations.

3.3.3 Global Optimization of CoCu(111) with Adsorbates

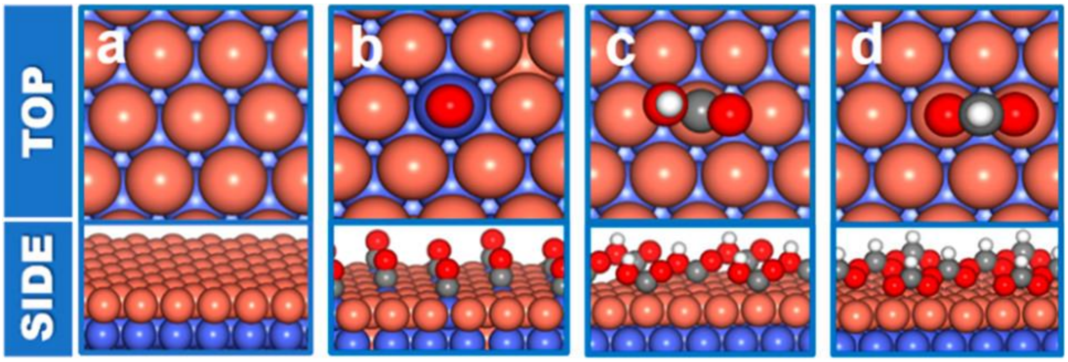

Figure 3.8 Top and side views of the most stable atomic configurations from global optimization calculations, (a) clean CoCu(111), surface with 0.11 ML of (b) *CO, (c) *COOH, and (d) HCOO*. Color scheme: O - red; H - white; C - gray; Cu - orange; Co - blue.

To verify the atomic segregation of CoCu alloys with adsorbates, slab models with (3 × 3) supercells of clean CoCu(111) surface and surfaces with key adsorbed species involved in hydrogenation reactions of CO and CO_2 (i.e., *CO, *COOH, and HCOO*) were globally optimized using genetic algorithm. The most stable surface structures are shown in Figure 3.8. In the absence of adsorbates, the surface is completely covered by a layer of Cu atoms (Figure 3.8a), which show the same segregation behavior as the clean particles. This is due to the lower surface energy of Cu compared to Co (Cu 1.934 $J \cdot m^{-2}$ versus Co 2.709 $J \cdot m^{-2}$)[86], in agreement with experimental observations in vacuum.[87] The second most stable configuration of clean CoCu(111) surface is formed by exchanging one subsurface Co atom with a surface Cu atom, which is destabilized by 0.53 eV versus the global minimum configuration.

Surface resegregation processes can occur in the presence of adsorbates. For instance, an adsorbed CO molecule pulls one subsurface Co atom to the surface (Figure 3.8b) due to a notable gain of energy from CO adsorption on top of Co. Interestingly, the expelled Cu atom prefers to stay in the subsurface layer. Forcing this Cu atom into deeper layers destabilizes the system by 0.3 eV. Contrary to CO adsorption, the adsorption of neither carboxyl nor formyl groups displays a strong enough preference for Co atoms to pull them to the surface (Figure 3.8c, d).

3.3.4 Adsorption Preference

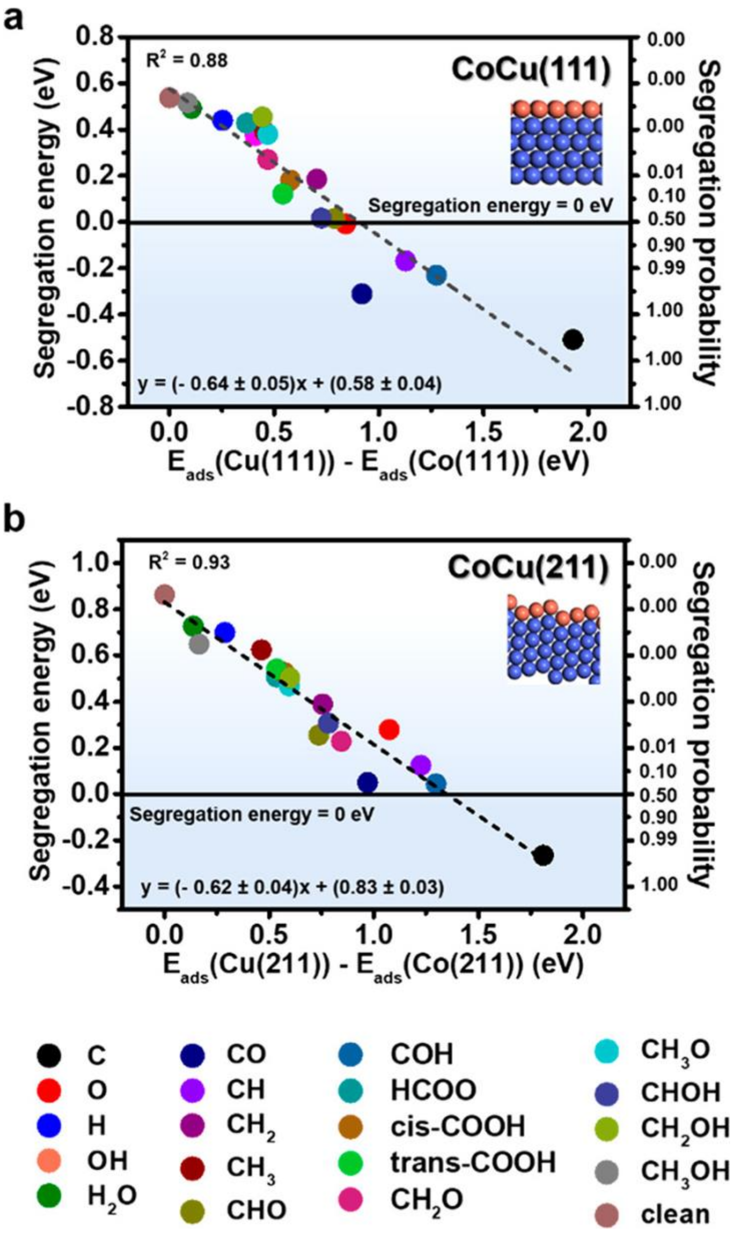

Figure 3.9 Scaling relations between adsorption preference (x axis) and segregation energy (y axis) over (a) CoCu(111), and (b) CoCu(211). The bottom inset displays the adsorbates in CO_2 hydrogenation towards C1 products.

Understanding the different reconstruction modes induced by these key intermediates is helpful to better portray the reactive surfaces. The present advanced optimizations enabled exploring the most stable surface morphologies via intensive computation, considering a large number of possible surface configurations. Unfortunately, the global DFT optimization remains too time-consuming, making it impractical to consider all significant adsorbed intermediates. Hence, reasonably simplified segregation analysis methodologies are needed to provide a conceptual model of how surface segregation is affected by various species involved in the surface reactions.

Adsorbates prefer stronger binding sites on which adsorption stabilizes the system by lowering the total energy. Metals constituting binary alloys (e.g., Co and Cu) often exhibit rather distinct adsorption abilities to the same adsorbate. Such adsorption preference may guide the adsorbate to build a preferred adsorption site, thus triggering surface segregation. In this way, the surface energy increase due to segregation can be compensated by enhanced adsorption. As a result, the surface composition of a certain alloy can be stabilized, modified, or even reversed, depending on the adsorption preference of the surface species.

Our calculations reveal that the segregation energy in the presence of a given adsorbate correlates with the adsorption preference. The latter concept is defined as the binding energy difference of an adsorbate over surfaces of pure metals that compose the bimetallic alloy. The involved equations are:

$$E_{seg} = E\left(Surf_{seg}\right) - E(Surf_{ori}) \tag{3.3.1}$$

$$E_{ads} = E_{slab/adsorbate} - (E_{slab} + E_{adsorbate}) \tag{3.3.2}$$

$$E_{AP}[CoCu(hkl)] = E_{ads}[Cu(hkl)] - E_{ads}[Co(hkl)] \tag{3.3.3}$$

$$segregation\,probability = \frac{\mathrm{e}^{-\mathrm{E_{seg}}/(\mathrm{kT})}}{e^{-E_{seg}/(kT)} + 1} \tag{3.3.4}$$

Here, the segregated surface, $Surf_{seg}$, is defined where one surface Cu atom is substituted by one Co atom from the subsurface layer, while the original surface, $Surf_{ori}$, is the globally optimized configuration. E_{seg} is the segregation energy, E_{ads} is the adsorption energy, $E_{slab/adsorbate}$ is the total energy of the surface with adsorbate, E_{slab} is the total energy of the clean surface, $E_{adsorbate}$ is the total energy of the free adsorbate, E_{AP} is the adsorption preference energy, *hkl* is the Miller index, segregation probability is derived from Boltzmann probability as a thermodynamic indicator for segregation induced by adsorbate, k is the Boltzmann constant, and T is the temperature (250 °C in our case, which is typical for CO_2 hydrogenation).

Noticeably, the adsorption preference energies scale linearly with the segregation energies (Figure 3.9). In the case of CoCu(111), the species around the leftmost region of the diagram (H*, H_2O*, CH_3O*H) show the weakest adsorption preference and thus leave the surface configuration unchanged with segregation probability as low as $\sim 10^{-4}$ at 250 °C. In contrast, *CO has a large adsorption preference of 0.88 eV and displays a high segregation probability of ~ 1 at the same temperature. The slope of −0.64 can be regarded as the sensitivity of surface segregation toward the adsorption preference. As the slope increases in magnitude, the driving force for segregation is also increased. In contrast, for alloy surfaces insensitive to adsorption preference, the segregation is less likely to be triggered by the reaction environment, and surface modification via interactions with given adsorbed species becomes difficult.

We extended the scaling relations to the CoCu(211) surface which shows good activity in CO hydrogenation reactions.[12] Only the row of edge Co sites was considered here because the inner part of the CoCu(211) surface resembles that of the CoCu(111) surface. Figure 3.9b shows that a linear relation is obtained, and the slope, −0.62, is nearly unchanged compared to its counterpart on the (111). This indicates different surface orientations might exhibit similar adsorption preferences in the case of CoCu binary alloys. The increased intercept from 0.58 to 0.83, on the other hand, implies that it should be more energetically demanding to segregate subsurface Co atoms to the step sites of CoCu(211). A notably stronger adsorption preference would hence be needed to reverse the segregation direction of CoCu(211). This surface segregation of Co could be induced, for example, by strongly binding species, such as adsorbed carbon atoms (the right-most data point in Figure 3.9b).

3.4 Conclusion

We successfully employed a neural network model that has been trained on a large number of DFT calculations of cuboctahedral $Co_{13}Cu_{42}$ particles to a series of CoCu-based particles with different sizes and compositions. The computational effort of this model scales linearly with particle size highlighting its wide range of applicability and efficiency. By combining this wACSF model with Monte Carlo simulations, the experimental phenomenon of Cu surface segregation in CoCu alloys was reproduced. We found that the outer two surface layers play a key role in the segregation process and tend to be occupied by Cu atoms. Through the analysis of the distribution of Co atoms on the surface, corner and edge sites were found to have the highest affinity to copper, followed by the (100) and (111) sites. These findings were not affected by the change in temperatures in our Monte Carlo simulations. There is a turning point for the formation of CoCu particles and only the particles larger than a certain size e.g., ~1.5 nm for Co_1Cu_1 particles, tend to form stable Co@Cu core-shell structures. Overall, we showed that the wACSF-MC method can be efficiently applied to investigate segregation processes in bimetallic particles.

Following the investigation of CoCu particles, segregation modes of alloy CoCu catalysts were quantified via global optimizations, which confirmed the copper-dominated surface in vacuum conditions and the strong ability of *CO and *C to draw Co atoms to the surface. The scaling relations between segregation energies and adsorption preferences were successfully applied to predict the probability of segregation on the studied bimetallic surfaces. The adsorption energy difference on pristine metal surfaces was calculated to control directions of segregation induced by different intermediates, providing a fast practical method to determine the surface composition of alloys with adsorbates.

4. Insights into the Mechanism of CO Hydrogenation on Segregated CoCu Catalysts[2]

4.1 Introduction

As we reported in Chapter 3, the continuously segregated Co atoms during the reaction give rise to the "dual-site" CoCu active centers, which has become a broad consensus.[13,24] However, the crucial and widespread Cu segregated surface at the early stage of reaction[18,21,22] and Co segregated surface at the late stage of reaction[22] haven't received any detailed atomic investigations for CO hydrogenation. Given the fact that these two kinds of surfaces don't have "visible" dual sites, the origin of reactivity for C_2 oxygenates is vague. A similar situation happened to the Rh catalyst which is a typical monometallic catalyst for C_2 oxygenates.[24] We would like to contribute to this discussion and see how a monometallic catalyst will serve like a "dual-site" catalyst.

In this chapter, we are going to shed light on the reactivity of these two kinds of rarely studied surfaces from an atomic perspective. According to our study shown in Chapter 3, the outer two layers of large CoCu particle play a key role in understanding the segregation phenomenon. Thus, four segregated CoCu(111) surfaces are collected as illustrated in Scheme 4.1 Cu terminated Cu/Co(111) and Cu_{2ML}/Co(111) are used to represent Cu segregated surfaces at the early stage of reaction and Co terminated Co/Cu(111) and Co_{2ML}/Cu(111) are used to represent Co segregated surfaces at the late stage of the reaction. The (111) facet is selected because of the observation of the (111) facet from XRD and HRTEM results.[22] The mechanisms of CO hydrogenation on these four surfaces are thoroughly explored.

---

[2] This chapter is based on the following publications: [1] Zha, S.; Sharapa, D.; Liu, S.; Zhao, Z.-J.; Studt, F. Insights into the Mechanism of CO Hydrogenation on Segregated CoCu Catalysts, in preparation.

4.2 Methods

Density Functional theory. VASP 5.4.4[81,88] was used to do DFT calculations with the BEEF-vdW functional[82,83]. Core electrons were treated using the PAW method.[84,85] Valence electrons were described using a plane-wave basis set with the cut-off energy of 400 eV. The CoCu(111) structures are modeled by using 4 × 4 × 4 slabs. The Brillouin zone was accordingly sampled using the Monkhorst-Pack method with a 3 × 3 × 1 grid. The dipole correction was added into the direction perpendicular to the slab surface. All the structures were optimized until the force on each atom is less than 0.02 eV/Å. The spin polarization is considered for all calculations. The transition states of the reactions were first roughly searched using the climbing nudged elastic band method[89], then located by the dimer method[90]. The final transition state structure is confirmed by only one existing imaginary frequency. All the potential energies and frequencies that appeared in this chapter can be retrieved from Table A2.1-4. The gas phases and the adsorbates on the surfaces were treated respectively using ideal gas approximation and harmonic approximation. All the imaginary frequencies smaller than 100 cm^{-1} are set to 12 cm^{-1}.[11]

Scheme 4.1 The reaction network from CO to methane, methanol, acetaldehyde, and ethanol, as well as the illustration of four segregated CoCu surfaces. Cu atoms are in bronze and Co atoms are in green.

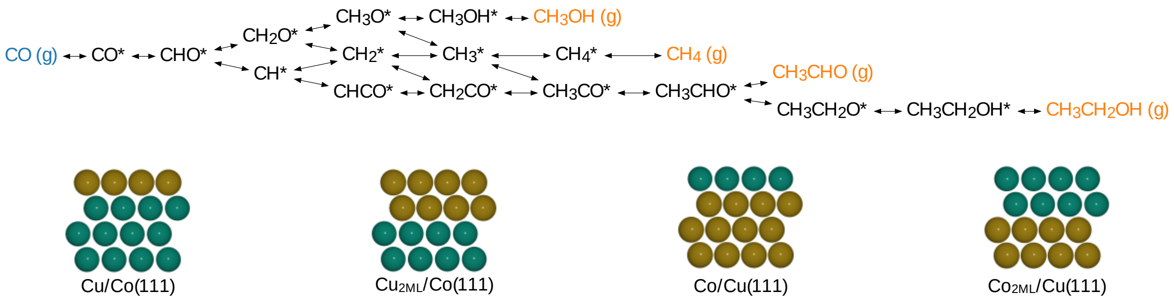

Microkinetic Modeling. The microkinetic modeling was done using CatMAP package[74] with the reaction network shown in Scheme 4.1 We used a complete reaction network to seek the intrinsic mechanism of CO hydrogenation. By default, two sites were included in the simulation. Those sites denoted with _h are for H* adsorbate, while the sites denoted with _s are for all other adsorbates.[10]

1. H_2_g + 2*_h → 2H*_h
2. CO_g + *_s → CO*_s
3. CO*_s + H*_h ↔ H-CO*_s + *_h → CHO*_s + *_h
4. CHO*_s + *_s ↔ O-CH*_s + *_s → CH*_s + O*_s
5. CHO*_s + H*_h ↔ H-CHO*_s + *_h → CH_2O*_s + *_h
6. CH*_s + CO*_s ↔ CO-CH*_s + *_s → CHCO*_s + *_s
7. CH*_s + H*_h ↔ H-CH*_s + *_h → CH_2*_s + *_h
8. CH_2O*_s + *_s ↔ O-CH_2*_s + *_s → CH_2*_s + O*_s
9. CH_2O*_s + H*_h ↔ H-CH_2O*_s + *_h → CH_3O*_s + *_h
10. CHCO*_s + H*_h ↔ H-CHCO*_s + *_h → CH_2CO*_s + *_h
11. CH_2*_s + CO*_s ↔ CO-CH_2*_s + *_s → CH_2CO*_s + *_s
12. CH_2*_s + H*_h ↔ H-CH_2*_s + *_h → CH_3*_s + *_h
13. CH_3O*_s + *_s ↔ O-CH_3*_s + *_s → CH_3*_s + O*_s
14. CH_3O*_s + H*_h ↔ H-CH_3O*_s + *_h → CH_3OH*_s + *_h
15. CH_2CO*_s + H*_h ↔ H-CH_2CO*_s + *_h → CH_3CO*_s + *_h
16. CH_3*_s + CO*_s ↔ CO-CH_3*_s + *_s → CH_3CO*_s + *_s
17. CH_3*_s + H*_h ↔ H-CH_3*_s + *_h → CH_4*_s + *_h
18. CH_3OH*_s → CH_3OH_g + *_s
19. CH_3CO*_s + H*_h ↔ H-CH_3CO*_s + *_h → CH_3CHO*_s + *_h
20. CH_4*_s → CH_4_g + *_s
21. CH_3CHO*_s + H*_h ↔ H-CH_3CHO*_s + *_h → CH_3CH_2O*_s + *_h
22. CH_3CH_2O*_s + H*_h ↔ H-CH_3CH_2O*_s + *_h → CH_3CH_2OH*_s + *_h
23. CH_3CH_2OH*_s → CH_3CH_2OH_g + *_s
24. O*_s + 2H*_h → H_2O*_s + 2*_h
25. H_2O*_s → H_2O_g + *_s

4.3 Results

4.3.1 CO* Hydrogenation and Dissociation

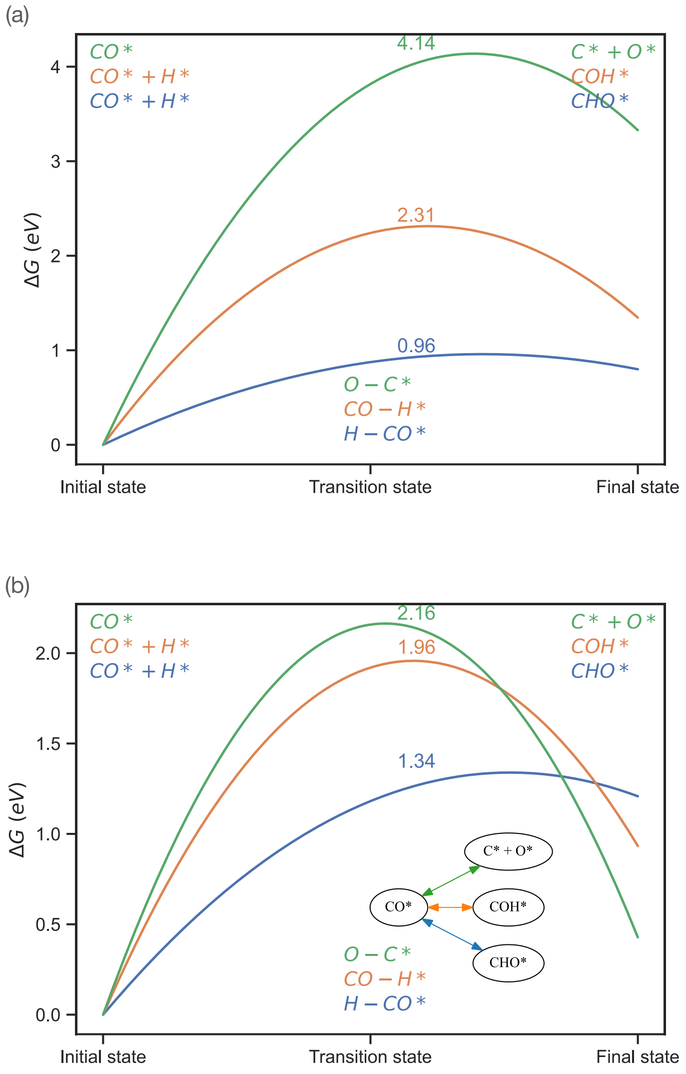

Figure 4.1 The competition between CO* hydrogenation and dissociation on (a) Cu/Co(111) and (b) Co/Cu(111).

As the first step to produce C_2 oxygenates, the CO* activation is crucial, and several mechanisms have been proposed (Figure 4.1). The carbide mechanism (CO* → C* + O*) indicating the direct dissociation of the CO* bond, the H-assisted CO* dissociation mechanism (CO* + H* → COH* or CO* + H* → CHO*) have all been investigated. From the results in Figure 4.1, the route from CO* to CHO* is always preferred for both Cu/Co and Co/Cu with free energy barriers of 0.96 eV and 1.34 eV, respectively. Thus, we didn't include the other two mechanisms in later calculations.

4.3.2 CH_XO* Hydrogenation and Dissociation

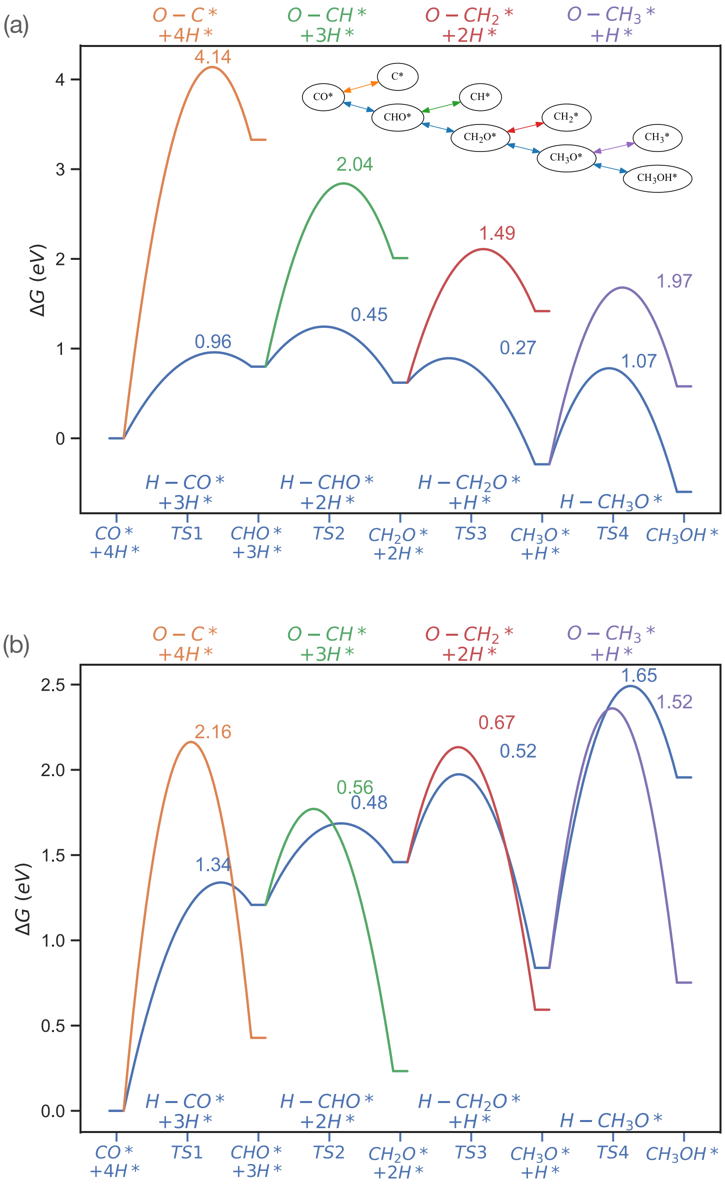

Figure 4.2 The competition between CH_XO* hydrogenation and dissociation on (a) Cu/Co(111) and (b) Co/Cu(111).

Although the whole reaction network from CO to C_2 oxygenates is sophisticated as shown in Scheme 4.1, the main thread still can be summed up based on the existing investigations. First, there is a competition existing between CH_XO^* (CHO^*, CH_2O^*, or CH_3O^*) hydrogenation and dissociation. The hydrogenation of CH_XO^* leads to the production of $CH_3OH(g)$, while the dissociation of CH_XO^* provides the CH_X^* intermediates (including CH^*, CH_2^*, or CH_3^*) as the precursors to C_2 oxygenates. Second, with the formation of CH_X^* intermediates, they can serve as precursors and accept the insertion of CO^*, which leads to CH_XCO^* ($CHCO^*$, CH_2CO^*, or CH_3CO). In the meantime, the hydrogenation of CH_X^* will be the competitor of the insertion process. Once CH_XCO^* intermediates have formed, the later hydrogenation to C_2 oxygenates (CH_3CHO (g) and CH_3CH_2OH (g)) is generally considered comparably feasible.

As to the specific case of Cu/Co(111) shown in Figure 4.2a, when comparing the free energy barriers of CH_XO^* hydrogenation (depicted in blue) and CH_XO^* scission (depicted in other colors), the free energy barriers of CH_XO^* hydrogenation is much lower than that of dissociation, which indicates CH_XO^* hydrogenation is thermodynamically preferred. Considering the large difference between CH_XO^* scission and hydrogenation, the reaction may follow the hydrogenation way from beginning to end, which causes the final production of CH_3OH. As a comparison, on Co terminated Co/Cu(111), the free energy differences between CHO^*, CH_2O^*, and CH_3O^* hydrogenation and scission are all less than 0.2 eV which is located in the error region of DFT calculations.[91] This fierce competition suggests the possible formation of CH_X^* intermediates on the Co/Cu surface. Note we didn’t include $CHOH^*$ intermediate[11] in our reaction network because free energy barriers of CHO^* hydrogenation to CH_2O^* are lower on all surfaces from our results (Figure A2.1).

4.3.3 CHx* Hydrogenation and CO* Insertion

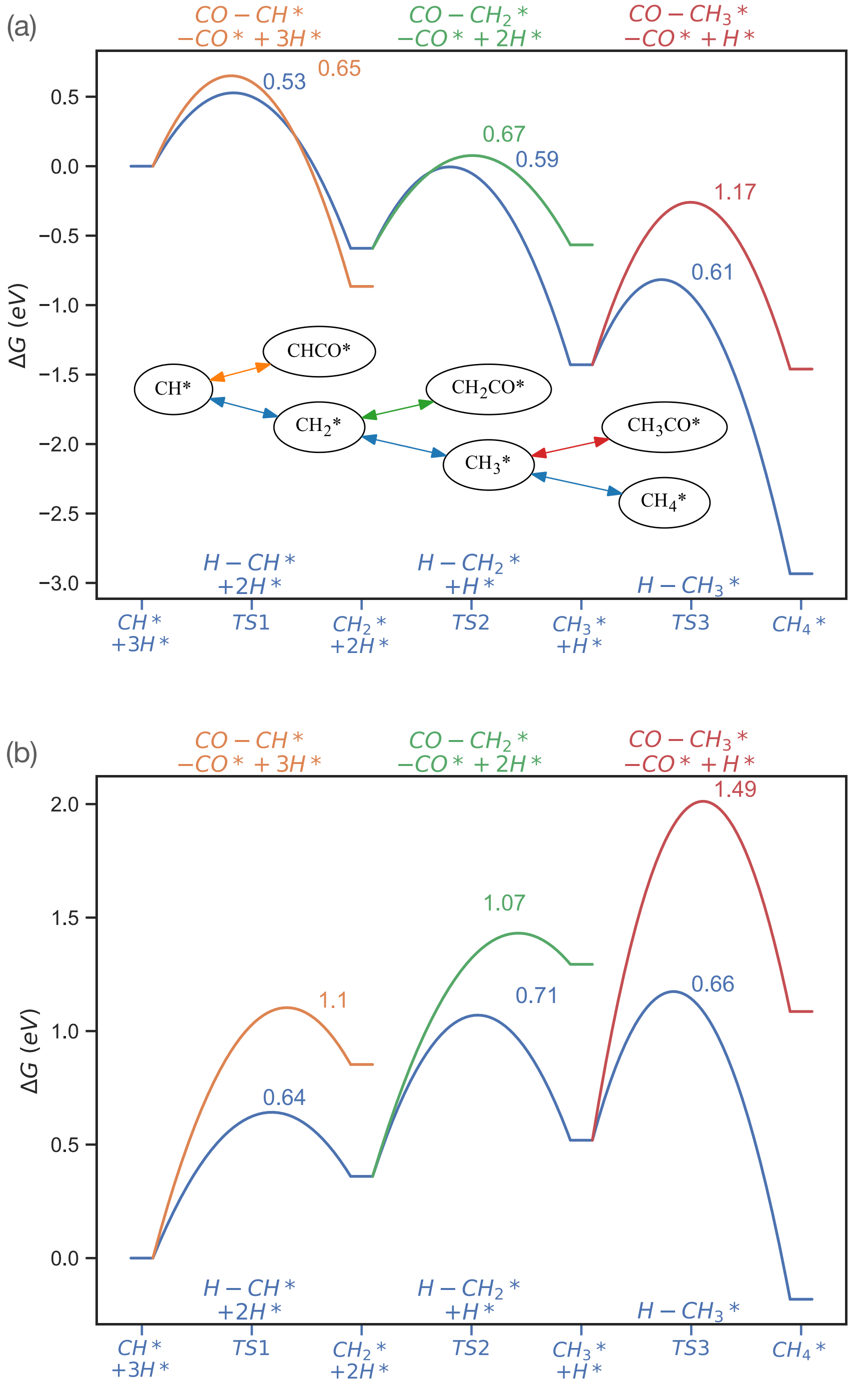

Figure 4.3 The competition between CHx* hydrogenation and CO* insertion on (a) Cu/Co(111) and (b) Co/Cu(111).

With the formation of CH_X* precursors, CO* insertion becomes the sequent crucial step. In Figure 4.3a, the close free energy barriers between CH_X* hydrogenation (depicted in blue) and CO* insertion (depicted in other colors) indicate the feasible CO insertion on Cu/Co(111). However, as suggested previously, Cu/Co cannot provide enough CH_X* intermediates for the formation of CH_XCO*, which may finally lead to low production of C_2 oxygenates. By contrast, the free energy differences between CH_X* hydrogenation and CO* insertion on Co/Cu (Figure 4.3b) are not so close as that on Cu/Co (Figure 4.3a). The free energy difference between CH_2* hydrogenation and CO* insertion is around 0.36 eV. With the possible company of abundant CH_X* intermediates, there is a possibility that CO* insertion happens on Co/Cu contributing to the high production of C_2 oxygenates. We must emphasize all the analyses above are based on thermodynamics which is qualitative. To gain a quantitative comprehension, microkinetic simulations are performed and the results are interpreted below.

4.3.4 Microkinetic Simulations

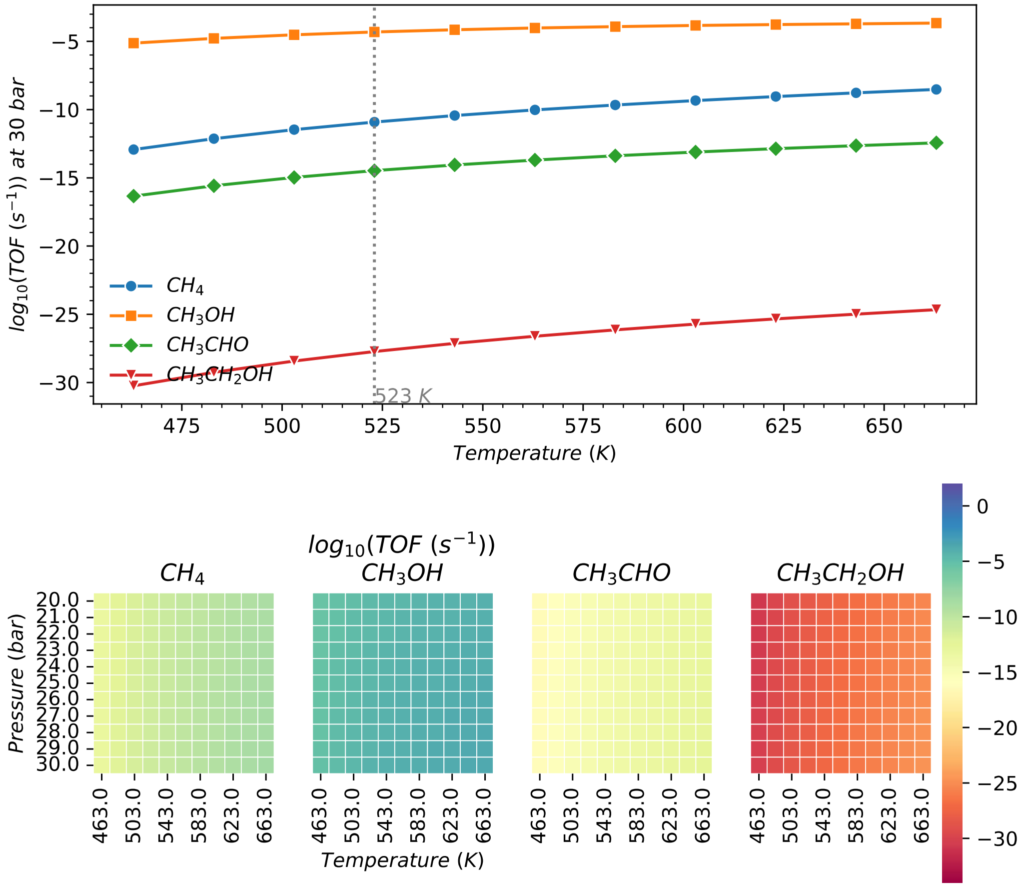

Figure 4.4 Turnover frequencies (TOF) of CH_4, CH_3OH, CH_3CHO, and CH_3CH_2OH on Cu/Co(111) under temperatures ranging from 463 K to 663 K and pressures ranging from 20 bar to 30 bar.

The microkinetic simulation based on mean-field approximation was first performed on Cu/Co(111) (Figure 4.4). In the whole range of temperatures from 463 to 663 K, the CH_3OH is the dominant product, while the second amount of product, CH_4 is several orders of magnitude lower than that of CH_3OH. The phenomenon confirmed what we analyzed from the thermodynamic perspective way that C_2 oxygenates are not desired and CH_3OH will be the predominant product on Cu/Co. Compared with the results of pure Cu that methanol is always the main product from CO hydrogenation[92], we may conclude that the addition of Co to the bottom three layers didn't bring an influential effect on the distribution of the products. From our calculation, we affirmed there is almost no C_2 oxygenates on fully Cu segregated surfaces. As reported in the literature, Cu segregated CoCu catalyst can produce a great amount of C_2 oxygenates[21,22], we will attribute the origin of reactivity to the small amount of Co atoms adjacent to the Cu atoms or the Co atoms segregated to the surface with the happening of the reaction.[9]

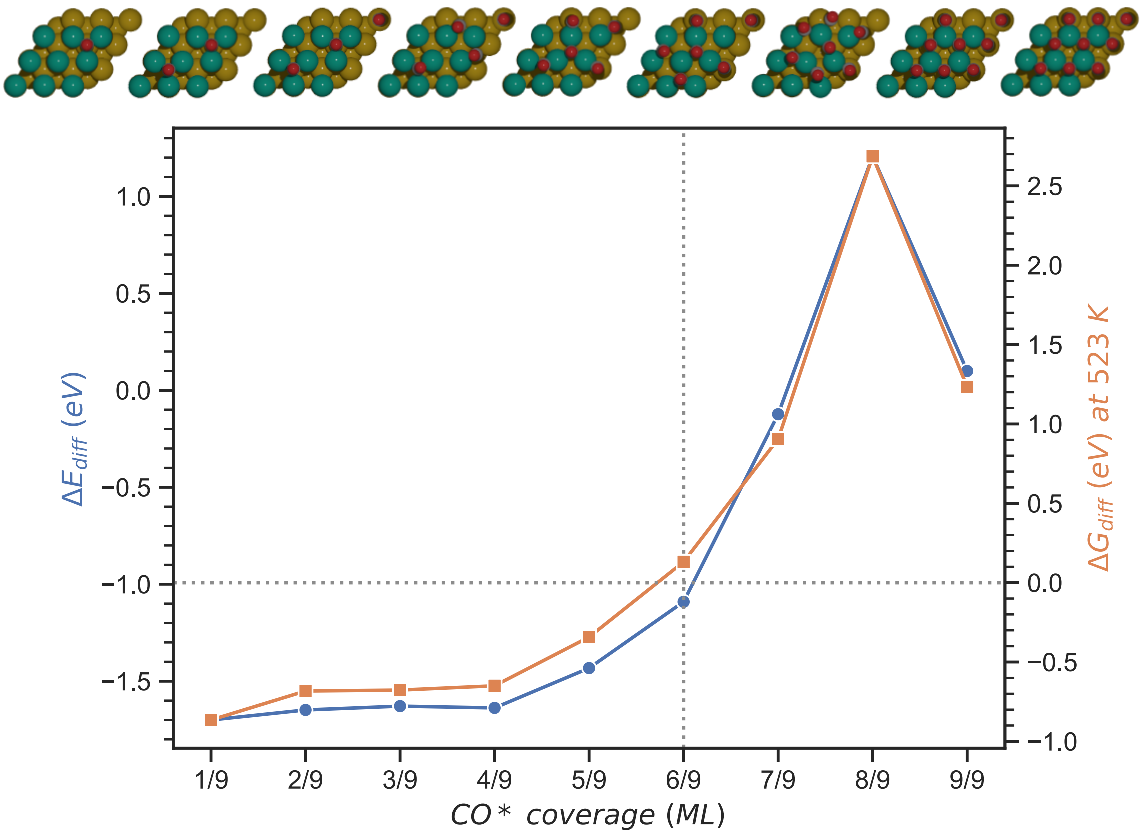

Figure 4.5 Coverage-dependent differential adsorption energies of CO* on the Co/Cu(111), the C and O atoms in CO* molecules are represented in black and red respectively.

As suggested in the literature, when the CO* adsorption is strong enough, the surface will be abundant with adsorbed CO* and there is a limiting coverage.[10] Thus, the coverage-dependent differential adsorption energies are calculated (Figure 4.5). As the convergence comes to 6/9 ML on Co/Cu(111), the ΔG_{diff} is no more negative, indicating the CO* turns into an unstable state on the surface. The maximum coverage of CO*, 6/9 ML, is used in our later microkinetic simulations. This is done by creating a "dummy" site denoted with _c for CO* adsorbate.

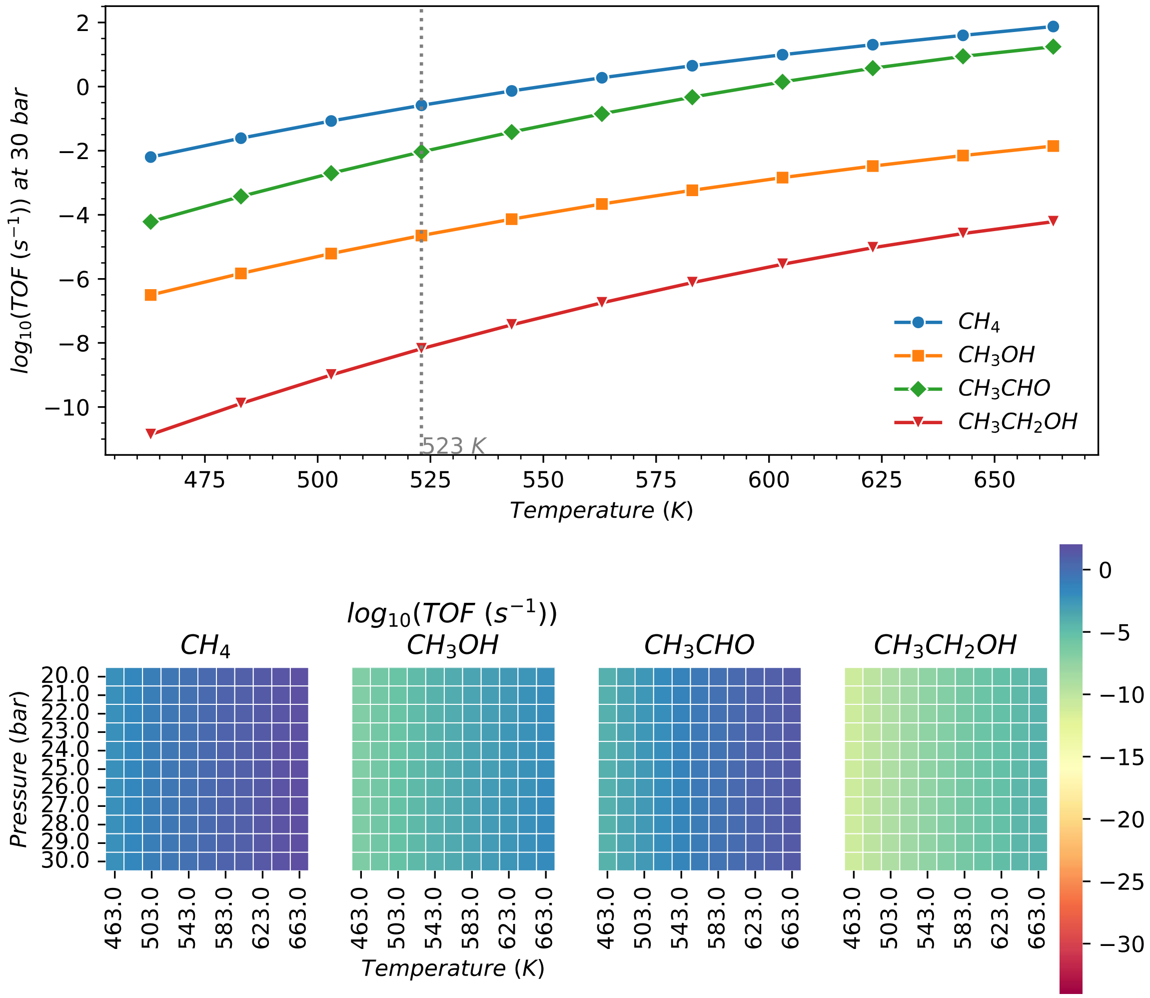

Figure 4.6 Turnover frequencies of CH_4, CH_3OH, CH_3CHO, and CH_3CH_2OH on Co/Cu(111) under different reaction conditions.

The microkinetic simulation results of Co/Cu(111) were shown in Figure 4.6. The CH_4 is the main product, closely followed by CH_3CHO (TOF of CH_4 is around 1 or 2 orders of magnitude higher than that of CH_3CHO). As we suggested in the analysis of free energy profiles, the hydrogenation of CH_X* is a little easier than CO* insertion. CH_4 is the main product on the Co/Cu surface. Besides, due to the abundance of formed CH_X*, C_2 oxygenates will also be massively produced. With the microkinetic results, we confirmed the assumption quantitively. Compared with the microkinetic results of Rh(211) which can produce C_2 oxygenates, the production of C_2 oxygenates on Co/Cu is at the same level as Rh(211), indicating the close catalytic reactivity of Co/Cu(111) to Rh(211)[10].

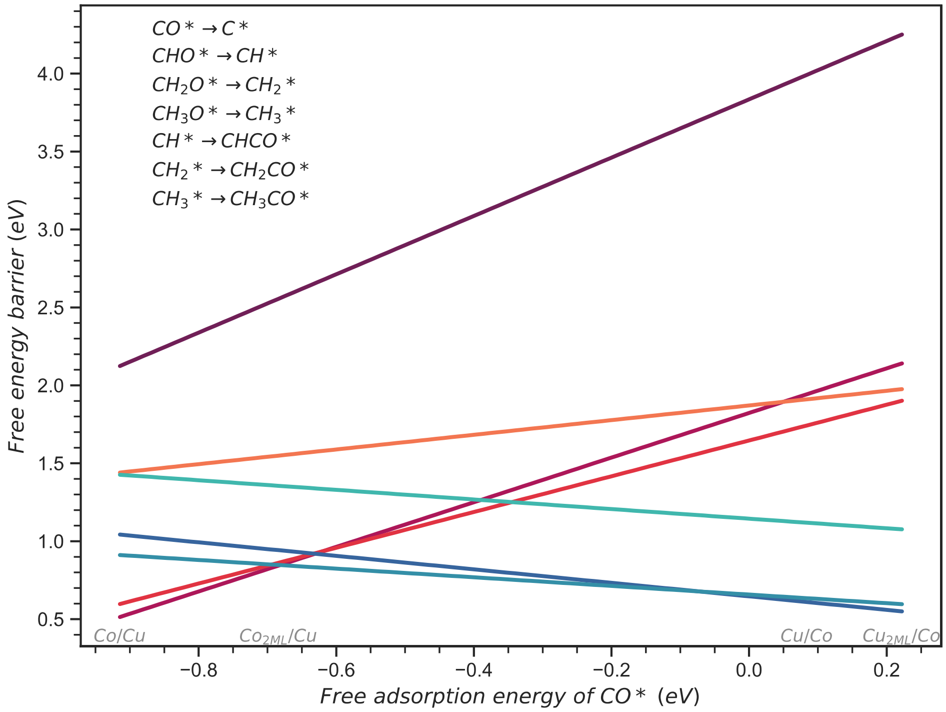

Figure 4.7 The scaling relationship between the free adsorption energy of CO* and free energy barriers on segregated CoCu surfaces. Free energy barriers of CH_XO* dissociation is depicted in different shades of red color and CO* insertion is depicted in different shades of green color.

According to Sabatier's principle[93,94], proper adsorption leads to the desired product, which perfectly describes the CoCu systems in the chapter. As to the CO hydrogenation reaction, the most significant adsorption is the adsorption of CO. According to the scaling relationship we found in Figure 4.7, the stronger the CO* adsorption is, the easier CH_xO* dissection is while the harder CO* insertion is.[7] The two important kinds of reaction barriers in CO hydrogenation are related to the CO* adsorption strength. It suggests CO* adsorption can be used as the key metric to measure the overall reactivity of CO hydrogenation.

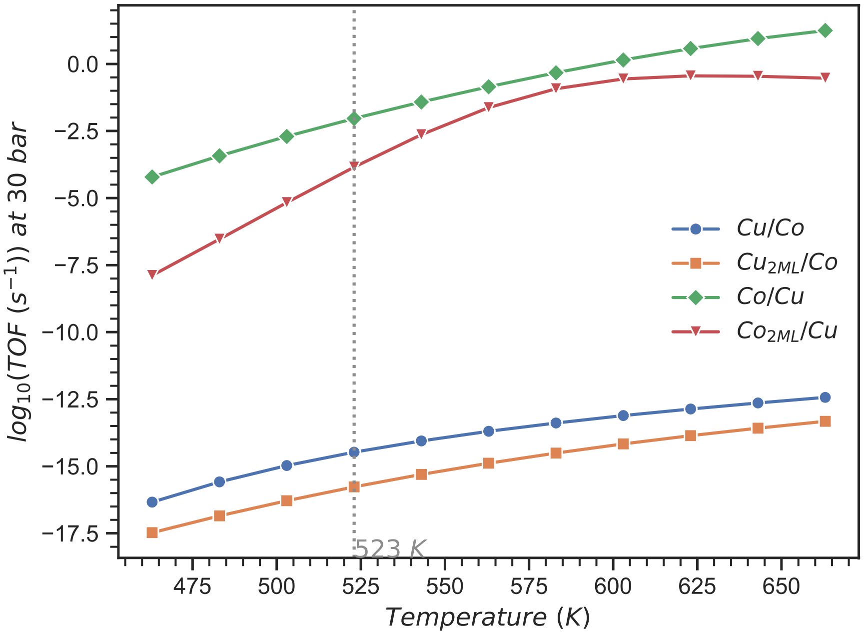

Figure 4.8 Turnover frequencies of C_2 oxygenates on segregated CoCu surfaces.

For Cu terminated surfaces (Cu/Co and Cu_{2ML}/Co), more Co appearing at the bottom brings more C_2 oxygenates (Figure 4.8). However, Cu/Co is still far away from the "proper adsorption" region, which reflects in the severely low production of C_2 oxygenates. In contrast, Co terminated surfaces (Co/Cu and Co_{2ML}/Cu) are close to the "proper adsorption" region, especially more Cu modified Co catalyst i.e., Co/Cu. This finding extends the generally recognized "dual-site" mechanism for C_2 oxygenate formation, from which one site is used for CHOx* dissociation and the other one is utilized for CO* insertion. From our results, if a proper balance between CHOx* dissociation and CO* insertion is reached, the superior performance for C_2 oxygenate formation will be attained even with only one type of active site on the surface. Similar cases like Rh based catalysts[10], and Co/SiO_2 catalysts[17] which only consist of one type of active site have already been reported to be active for the production of C_2 oxygenates.

4.4 Conclusion

Our results demonstrate the reactivity of fully segregated CoCu(111) surfaces for CO hydrogenation to C_2 oxygenates. The reactivity of Cu terminated surfaces i.e. Cu/Co(111) and Cu_{2ML}/Co(111) is close to pure Cu. Because of the strong tendency to hydrogenation, the only product will be methanol, and the production of C_2 oxygenates can be neglected. For Co terminated Co/Cu(111), the free energies of CO* dissociation are close to CO* hydrogenation, which brings enough CH_X* intermediates. Accompanied with a pronounced CO* insertion ability, Co/Cu(111) yields a comparable reactivity of C_2 oxygenates to methane. This is confirmed by our thermodynamic and kinetic analysis concurrently. By incorporating all the results, we claim the relativity of CO hydrogenation to C_2 oxygenates can be high as long as the balance between CH_XO* dissociation and CO* insertion is reached.

5. Kinetic Assessment of Partially Segregated CoCu Catalysts for CO Hydrogenation[3]

5.1 Introduction

Until now, all theoretical works related to CoCu catalysts focused on well-defined surfaces. The partially segregated CoCu surface during reaction [95] has never been mentioned. There are two stumbling blocks to the investigation of partially segregated surfaces. The first one is the possible surface configuration under the reaction conditions. The second obstacle is the consequent kinetic assessment of partially segregated surfaces which typically comes with a high CO coverage. To find a solution to high coverage systems, the kMC simulations with cluster expansion models and scaling relationships e.g. BEP relationship is a potential way.[75,73] However, the error BEP relationship brought is not trivial[96,97]. In addition to the complexity of the reaction network of CO hydrogenation, the exploration of partially segregated CoCu surface is still not available.

In this chapter, we shed light on the reactivity of partially segregated CoCu surfaces from an atomic perspective. We contributed to this topic by constructing the phase diagram and found the partially segregated surface. By using both MFT and kMC for a low coverage system, i.e. Cu/Co(111), the consistency between MFT and kMC was unveiled. On top of that, the partially segregated CoCu/Co(111) with a high CO coverage representing the real surface during the reaction was investigated.

---

[3] This chapter is based on the following publications: [1] Liu, S.; Yang, C.; Zha, S.; Sharapa, D.; Studt, F.; Zhao, Z.; Gong, J. Moderate Surface Segregation Promotes Selective Ethanol Production in CO_2 Hydrogenation Reaction over CoCu Catalysts. *Angew. Chem. Intl. Ed.* 2022, *61* (2). [2] Zha, S.; Sharapa, D.; Liu, S.; Zhao, Z.-J.; Studt, F. Kinetic Assessment of Partially Segregated CoCu Catalysts for CO Hydrogenation, in preparation.

5.2 Methods

Density Functional theory. VASP 5.4.4[81,88] was used to do DFT calculations with BEEF-vdW[82,83]. Core electrons were treated using the PAW method.[84,85] Valence electrons were described using a plane-wave basis set with the cut-off energy of 400 eV. $4 \times 4 \times 4$ slabs were used for Cu/Co(111), while $3 \times 3 \times 5$ slabs were used for CoCu/Co(111) shown in Scheme 5.1. The Brillouin zone was sampled using the Monkhorst-Pack method with a $3 \times 3 \times 1$ grid. The dipole correction was added into the direction perpendicular to the slab surface. All the structures were optimized until the force on each atom is less than 0.02 eV/Å. The spin polarization is considered for all calculations. The transition states of the reactions were first roughly searched using the climbing nudged elastic band method[89], then located by the dimer method[90]. The final transition state structure is confirmed by only one existing imaginary frequency. The potential energies and frequencies can be retrieved from Table A2.1-2, and Table A3.1. All the imaginary frequencies smaller than 100 cm^{-1} are set to 12 cm^{-1}.[11]

MFT and kMC. The microkinetic modeling was done using CatMAP package[74], and the elementary steps in the reaction network are listed below.

1. H_2_g + 2*_h → 2H*_h
2. CO_g + *_s → CO*_s
3. CO*_s + H*_h ↔ H-CO*_s + *_h → CHO*_s + *_h
4. CHO*_s + *_s ↔ O-CH*_s + *_s → CH*_s + O*_s
5. CHO*_s + H*_h ↔ H-CHO*_s + *_h → CH_2O*_s + *_h
6. CH*_s + CO*_s ↔ CO-CH*_s + *_s → CHCO*_s + *_s
7. CH*_s + H*_h ↔ H-CH*_s + *_h → CH_2*_s + *_h
8. CH_2O*_s + *_s ↔ O-CH_2*_s + *_s → CH_2*_s + O*_s
9. CH_2O*_s + H*_h ↔ H-CH_2O*_s + *_h → CH_3O*_s + *_h
10. CHCO*_s + H*_h ↔ H-CHCO*_s + *_h → CH_2CO*_s + *_h
11. CH_2*_s + CO*_s ↔ CO-CH_2*_s + *_s → CH_2CO*_s + *_s
12. CH_2*_s + H*_h ↔ H-CH_2*_s + *_h → CH_3*_s + *_h
13. CH_3O*_s + *_s ↔ O-CH_3*_s + *_s → CH_3*_s + O*_s

14. CH_3O*_s + H*_h ↔ H-CH_3O*_s + *_h → CH_3OH_g + *_s + *_h
15. CH_2CO*_s + H*_h ↔ H-CH_2CO*_s + *_h → CH_3CO*_s + *_h
16. CH_3*_s + CO*_s ↔ CO-CH_3*_s + *_s → CH_3CO*_s + *_s
17. CH_3*_s + H*_h ↔ H-CH_3*_s + *_h → CH_4_g + *_s + *_h
18. CH_3CO*_s + H*_h ↔ H-CH_3CO*_s + *_h → CH_3CHO_g + *_s + *_h
19. O*_s + 2H*_h → H_2O_g + *_s + 2*_h

Those sites denoted with _h are for H* adsorbate, while the sites denoted with _s are for all other adsorbates.[10]

As a comparison, a similar reaction network were used for kinetic Monte Carlo simulations using the kmos packages[79]. The acceleration algorithm developed by Dybeck et al.[98] was applied. The rate constants for the surface reactions and dissociative adsorption are given based on the transition state theory

$$k = \frac{k_B T}{h} \exp\left(\frac{-\Delta G}{k_\mathrm{B} T}\right) \tag{5.2.1}$$

where k_B, T, h, and ΔG are the Boltzmann constant, temperature, Planck constant, and the change in Gibbs energy. The rate constant for non-dissociative adsorption and desorption[75]

$$k_{ads,i} = \widetilde{S_\iota} \frac{p_i A}{\sqrt{2\pi m_i k_B T}} \tag{5.2.2}$$

$$k_{des,i} = k_{ads,i} \exp\left(\frac{-\Delta G_{ads,i}}{k_B T}\right) \tag{5.2.3}$$

where $\widetilde{S_\iota}$ is set to unity[75]. p_i, A, and m_i are the pressure of species i, the area of the unit cell, and the mass of species i.

5.3 Results

5.3.1 Phase Diagram of CoCu Catalysts

In Chapter 4, we found that adsorbed *CO induces segregation of Co.[29] To model the CoCu alloy, we chose a 5-layer 3×3 CoCu(111) surface as the catalyst model, which is large enough to describe surface segregation tendencies under different CO pressures and can also be subsequently used to calculate the hydrogenation reactions in detail. The temperatures are 473 K and 723K, corresponding to the reaction temperature applied in CO_2 hydrogenation reactions and CO pre-reduction temperature, respectively. To enhance the surface screening procedure, we applied a revised genetic algorithm to globally optimize *n*CO-(3×3)-CoCu(111) surfaces, with *n* ranges from 0 to 9, corresponding to surface coverages from 0 to 1ML. The global optimization method applied has not only accelerated the manual traversal by setting up the natural selection based on system energy but also included all possible surface configurations with multiple adsorbates, greatly enhancing the authenticity of as-organized surface phase diagrams.

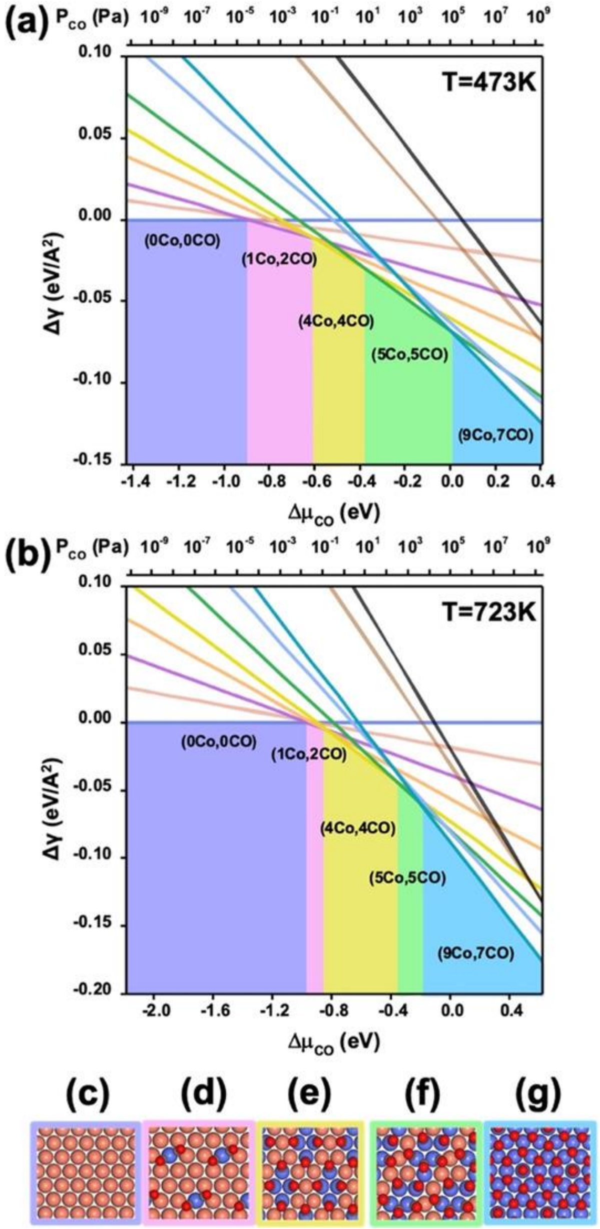

Figure 5.1 DFT-calculated thermodynamic surface phase diagram of CO adsorbed 3×3 CoCu(111) at (a) 473K and (b) 723K. The diagrams are exhibiting the Gibbs surface energy $\Delta\gamma$ (eV/A^2) as a function of CO chemical potential $\Delta\mu_{CO}$ (eV) or CO pressure (Pa). And the five screened-out regions are the surfaces of (c) (0ML Co, 0ML CO), (d) (1/9ML Co, 2/9ML CO), (e) (4/9ML Co, 4/9ML CO), (f) (5/9ML Co, 5/9ML CO) and (g) (1ML Co, 7/9ML CO). For each surface CO coverage, only the surface configuration with the lowest surface energy is shown in the phase diagram. Color: The brown, blue, grey, and red balls in the small boxes are representing copper, cobalt, carbon, and oxygen atoms respectively.

The obtained surface phase diagrams are shown in Figure 5.1. Within the wide range of studied CO pressures, there are five separate surface configurations (Figure 5.1c-g), with an increasing degree of cobalt segregation and consequent increasing CO surface coverage. Under UHV conditions ($< 10^{-7}$ Pa), the CoCu surface only exposes Cu atoms. Under typical CO/CO_2 hydrogenation reaction conditions, three surface phases might exist, (4/9ML Co, 4/9ML CO), (5/9ML Co, 5/9ML CO) and (1ML Co, 7/9ML CO). We define the former two as moderately segregated and the third as highly segregated, due to the segregation of a complete overlayer of cobalt to the surface. The adsorption of CO could drive reverse segregation of Co towards the surface, which results from the compensation of enhanced adsorption strength of CO on Co for the increase in surface energy. This has been thoroughly addressed in Chapter 3. As the temperature increases from 473K to 723K, the regions of (0ML Co, 0ML CO), (4/9ML Co, 4/9ML CO) and (1ML Co, 7/9ML CO) are enlarged, while the regions of (1/9ML Co, 2/9ML CO) and (5/9ML Co, 5/9ML CO) shrink, see Figure 5.1a and 5.2b. We discover that there are loosely binding CO molecules on (1/9ML Co, 2/9ML CO) and (5/9ML Co, 5/9ML CO), sharing one Co atom or adsorbing on the Co/Cu boundary, destabilizing the surface at a higher temperature. The segregation degree of Co not only changes the surface CO coverage but also the molecular adsorption configurations. The higher temperature undermines the thermal stability of surface configuration with loosely dangling, and thus narrows the existing interval of (1/9ML Co, 2/9ML CO) and (5/9ML Co, 5/9ML CO).

More interestingly, the segregated Co tends to form islands rather than be scattered. This phenomenon has been reported before, where Co clusters form on CoCu(110) in dynamic equilibrium with CO atmosphere.[99] With much stronger adsorption strength on cobalt than that on copper, CO prefers bonding on Co ensembles, leading to a relatively CO-free copper surface. This agrees well with the idea that the low coverage of reaction species on copper provides space for significant H_2 dissociative chemisorption, with the *CO and *H grouping on different sites over CoCu alloys.[49]

The surface phase diagrams in Figure 5.1 encompass the dual roles of surface segregation and coverage effect of key adsorbed species, taking one step closer to the realistic modeling of active sites over alloy surfaces. In the later discussions, the identified (5/9ML Co, 5/9ML CO) will be written as CoCu/Co(111) for simplicity.

Scheme 5.1 The reaction network from CO to methane, methanol, and acetaldehyde, as well as the illustration of Cu/Co(111) (representing the case of the low CO coverage) and CoCu/Co(111) (representing the case of high CO coverage). Cu atoms are in bronze and Co atoms are in green.

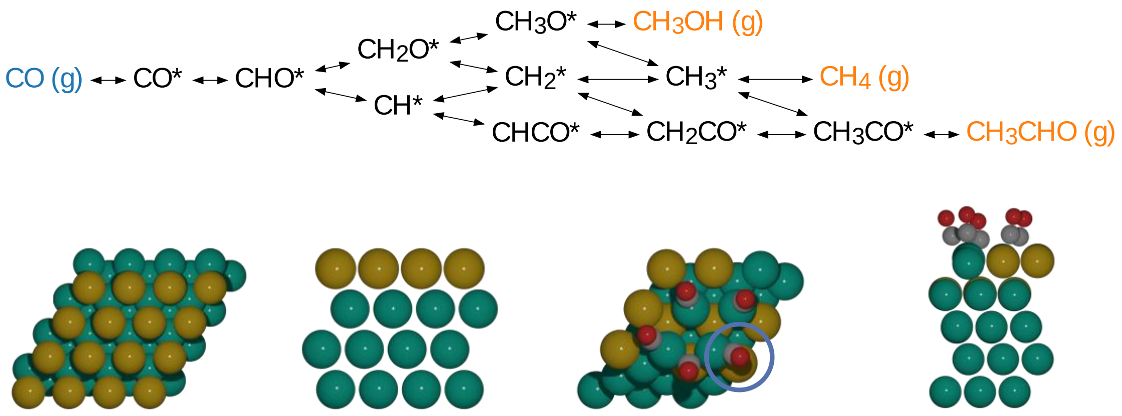

Cu/Co(111)
top view

Cu/Co(111)
front view

CoCu/Co(111)
(5/9 ML Co, 5/9 ML CO)
top view

CoCu/Co(111)
(5/9 ML Co, 5/9 ML CO)
front view

5.3.2 CO hydrogenation Mechanism

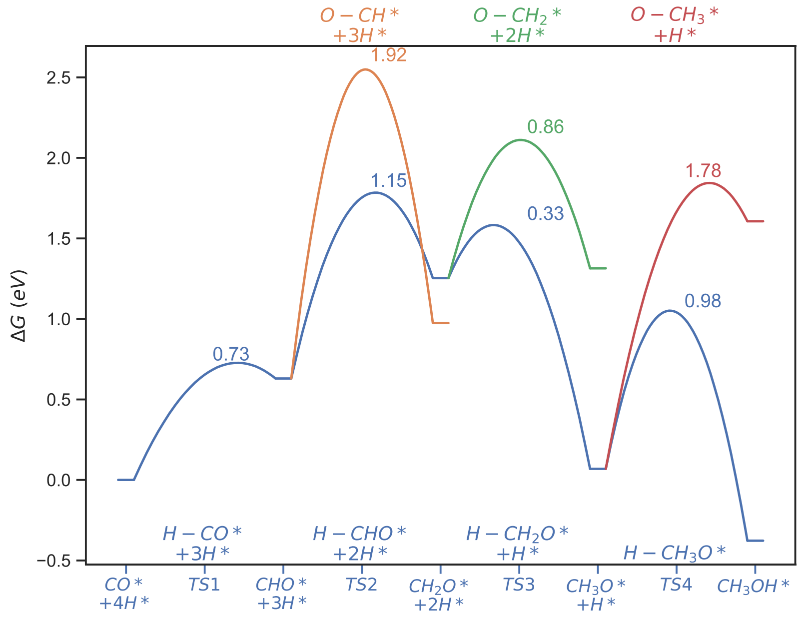

Figure 5.2 The competition between CHxO* hydrogenation and dissociation on CoCu/Co(111).

Most of the discussions for Cu/Co(111) were done in Chapter 4, and those results will be used for comparison only. In this chapter, we chose the H-assisted CO* dissociation mechanism (CO* + H* → CHO*) and didn't include CHOH* intermediate[11], which are based on the results in Chapter 4. The hydrogenation of CH_XO* (CHO*, CH_2O*, or CH_3O*) leads to the production of CH_3OH(g), while the dissociation of CH_XO* provides the CH_X* intermediates (CH*, CH_2*, or CH_3*) as the precursors to C_2 oxygenates. With the formation of CH_X* intermediates, they can accept the insertion of CO* leading to CH_XCO* (CHCO*, CH_2CO*, or CH_3CO). In the meantime, the hydrogenation of CH_X* heading to CH_4(g) will be the competitor to the insertion process. Once CH_XCO* intermediates have formed, the later hydrogenation to C_2 oxygenates (CH_3CHO (g)) is generally considered comparably feasible. Following the main thread, the competition existing between CH_XO* hydrogenation and dissociation were assessed. As shown in Figure 5.2, when comparing the free energy barriers of CH_XO* hydrogenation (depicted in blue) and CH_XO* dissociation (depicted in other colors), the free energy barriers of CH_XO* hydrogenation (in blue lines) are much lower than that of dissociation (in colorful lines) indicating CH_XO* hydrogenation is thermodynamically preferred. Considering the large energy difference between CH_XO* dissociation and hydrogenation, the reaction may follow the hydrogenation way from beginning to end, fostering the final production of CH_3OH(g).

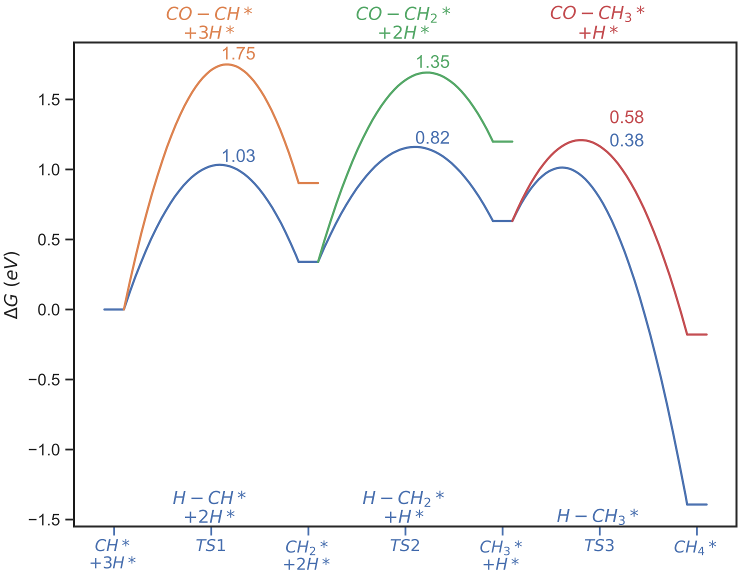

Figure 5.3 The competition between CH_X* hydrogenation and CO* insertion on CoCu/Co(111).

With the possible formation of CH_X* precursors, CO* insertion becomes the sequent crucial step. In Figure 5.3, the free energy barriers of CH_X* hydrogenation (in blue lines) is overall lower than that of CO* insertion (in colorful lines) implying the low possibility of CO insertion on CoCu/Co(111). Considering the insufficient CH_X* intermediates, the low production of C_2 oxygenates can be easily foreseen. To gain a quantitative comprehension, microkinetic results from MFT and kMC simulations will be demonstrated and compared below.

5.3.3 Scaling Relationship for CO Hydrogenation

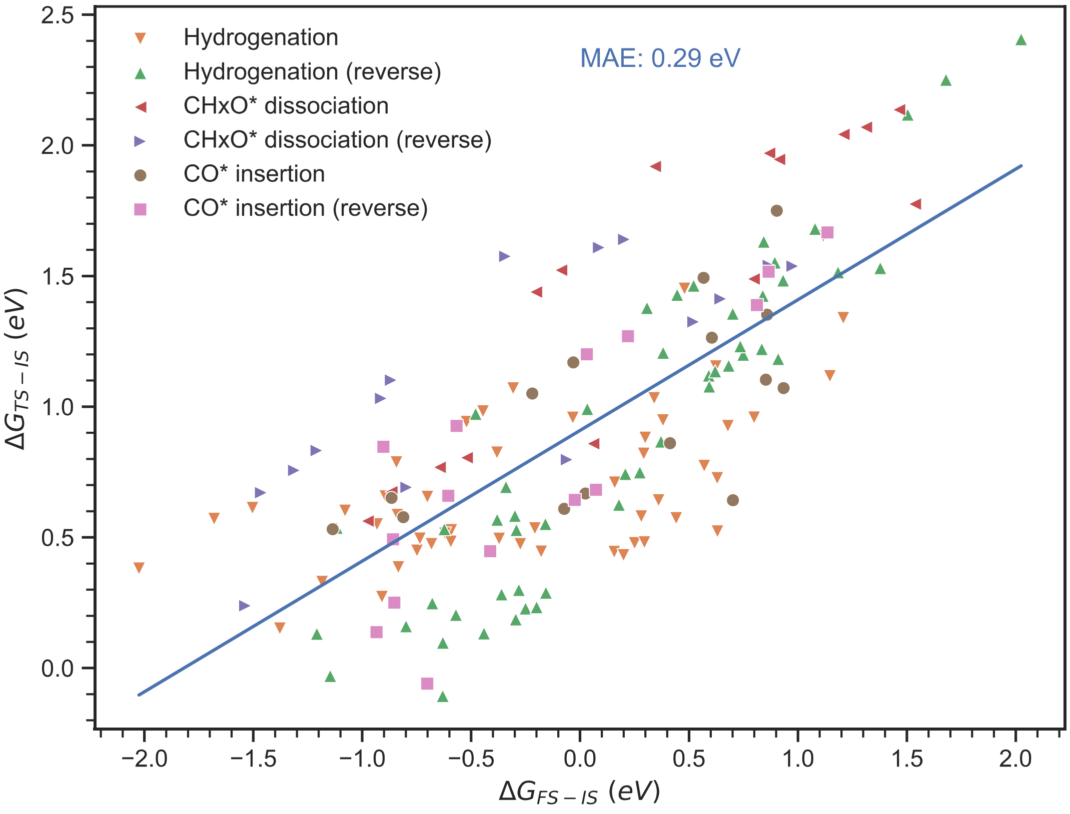

Figure 5.4 The BEP scaling relationship for CoCu systems containing Cu/Co(111), Cu_{2ML}/Co(111), Co/Cu(111), Co_{2ML}/Cu(111), and CoCu/Co(111). All elementary steps in CO hydrogenation are included. Color code: dehydrogenation in orange, hydrogenation (reverse) in green, CH_XO* dissociation in purple, CH_XO* dissociation (reverse) in red, CO* insertion in grey, CO* insertion (reverse) in pink.

Before diving into the microkinetic results, we may emphasize the pros and cons of the scaling relationship here. The calculations of transition state energies for a reaction consisting of many elementary reactions, e.g., CO hydrogenation are time-consuming and tedious, not to mention the extra obstacles caused by the high coverage. This situation calls for the introduction of scaling relationships and the computational time can be reduced to a large extent.[73,75,100] Figure 5.4 is a great example to show how the scaling relationship can help to predict the transition state energies. Following the definition of BEP relation, we collected all the data points for Cu/Co(111), Cu_{2ML}/Co(111), Co/Cu(111), Co_{2ML}/Cu(111), and CoCu/Co(111) in CO hydrogenation reaction, and tried to correlate the formation energies (ΔG_{FS-IS}) and transition state energies (ΔG_{TS-IS}). As demonstrated in Figure 5.4, a scaling relationship between formation energies and transition state energies was established including all the reaction types (Hydrogenation, CH_XO^* dissociation, CO* insertion, and their reverse reactions). The mean absolute error (MAE) of the data set is 0.29 eV which is close to the reported value.[96] Although, the value of MAE may not seem appealing, the scaling relationship constructed above still can be informative, especially for fast prediction or estimation of some missing data points.[100] However, the rate constant, the fundamental input to kMC, is sensitive to the values of transition state energies. A value like 0.29 eV corresponds to an error around 3 orders of magnitude in the rate constant. So large an error in the rate constant for every elementary step may lead to a different mechanism. Therefore, we didn't resort to the scaling relationship here. Instead, we chose to calculate all the energy profiles and frequencies in the reaction network DFT to keep the data points accurate and precise. The consequent shortcoming of this choice is the infeasibility of applying cluster expansion to the kMC simulations.

5.3.4 MFT vs kMC

The microkinetic simulation based on MFT was first performed on Cu/Co(111) and the detailed results can be found in Chapter 4. In the whole range of temperature from 463 to 663 K, the CH_3OH is the dominant product, while the second amount of product, CH_4 is several orders of magnitude lower than that of CH_3OH. The only adsorbate residing on the surface is CO* and the coverages stay in the low coverage zone, e.g., 0.13 at 523 K and 30 bar. The condition of low coverage on Cu/Co(111) provides an ideal condition to compare the results from MFT and kMC.[73,75]

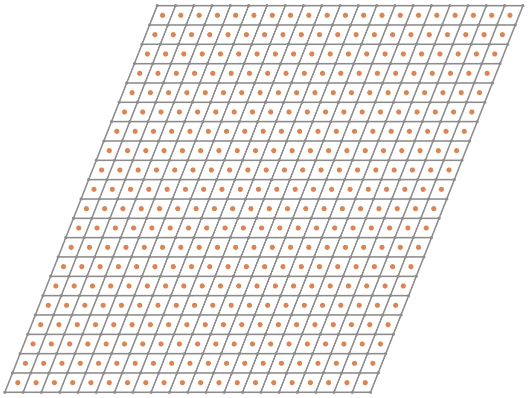

Figure 5.5 KMC lattice of Cu/Co(111) in simulations consisting of (20 × 20) unit cells. Reactants are in red.

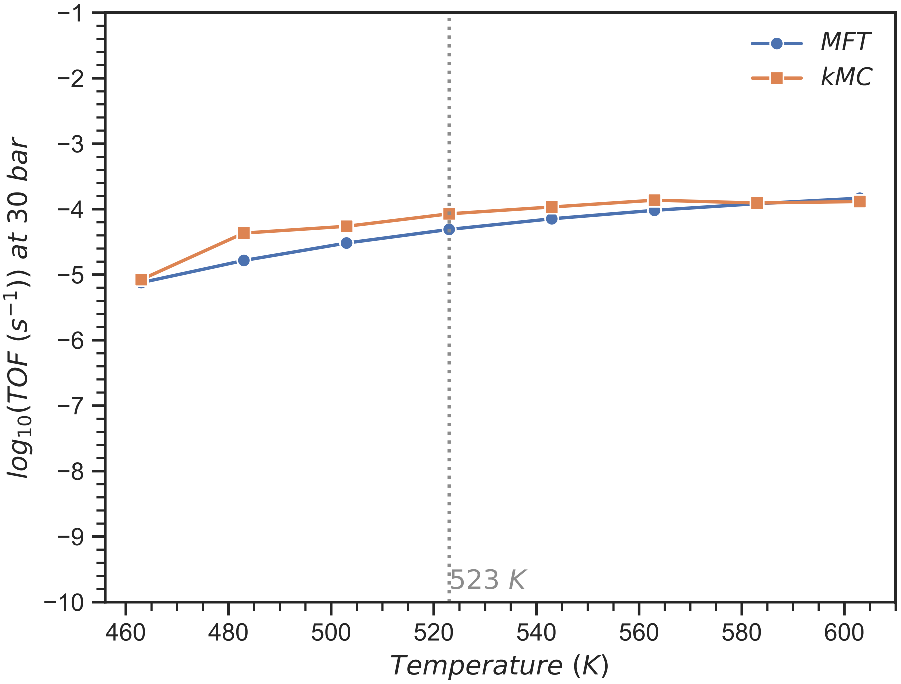

Figure 5.6 Turnover frequencies of methanol production on Cu/Co(111) at 30 bar.

For kMC simulations on Cu/Co(111), we mimicked all the settings in MFT and used a surface model containing (20 × 20) unit cells illustrated in Figure 5.5 In Figure 5.6, the kMC simulations were compared with MFT results under a series of temperatures. The dominant product from kMC is methanol the same as the result from MFT, and CO* is the only adsorbate possessing a noticeable but low coverage. Moreover, the TOF of methanol from kMC owns the same order of magnitude compared with that of MFT. Thus, we conclude the results from kMC and MFT quantitatively agree with each other under the conditions of infinitely fast diffusion and no adsorbate interactions. This conclusion is consistent with Hoffmann et al.'s investigation of CO oxidation.[73]

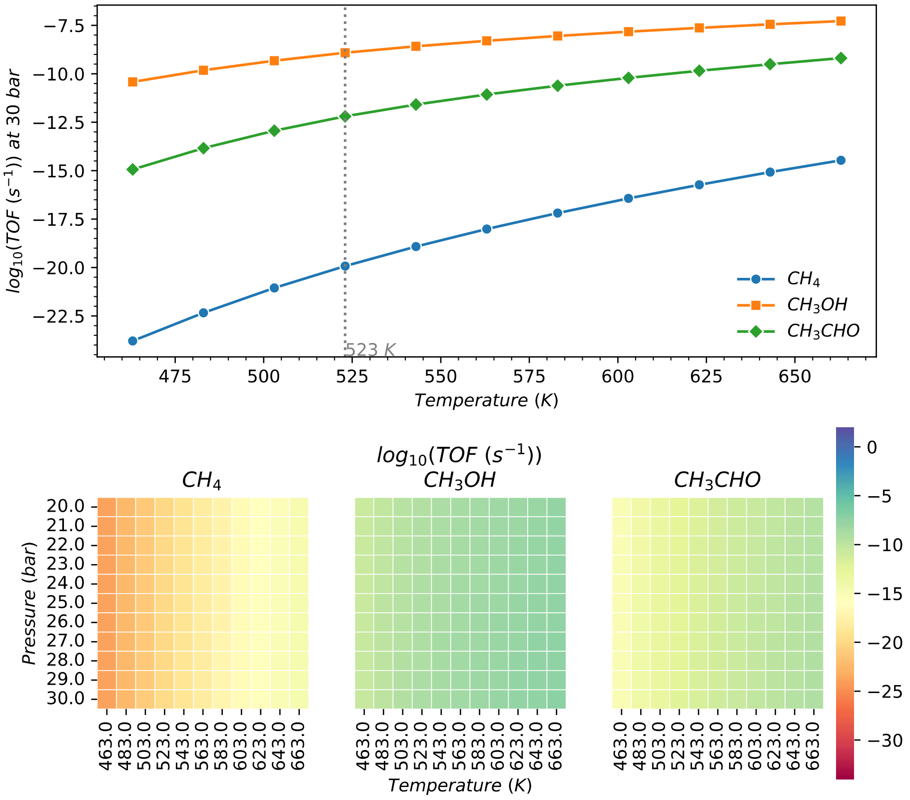

Figure 5.7 Turnover frequencies of CH_4, CH_3OH, and CH_3CHO on CoCu/Co(111) based on MFT under temperatures ranging from 463 K to 663 K and pressures ranging from 20 bar to 30 bar.

To go one step further, the microkinetic investigations were done for the high coverage system. First, the MFT results of CoCu/Co(111) were shown in Figure 5.7. Here, we assume one reactant (marked with a circle) is undergoing a unified external interaction with the 4 surrounding CO* molecules as illustrated in the top view of CoCu/Co(111) in Scheme 5.1. The MFT results in Figure 5.7 suggest CH_3OH as the main product, followed by CH_3CHO which is around 3 orders of magnitude lower. As we suggested in the analysis of free energy profiles, the hydrogenation of CH_XO* is much easier than CO* dissociation leading to the formation of CH_3OH, which we confirmed using the MFT results. With the help of kMC, the conclusion was further validated. We must note that cluster expansion is not included. As we mentioned above, introducing the BEP scaling relationship to circumvent the calculations of transition state energies may cause large errors in kMC simulations. In the meantime, calculating all the possible transition state energies for a complex reaction like CO hydrogenation under a series of coverages is still impractical. We chose a workable route, i.e., we fixed four surrounding CO* adsorbates that are ready to insert into the reactant in our kMC settings. Once one of those surrounding CO* is consumed, the CO* will be compensated immediately. Under this assumption, we did the simulation at 523 K and 30 bar of total pressure. The TOF of methanol is 1.27×10^{-9} s^{-1} per site. As a comparison, the TOF of methanol is 1.21×10^{-9} s^{-1} per site in MFT. The difference between kMC and MFT is negligible. This result confirmed the applicability of our MFT results for a high coverage circumstance.

5.4 Conclusion

Our work in this chapter demonstrates the reactivity of a fully segregated Cu/Co(111) surface, and a partially segregated CoCu/Co(111) surface for CO hydrogenation using both MFT and kMC simulations. Cu/Co(111) is an excellent example to symbolize the low coverage situation. Because of the strong tendency to hydrogenation, the only product will be methanol, and the production of C_2 oxygenates can be neglected, and the quantitively consistent results are from both MFT and kMC simulations. For CoCu/Co(111), a partially segregated surface with a high CO coverage, the free energy barriers of CH_XO^* dissociation are much higher than that of CH_XO^* hydrogenation, which leads to the dominant methanol production. This is confirmed by our thermodynamic and microkinetic analysis concurrently. The applicability of MFT and kMC was shown to this specific system with high coverage.

6. Final Conclusions and Outlook

This thesis thoroughly investigated the CoCu catalysts in CO hydrogenation.

For the pure CoCu particles, we employed a neural network model (wACSF) trained on a large number of DFT calculations of cuboctahedral $Co_{13}Cu_{42}$ particles to a series of CoCu-based particles with different sizes and compositions. The computational effort of this model scales linearly with particle size highlighting its wide range of applicability and efficiency. By combining this wACSF model with Monte Carlo simulations, the experimental phenomenon of Cu surface segregation in CoCu alloys was reproduced. We found that the outer two surface layers play a key role in the segregation process and tend to be occupied by Cu atoms. Through the analysis of the distribution of Co atoms on the surface, corner and edge sites were found to have the highest affinity to copper, followed by the (100) and (111) sites. These findings were not affected by the change in temperatures in our Monte Carlo simulations. There is a turning point for the formation of CoCu particles and only the particles larger than a certain size e.g., ~1.5 nm for Co_1Cu_1 particles, tend to form stable Co@Cu core-shell structures.

Following the investigation of CoCu particles, segregation modes of alloy CoCu catalysts were quantified via global optimizations, which confirmed the copper-dominated surface in vacuum conditions and the strong ability of *CO and *C to draw Co atoms to the surface. The scaling relations between segregation energies and adsorption preferences were successfully applied to predict the probability of segregation. The adsorption energy difference on pristine metal surfaces was calculated to control directions of segregation induced by different intermediates, providing a fast practical method to determine the surface composition of alloys with adsorbates.

Based on the fully segregated CoCu(111) surfaces for CO hydrogenation to C_2 oxygenates, we investigated the reactivity. The reactivity of Cu terminated surfaces i.e. Cu/Co(111) and Cu_{2ML}/Co(111) is close to pure Cu. Because of the strong tendency to hydrogenation, the only product will be methanol, and the production of C_2 oxygenates can be neglected. For Co terminated Co/Cu(111), the free energies of CO* dissociation are close to CO* hydrogenation, which brings enough CH_X* intermediates. Accompanied with a pronounced CO* insertion ability, Co/Cu(111) yields a comparable reactivity of C_2 oxygenates to methane. This is confirmed by our thermodynamic and kinetic analysis concurrently. By incorporating all the results, we claim the relativity of CO hydrogenation to C_2 oxygenates can be high as long as the balance between CH_XO* dissociation and CO* insertion is reached.

To investigate the CoCu surface during the reaction, the surface phase diagrams were constructed. The segregated Co atoms tend to form islands rather than be scattered. The identified partially segregated Cu/Co(111) surface (5/9ML Co, 5/9ML CO) takes one step closer to the realistic modeling of active sites. Based on these results, we demonstrate the reactivity of a fully segregated Cu/Co(111) surface and a partially segregated CoCu/Co(111) surface for CO hydrogenation using both MFT and kMC simulations. Cu/Co(111) is an excellent example to symbolize the low coverage situation. Because of the strong tendency to hydrogenation, the only product will be methanol, and the production of C_2 oxygenates can be neglected, and the quantitively consistent results are from both MFT and kMC simulations. For CoCu/Co(111), a partially segregated surface with a high CO coverage, the free energy barriers of CH_XO* dissociation are much higher than that of CH_XO* hydrogenation, which leads to the dominant methanol production. This is confirmed by our thermodynamic and microkinetic analysis concurrently. The applicability of MFT and kMC was shown to this specific system with high coverage.

Overall, we built the structure-performance relationship for CO hydrogenation over CoCu catalysts from the early stage to the late stage of the reaction.

Future work will focus on the more realistic modeling of the CoCu surface during the reaction. The surface segregation of Co or Cu could be influenced by different external conditions, *e.g.*, CO partial pressure. Considering the existence of H_2O and other potential oxidizers in the hydrogenation process, the alloy surface could be partially oxidized. Thus, the models applied in this thesis only encompass surface segregation and the consequent coverage effect. The models are not necessarily identical to exact active surfaces in experiments. In addition, a more sophisticated kMC simulation with cluster expansion will be required for a more realistic CoCu catalyst.

References

1. U.S. Energy Information Administration. International Energy Outlook 2021. (2021).
2. Bushuyev, O. S. *et al.* What Should We Make with CO_2 and How Can We Make It? *Joule* **2**, 825–832 (2018).
3. Chorkendorff, I. & Niemantsverdriet, J. W. *Concepts of Modern Catalysis and Kinetics*. (Wiley, 2003).
4. Puga, A. V. On the nature of active phases and sites in CO and CO_2 hydrogenation catalysts. *Catal. Sci. Technol.* **8**, 5681–5707 (2018).
5. Studt, F. *et al.* Identification of Non-Precious Metal Alloy Catalysts for Selective Hydrogenation of Acetylene. *Science* **320**, 1320–1322 (2008).
6. van Santen, R. A., Markvoort, A. J., Filot, I. A. W., Ghouri, M. M. & Hensen, E. J. M. Mechanism and microkinetics of the Fischer–Tropsch reaction. *Phys. Chem. Chem. Phys.* **15**, 17038 (2013).
7. Medford, A. J. *et al.* Activity and Selectivity Trends in Synthesis Gas Conversion to Higher Alcohols. *Top. Catal.* **57**, 135–142 (2014).
8. Xu, X.-C. *et al.* First-Principles Study of C_2 Oxygenates Synthesis Directly from Syngas over CoCu Bimetallic Catalysts. *J. Phys. Chem. C* **119**, 216–227 (2015).
9. Zhang, R., Liu, F. & Wang, B. Co-decorated Cu alloy catalyst for C_2 oxygenate and ethanol formation from syngas on Cu-based catalyst: insight into the role of Co and Cu as well as the improved selectivity. *Catal. Sci. Technol.* **6**, 8036–8054 (2016).
10. Yang, N. *et al.* Intrinsic Selectivity and Structure Sensitivity of Rhodium Catalysts for C_{2+} Oxygenate Production. *J. Am. Chem. Soc.* **138**, 3705–3714 (2016).
11. Schumann, J. *et al.* Selectivity of Synthesis Gas Conversion to C_{2+} Oxygenates on fcc(111) Transition-Metal Surfaces. *ACS Catal.* **8**, 3447–3453 (2018).
12. Cao, A. *et al.* Mechanistic Insights into the Synthesis of Higher Alcohols from Syngas on CuCo Alloys. *ACS Catal.* **8**, 10148–10155 (2018).
13. Luk, H. T., Mondelli, C., Ferré, D. C., Stewart, J. A. & Pérez-Ramírez, J. Status and prospects in higher alcohols synthesis from syngas. *Chem. Soc. Rev.* **46**, 1358–1426 (2017).
14. Liu, L. & Corma, A. Metal Catalysts for Heterogeneous Catalysis: From Single Atoms to Nanoclusters and Nanoparticles. *Chem. Rev.* **118**, 4981–5079 (2018).

15. Wang, W., Wang, S., Ma, X. & Gong, J. Recent advances in catalytic hydrogenation of carbon dioxide. *Chem. Soc. Rev.* **40**, 3703 (2011).

16. Spivey, J. J. & Dooley, K. M. Promotion Effects in Co-based Fischer–Tropsch Catalysis. in *Catalysis* vol. 19 1–40 (2006).

17. Baker, J. E., Burch, R., Hibble, S. J. & Loader, P. K. Properties of silica-supported Cu/Co bimetallic catalysts in the synthesis of higher alcohols. *Appl. Catal.* **65**, 281–292 (1990).

18. Subramanian, N. D., Balaji, G., Kumar, C. S. S. R. & Spivey, J. J. Development of cobalt–copper nanoparticles as catalysts for higher alcohol synthesis from syngas. *Catal. Today* **147**, 100–106 (2009).

19. Fang, Y. Z., Liu, Y. & Zhang, L. H. $LaFeO_3$-supported nano Co-Cu catalysts for higher alcohol synthesis from syngas. *Appl. Catal. Gen.* **397**, 183–191 (2011).

20. Prieto, G. *et al.* Design and Synthesis of Copper–Cobalt Catalysts for the Selective Conversion of Synthesis Gas to Ethanol and Higher Alcohols. *Angew. Chem. Int. Ed.* **53**, 6397–6401 (2014).

21. Xiang, Y., Barbosa, R. & Kruse, N. Higher Alcohols through CO Hydrogenation over CoCu Catalysts: Influence of Precursor Activation. *ACS Catal.* **4**, 2792–2800 (2014).

22. Yang, Q. *et al.* Bimetallic Nano Cu–Co Based Catalyst for Direct Ethanol Synthesis from Syngas and Its Structure Variation with Reaction Time in Slurry Reactor. *Ind. Eng. Chem. Res.* **56**, 2889–2898 (2017).

23. Göbel, C. *et al.* Structural evolution of bimetallic Co-Cu catalysts in CO hydrogenation to higher alcohols at high pressure. *J. Catal.* **383**, 33–41 (2020).

24. Ao, M., Pham, G. H., Sunarso, J., Tade, M. O. & Liu, S. Active Centers of Catalysts for Higher Alcohol Synthesis from Syngas: A Review. *ACS Catal.* **8**, 7025–7050 (2018).

25. Alayoglu, S. *et al.* Surface Composition Changes of Redox Stabilized Bimetallic CoCu Nanoparticles Supported on Silica under H_2 and O_2 Atmospheres and During Reaction between CO_2 and H_2: In Situ X-ray Spectroscopic Characterization. *J. Phys. Chem. C* **117**, 21803–21809 (2013).

26. Wang, B., Chen, X., Chen, G., Wang, G. & Zhao, J. Magnetic Properties of Icosahedral Copper-Coated Cobalt Clusters. *Surf. Rev. Lett.* **11**, 15–20 (2004).

27. Shim, J.-H., Lee, B.-J., Ahn, J.-P., Cho, Y. W. & Park, J.-K. Monte Carlo Simulation of Phase Separation Behavior in a Cu-Co Alloy Nanoparticle. *J. Mater. Res.* **17**, 925–928 (2002).

28. Dzhurakhalov, A. A. & Hou, M. Equilibrium properties of binary and ternary metallic immiscible nanoclusters. *Phys. Rev. B* **76**, 045429 (2007).

29. Liu, S. *et al.* Adsorption Preference Determines Segregation Direction: A Shortcut to More Realistic Surface Models of Alloy Catalysts. *ACS Catal.* **9**, 5011–5018 (2019).

30. Sabbe, M. K., Reyniers, M.-F. & Reuter, K. First-principles kinetic modeling in heterogeneous catalysis: an industrial perspective on best-practice, gaps and needs. *Catal. Sci. Technol.* **2**, 2010 (2012).

31. Kozlov, S. M., Kovács, G., Ferrando, R. & Neyman, K. M. How to determine accurate chemical ordering in several nanometer large bimetallic crystallites from electronic structure calculations. *Chem. Sci.* **6**, 3868–3880 (2015).

32. Stephens, I. E. L., Bondarenko, A. S., Grønbjerg, U., Rossmeisl, J. & Chorkendorff, I. Understanding the electrocatalysis of oxygen reduction on platinum and its alloys. *Energy Environ. Sci.* **5**, 6744 (2012).

33. Hohenberg, P. & Kohn, W. Inhomogeneous Electron Gas. *Phys. Rev.* **136**, B864–B871 (1964).

34. Koch, W. & Holthausen, M. C. *A Chemist's Guide to Density Functional Theory*. (Wiley, 2001).

35. Perdew, J. P. *et al.* Atoms, molecules, solids, and surfaces: Applications of the generalized gradient approximation for exchange and correlation. *Phys. Rev. B* **46**, 6671–6687 (1992).

36. Perdew, J. P., Burke, K. & Ernzerhof, M. Generalized Gradient Approximation Made Simple. *Phys. Rev. Lett.* **77**, 3865–3868 (1996).

37. Hammer, B., Hansen, L. B. & Nørskov, J. K. Improved adsorption energetics within density-functional theory using revised Perdew-Burke-Ernzerhof functionals. *Phys. Rev. B* **59**, 7413–7421 (1999).

38. Sun, J. *et al.* Self-consistent meta-generalized gradient approximation within the projector-augmented-wave method. *Phys. Rev. B* **84**, 035117 (2011).

39. Stephens, P. J., Devlin, F. J., Chabalowski, C. F. & Frisch, M. J. Ab Initio Calculation of Vibrational Absorption and Circular Dichroism Spectra Using Density Functional Force Fields. *J. Phys. Chem.* **98**, 11623–11627 (1994).

40. Adamo, C. & Barone, V. Toward reliable density functional methods without adjustable parameters: The PBE0 model. *J. Chem. Phys.* **110**, 6158–6170 (1999).

41. Johnston, R. L. Evolving better nanoparticles: Genetic algorithms for optimising cluster geometries. *Dalton Trans.* **0**, 4193–4207 (2003).

42. Grajciar, L. *et al.* Towards *operando* computational modeling in heterogeneous catalysis. *Chem. Soc. Rev.* **47**, 8307–8348 (2018).

43. Wales, D. J. & Doye, J. P. K. Global Optimization by Basin-Hopping and the Lowest Energy Structures of Lennard-Jones Clusters Containing up to 110 Atoms. *J. Phys. Chem. A* **101**, 5111–5116 (1997).

44. Heard, C. J. & Johnston, R. L. A density functional global optimisation study of neutral 8-atom Cu-Ag and Cu-Au clusters. *Eur. Phys. J. D* **67**, 34 (2013).

45. Heard, C. J. & Johnston, R. L. Global Optimisation Strategies for Nanoalloys. in *Clusters* (eds. Nguyen, M. T. & Kiran, B.) vol. 23 1–52 (Springer International Publishing, 2017).

46. Lysgaard, S., Landis, D. D., Bligaard, T. & Vegge, T. Genetic Algorithm Procreation Operators for Alloy Nanoparticle Catalysts. *Top. Catal.* **57**, 33–39 (2014).

47. Zhao, J., Shi, R., Sai, L., Huang, X. & Su, Y. Comprehensive genetic algorithm for *ab initio* global optimisation of clusters. *Mol. Simul.* **42**, 809–819 (2016).

48. Vilhelmsen, L. B. & Hammer, B. Systematic Study of Au_6 to Au_{12} Gold Clusters on MgO(100) *F* Centers Using Density-Functional Theory. *Phys. Rev. Lett.* **108**, 126101 (2012).

49. Vilhelmsen, L. B. & Hammer, B. Interfacial oxygen under TiO_2 supported Au clusters revealed by a genetic algorithm search. *J. Chem. Phys.* **139**, 204701 (2013).

50. Vilhelmsen, L. B. & Hammer, B. Identification of the Catalytic Site at the Interface Perimeter of Au Clusters on Rutile TiO_2(110). *ACS Catal.* **4**, 1626–1631 (2014).

51. Vilhelmsen, L. B., Walton, K. S. & Sholl, D. S. Structure and Mobility of Metal Clusters in MOFs: Au, Pd, and AuPd Clusters in MOF-74. *J. Am. Chem. Soc.* **134**, 12807–12816 (2012).

52. Heiles, S. & Johnston, R. L. Global optimization of clusters using electronic structure methods. *Int. J. Quantum Chem.* **113**, 2091–2109 (2013).

53. Wales, D. J. Global Optimization of Clusters, Crystals, and Biomolecules. *Science* **285**, 1368–1372 (1999).

54. Boes, J. R. & Kitchin, J. R. Modeling Segregation on AuPd(111) Surfaces with Density Functional Theory and Monte Carlo Simulations. *J. Phys. Chem. C* **121**, 3479–3487 (2017).

55. Boes, J. R. & Kitchin, J. R. Neural network predictions of oxygen interactions on a dynamic Pd surface. *Mol. Simul.* **43**, 346–354 (2017).

56. Kang, J. *et al.* First-principles database driven computational neural network approach to the discovery of active ternary nanocatalysts for oxygen reduction reaction. *Phys. Chem. Chem. Phys.* **20**, 24539–24544 (2018).

57. Deaven, D. M. & Ho, K. M. Molecular Geometry Optimization with a Genetic Algorithm. *Phys. Rev. Lett.* **75**, 288–291 (1995).

58. Kolsbjerg, E. L., Peterson, A. A. & Hammer, B. Neural-network-enhanced evolutionary algorithm applied to supported metal nanoparticles. *Phys. Rev. B* **97**, 195424 (2018).

59. Kolb, B., Lentz, L. C. & Kolpak, A. M. Discovering charge density functionals and structure-property relationships with PROPhet: A general framework for coupling machine learning and first-principles methods. *Sci. Rep.* **7**, 1192 (2017).

60. Schütt, K. T. *et al.* SchNetPack: A Deep Learning Toolbox For Atomistic Systems. *J. Chem. Theory Comput.* **15**, 448–455 (2019).

61. Behler, J. Constructing high-dimensional neural network potentials: A tutorial review. *Int. J. Quantum Chem.* **115**, 1032–1050 (2015).

62. Behler, J. & Parrinello, M. Generalized Neural-Network Representation of High-Dimensional Potential-Energy Surfaces. *Phys. Rev. Lett.* **98**, 146401 (2007).

63. Behler, J. Atom-centered symmetry functions for constructing high-dimensional neural network potentials. *J. Chem. Phys.* **134**, 074106 (2011).

64. Gastegger, M., Schwiedrzik, L., Bittermann, M., Berzsenyi, F. & Marquetand, P. wACSF—Weighted atom-centered symmetry functions as descriptors in machine learning potentials. *J. Chem. Phys.* **148**, 241709 (2018).

65. Artrith, N. & Behler, J. High-dimensional neural network potentials for metal surfaces: A prototype study for copper. *Phys. Rev. B* **85**, 045439 (2012).

66. Artrith, N. & Kolpak, A. M. Understanding the Composition and Activity of Electrocatalytic Nanoalloys in Aqueous Solvents: A Combination of DFT and Accurate Neural Network Potentials. *Nano Lett.* **14**, 2670–2676 (2014).

67. Artrith, N. & Kolpak, A. M. Grand canonical molecular dynamics simulations of Cu–Au nanoalloys in thermal equilibrium using reactive ANN potentials. *Comput. Mater. Sci.* **110**, 20–28 (2015).

68. Huang, S.-D., Shang, C., Zhang, X.-J. & Liu, Z.-P. Material discovery by combining stochastic surface walking global optimization with a neural network. *Chem. Sci.* **8**, 6327–6337 (2017).

69. Kitchin, J. R. Machine learning in catalysis. *Nat. Catal.* **1**, 230–232 (2018).

70. Nørskov, J. K., Studt, F., Abild-Pedersen, F. & Bligaard, T. *Fundamental Concepts in Heterogeneous Catalysis*. (John Wiley & Sons, Inc, 2014).

71. Cramer, C. J. *Essentials of Computational Chemistry*. (Wiley, 2004).

72. Stoltze, P. Microkinetic simulation of catalytic reactions. *Prog. Surf. Sci.* **65**, 65–150 (2000).

73. Hoffmann, M. J. & Bligaard, T. A Lattice Kinetic Monte Carlo Solver for First-Principles Microkinetic Trend Studies. *J. Chem. Theory Comput.* **14**, 1583–1593 (2018).

74. Medford, A. J. *et al.* CatMAP: A Software Package for Descriptor-Based Microkinetic Mapping of Catalytic Trends. *Catal. Lett.* **145**, 794–807 (2015).

75. Andersen, M., Plaisance, C. P. & Reuter, K. Assessment of mean-field microkinetic models for CO methanation on stepped metal surfaces using accelerated kinetic Monte Carlo. *J. Chem. Phys.* **147**, 152705 (2017).

76. Lukkien, J. J., Segers, J. P. L., Hilbers, P. A. J., Gelten, R. J. & Jansen, A. P. J. Efficient Monte Carlo methods for the simulation of catalytic surface reactions. *Phys. Rev. E* **58**, 2598–2610 (1998).

77. Andersen, M., Panosetti, C. & Reuter, K. A Practical Guide to Surface Kinetic Monte Carlo Simulations. *Front. Chem.* **7**, 202 (2019).

78. Papanikolaou, K. G. & Stamatakis, M. Toward the accurate modeling of the kinetics of surface reactions using the kinetic Monte Carlo method. in *Frontiers of Nanoscience* vol. 17 95–125 (Elsevier, 2020).

79. Hoffmann, M. J., Matera, S. & Reuter, K. kmos: A lattice kinetic Monte Carlo framework. *Comput. Phys. Commun.* **185**, 2138–2150 (2014).

80. Kresse, G. & Hafner, J. Ab initio molecular-dynamics simulation of the liquid-metal--amorphous-semiconductor transition in germanium. *Phys. Rev. B* **49**, 14251–14269 (1994).

81. Kresse, G. & Furthmüller, J. Efficiency of ab-initio total energy calculations for metals and semiconductors using a plane-wave basis set. *Comput. Mater. Sci.* **6**, 15–50 (1996).

82. Mortensen, J. J. *et al.* Bayesian Error Estimation in Density-Functional Theory. *Phys. Rev. Lett.* **95**, (2005).

83. Wellendorff, J. *et al.* Density functionals for surface science: Exchange-correlation model development with Bayesian error estimation. *Phys. Rev. B* **85**, 235149 (2012).

84. Blöchl, P. E. Projector augmented-wave method. *Phys. Rev. B* **50**, 17953–17979 (1994).

85. Kresse, G. & Joubert, D. From ultrasoft pseudopotentials to the projector augmented-wave method. *Phys. Rev. B* **59**, 1758–1775 (1999).

86. Edelstein, A. S. *et al.* Inversion of surface composition and evolution of nanostructure in Cu/Co nanocrystals. *Appl. Phys. Lett.* **74**, 3161–3163 (1999).

87. Xiang, Y. *et al.* Long-Chain Terminal Alcohols through Catalytic CO Hydrogenation. *J. Am. Chem. Soc.* **135**, 7114–7117 (2013).

88. Kresse, G. & Hafner, J. *Ab initio* molecular-dynamics simulation of the liquid-metal–amorphous-semiconductor transition in germanium. *Phys. Rev. B* **49**, 14251–14269 (1994).

89. Henkelman, G., Uberuaga, B. P. & Jónsson, H. A climbing image nudged elastic band method for finding saddle points and minimum energy paths. *J. Chem. Phys.* **113**, 9901–9904 (2000).

90. Henkelman, G. & Jónsson, H. A dimer method for finding saddle points on high dimensional potential surfaces using only first derivatives. *J. Chem. Phys.* **111**, 7010–7022 (1999).

91. Medford, A. J. *et al.* Assessing the reliability of calculated catalytic ammonia synthesis rates. *Science* **345**, 197–200 (2014).

92. Grabow, L. C. & Mavrikakis, M. Mechanism of Methanol Synthesis on Cu through CO_2 and CO Hydrogenation. *ACS Catal.* **1**, 365–384 (2011).

93. Che, M. Nobel Prize in chemistry 1912 to Sabatier: Organic chemistry or catalysis? *Catal. Today* **218–219**, 162–171 (2013).

94. Medford, A. J. *et al.* From the Sabatier principle to a predictive theory of transition-metal heterogeneous catalysis. *J. Catal.* **328**, 36–42 (2015).

95. Liu, S. *et al.* Moderate Surface Segregation Promotes Selective Ethanol Production in CO_2 Hydrogenation Reaction over CoCu Catalysts. *Angew. Chem. Int. Ed.* **61**, (2022).

96. Wang, S. *et al.* Universal transition state scaling relations for (de)hydrogenation over transition metals. *Phys. Chem. Chem. Phys.* **13**, 20760 (2011).

97. Wang, S. *et al.* Universal Brønsted-Evans-Polanyi Relations for C–C, C–O, C–N, N–O, N–N, and O–O Dissociation Reactions. *Catal. Lett.* **141**, 370–373 (2011).

98. Dybeck, E. C., Plaisance, C. P. & Neurock, M. Generalized Temporal Acceleration Scheme for Kinetic Monte Carlo Simulations of Surface Catalytic Processes by Scaling the Rates of Fast Reactions. *J. Chem. Theory Comput.* **13**, 1525–1538 (2017).

99. Eren, B. *et al.* Structure of Copper–Cobalt Surface Alloys in Equilibrium with Carbon Monoxide Gas. *J. Am. Chem. Soc.* **140**, 6575–6581 (2018).

100. Zhao, Z.-J. *et al.* Theory-guided design of catalytic materials using scaling relationships and reactivity descriptors. *Nat. Rev. Mater.* **4**, 792–804 (2019).

Appendix

A1. Modeling CoCu Nanoparticles Using Neural Network Accelerated Monte Carlo Simulations

Table A1.1 List of radial symmetry functions.

No	η (Å^{-2})	μ (Å)
1	12.5	5.5
2	12.5	5.3
3	12.5	5.1
4	12.5	4.9
5	12.5	4.7
6	12.5	4.5
7	12.5	4.3
8	12.5	4.1
9	12.5	3.9
10	12.5	3.7
11	12.5	3.5
12	12.5	3.3
13	12.5	3.1
14	12.5	2.9
15	12.5	2.7
16	12.5	2.5
17	12.5	2.3
18	12.5	2.1
19	12.5	1.9
20	12.5	1.7
21	12.5	1.5
22	12.5	1.3
23	12.5	1.1
24	12.5	0.9
25	12.5	0.7
26	12.5	0.5

Table A1.2 List of angular symmetry functions.

No	η (Å^{-2})	λ	ζ
27	0.05390956	-1.0	1.0
28	0.05390956	1.0	1.0
29	0.07193817	-1.0	1.0
30	0.07193817	1.0	1.0
31	0.10079134	-1.0	1.0
32	0.10079134	1.0	1.0
33	0.15125	-1.0	1.0
34	0.15125	1.0	1.0
35	0.25182102	-1.0	1.0
36	0.25182102	1.0	1.0
37	0.5	-1.0	1.0
38	0.5	1.0	1.0

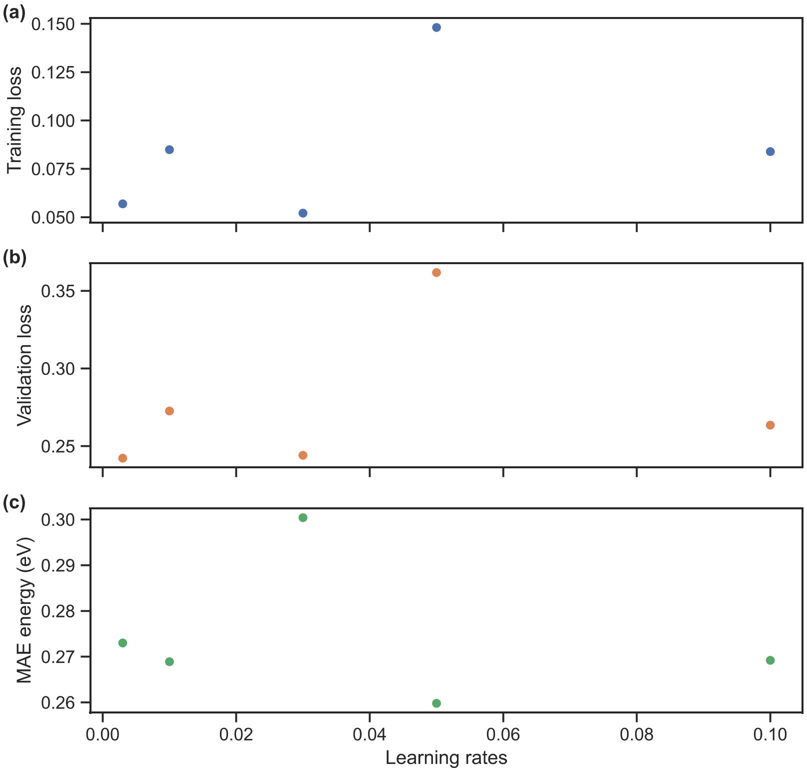

Figure A1.1 Test of learning rates.

A too-small learning rate may result in a long training process that could get stuck, while a too-large learning rate may make the learning jump over the minimum. As shown in Figure A1.1, we set the architecture to 3 hidden layers and 5 nodes, and the learning rate is changed by 0.003, 0.01, 0.03, 0.05, and 0.1. After around 400 epochs, the model got well trained, and all the results were collected. With all varied learning rates, the training loss, validation loss, and the mean absolute errors (MAE) are almost the same, which means the values of the learning rate we have chosen may not affect the trained model notably. The learning rate of 0.03 will be used for all the calculations.

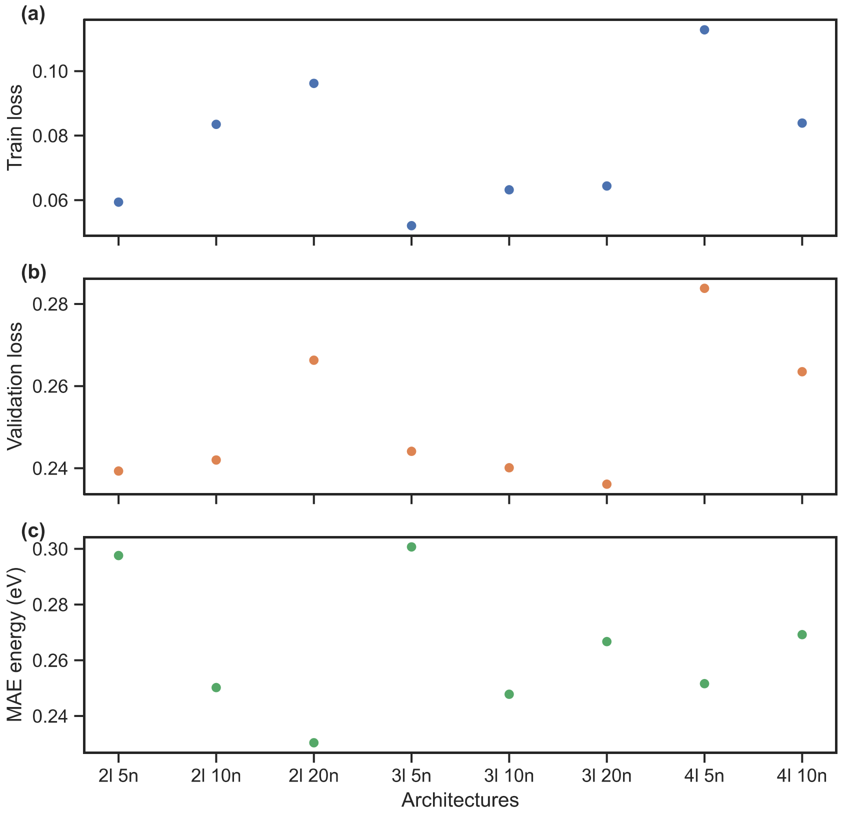

Figure A1.2 Test of the architectures of neural networks.

A series of architectures of neural networks were accessed, changing from 2 hidden layers and 5 nodes to 4 hidden layers and 10 nodes. The architecture is desired to keep small to decrease the possibility of overfitting, while too small a neural network may not enough to properly fit the data. In Figure A1.2, the training loss, validation loss, and MAEs are almost the same, indicating they are all large enough to describe our system. In the following calculations, we will use 3 hidden layers and 10 nodes as the default option. We note that the range of applicability of a given neural network model highly depends on the input data set and should be validated carefully.

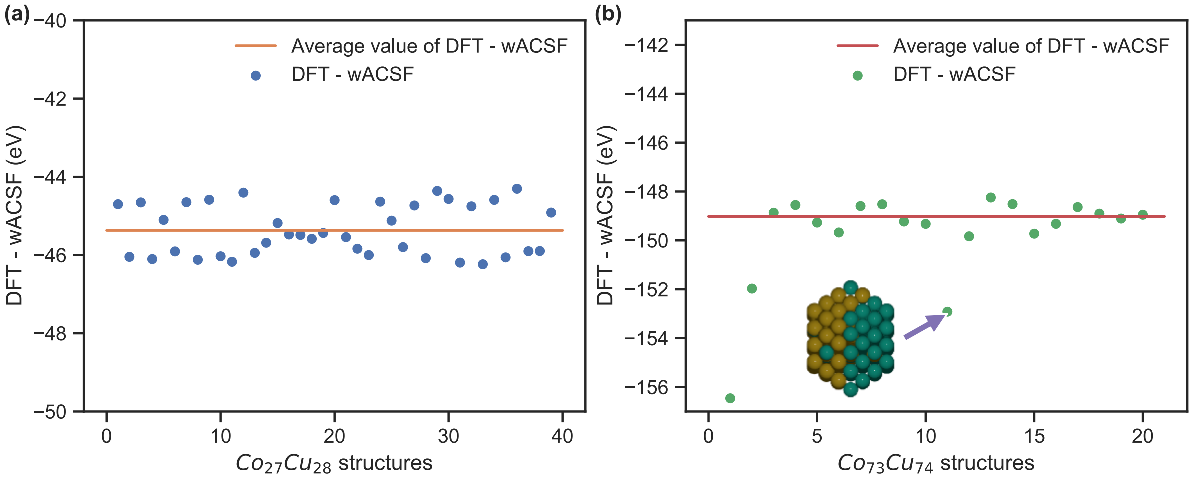

Figure A1.3 (a) The energy difference between DFT and wACSF method when applying the model from $Co_{13}Cu_{42}$ to (a) $Co_{27}Cu_{28}$ and (b) $Co_{73}Cu_{74}$.

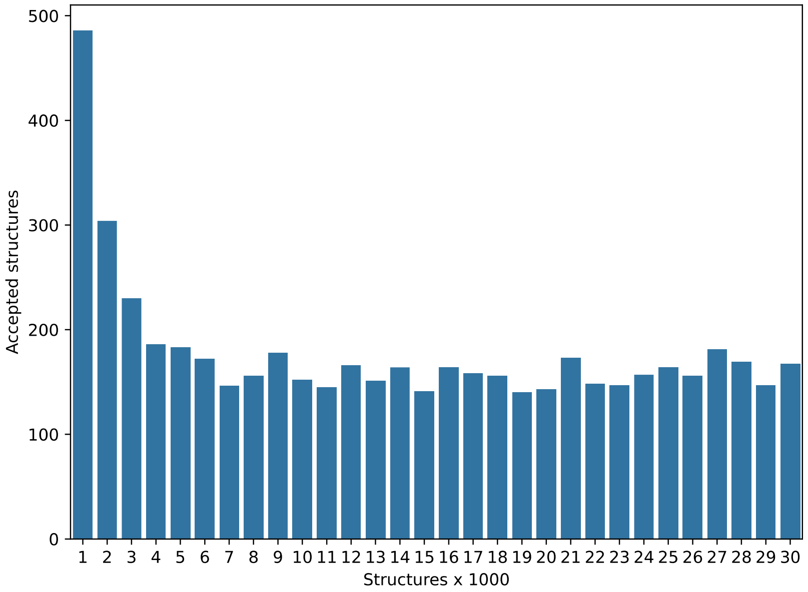

Figure A1.4 The number of accepted structures in every 1000 MC steps in Figure 3.4a.

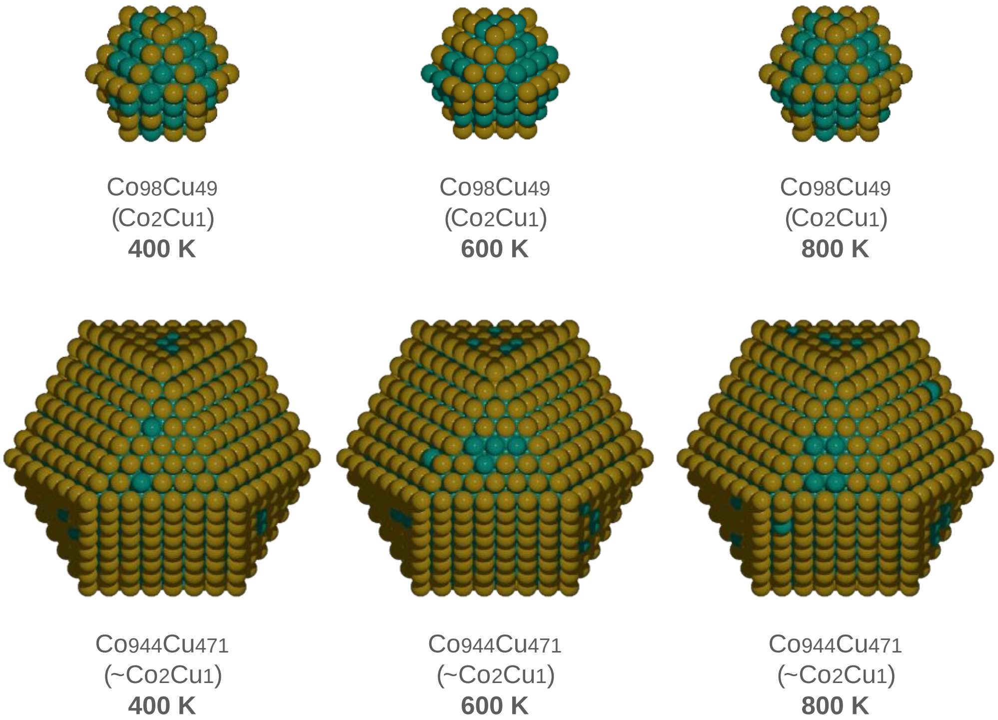

Figure A1.5 Co_2Cu_1 particles with 147 and 1415 atoms under different temperatures.

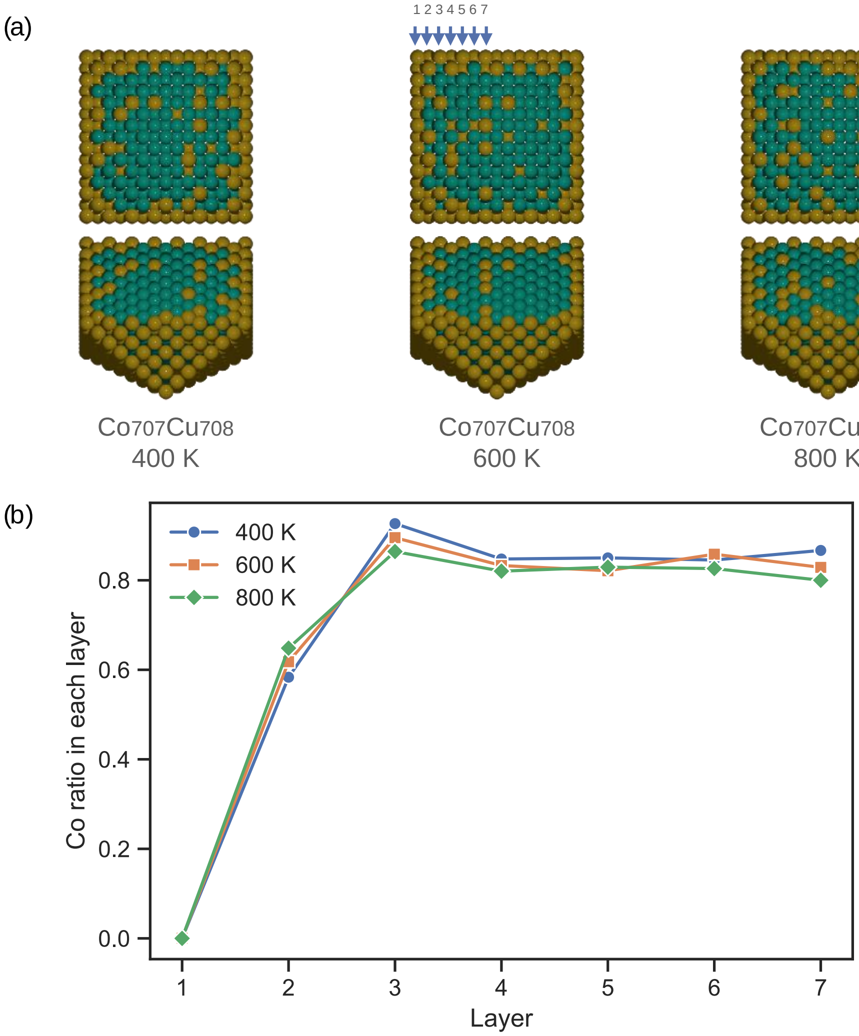

Figure A1.6 Segregation behaviors with different temperatures according to wACSF-MC. (a) optimized configurations and (b) average Co ratios for 10 converged structures in each layer.

We investigated the effect of temperature on the distribution of Co and Cu atoms in the particles. The optimized structures of $Co_{707}Cu_{708}$ at 400 K, 600 K, and 800 K have been illustrated in Figure Figure A1.6. The chemical ordering of the particles didn't show significant differences with the temperatures. To be clearer, we counted the Co ratio on each layer of $Co_{707}Cu_{708}$ under the three temperatures. The distribution of Co confirmed raising the temperature from 400 to 800 K may not change the chemical ordering of CoCu particles. As a comparison, Dzhurakhalov et al.[28] utilized Monte Carlo simulation with a modified embedded atom method to explore the phase separation behavior of CoCu particles, and onion-like CoCu configurations were discovered at 100 K. However, the CoCu configurations get more random when the temperature is raised to 500 K.

A2. Insights into the Mechanism of CO Hydrogenation on Segregated CoCu Catalysts

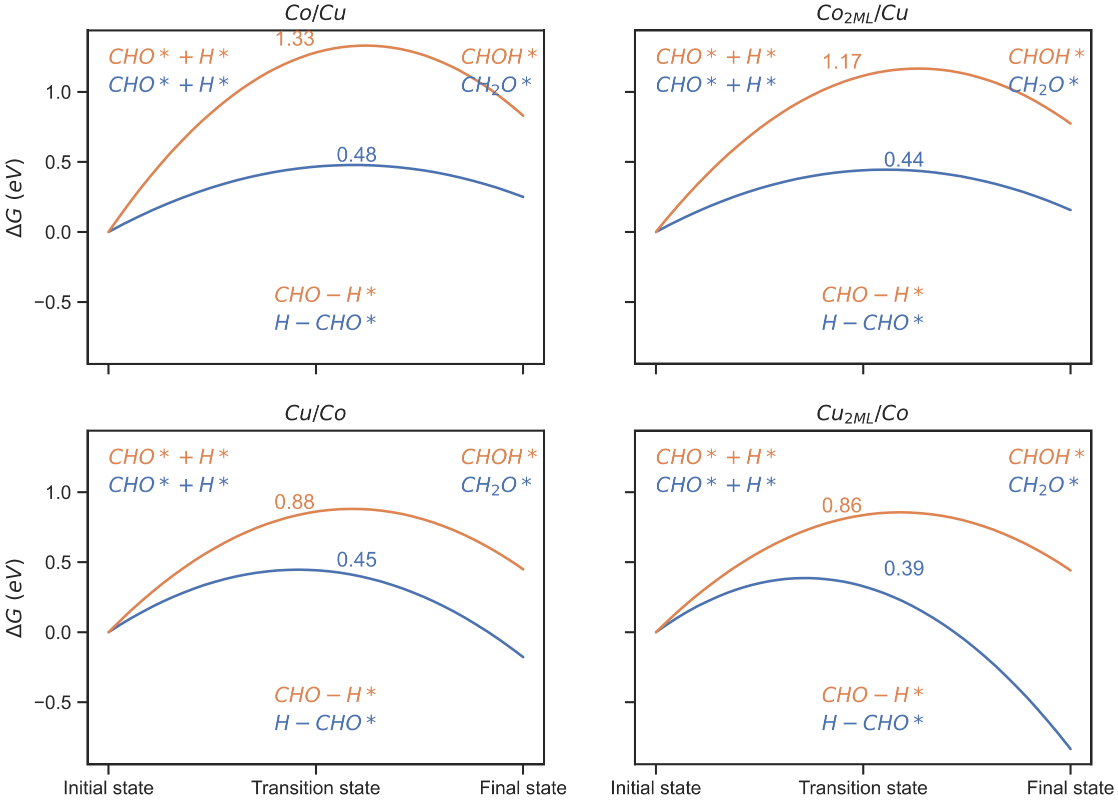

Figure A2.1 The competition between the formation of CHOH* and CH_2O* from CHO*.

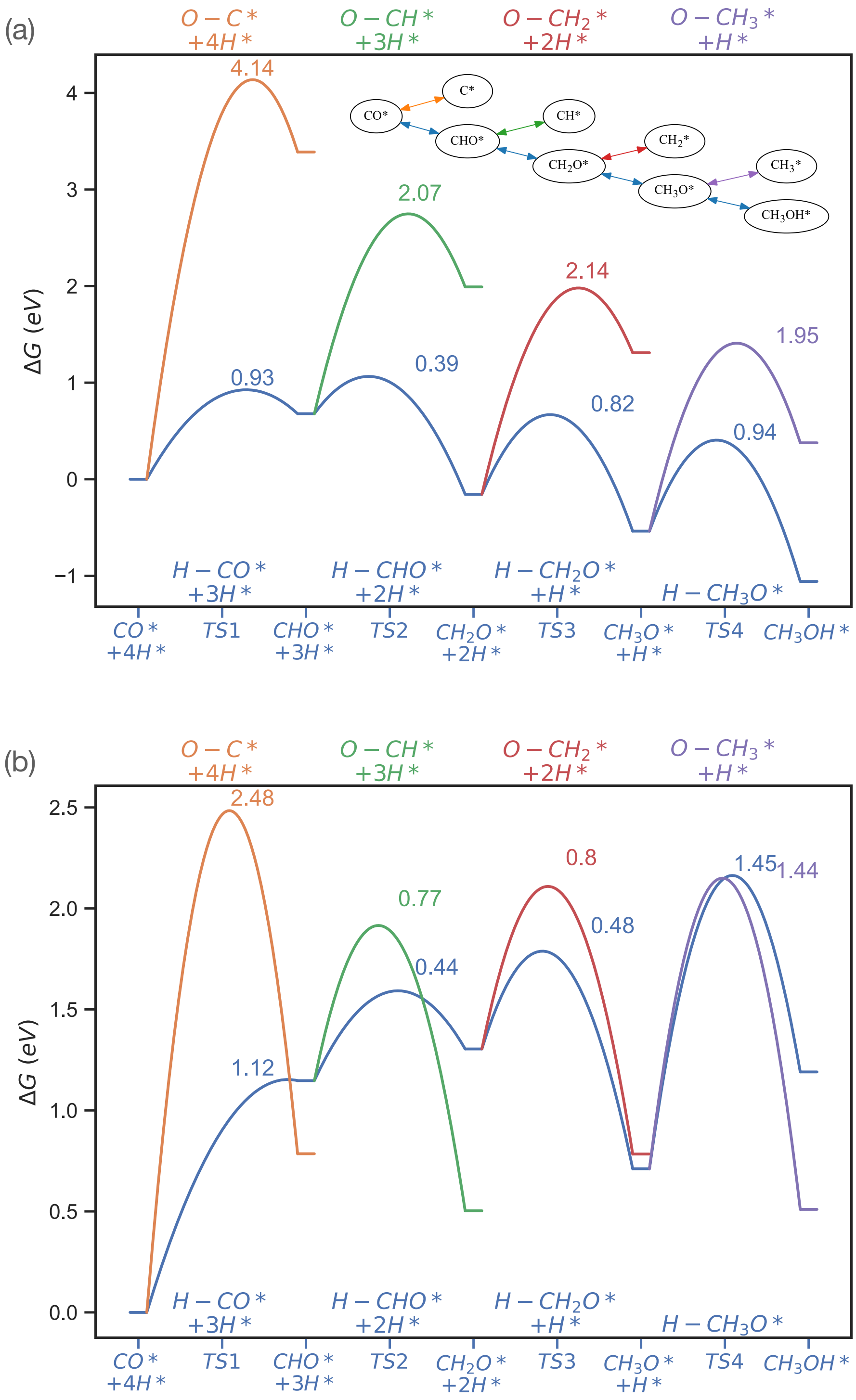

Figure A2.2 The competition between CHxO* hydrogenation and dissociation on (a) Cu_{2ML}/Co(111) and (b) Co_{2ML}/Cu(111).

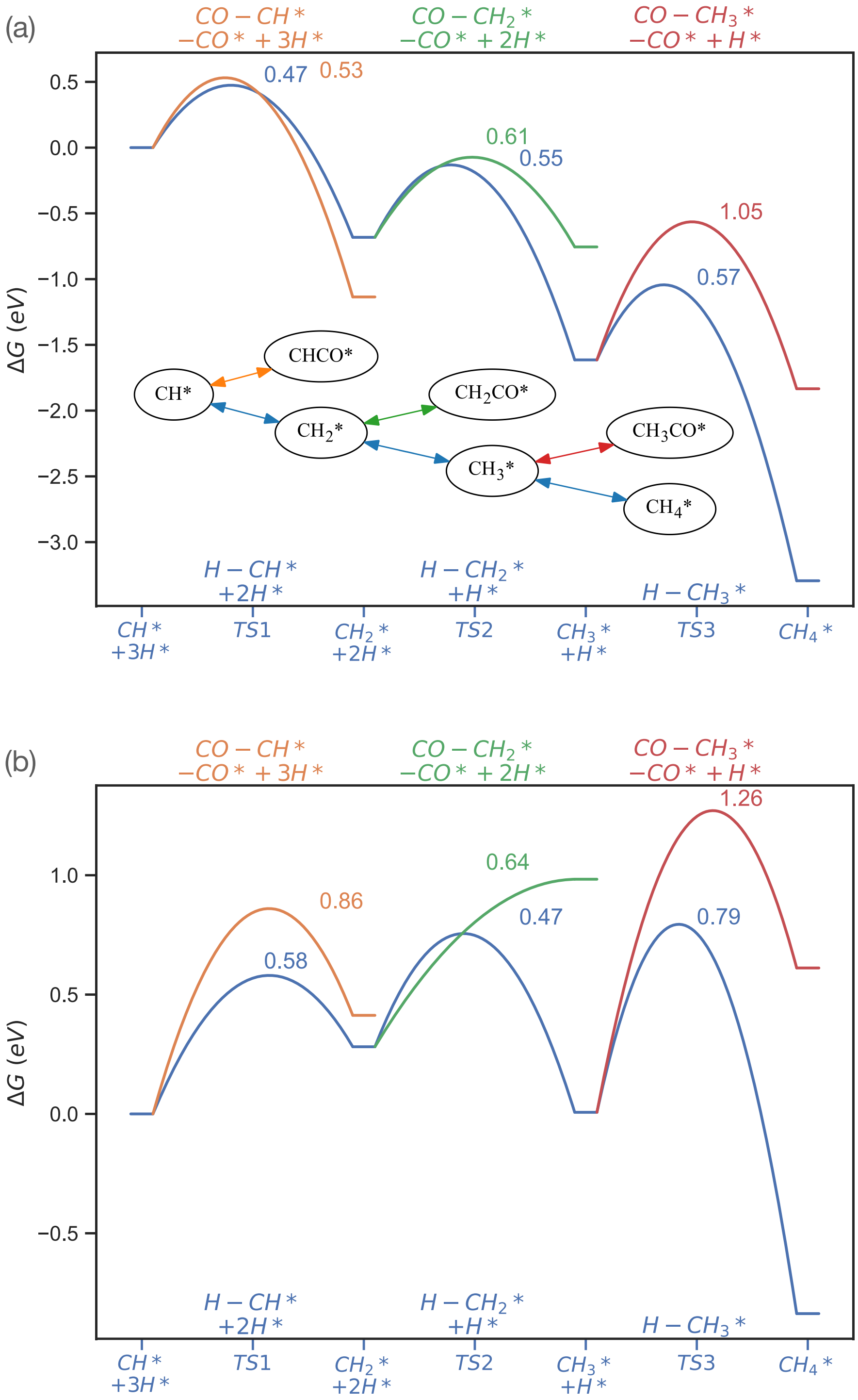

Figure A2.3 The competition between CHx* hydrogenation and CO* insertion on (a) Cu_{2ML}/Co(111) and (b) Co_{2ML}/Cu(111).

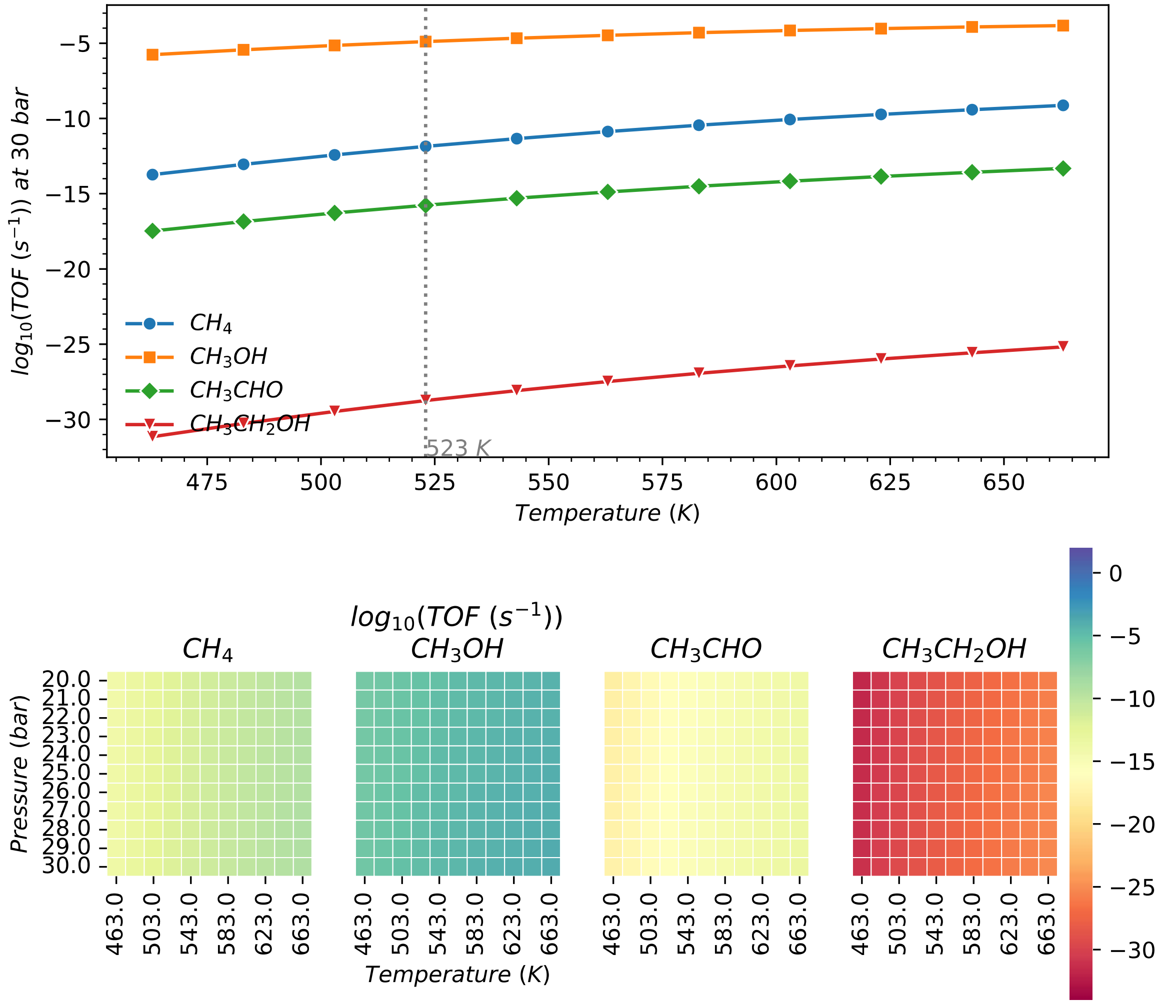

Figure A2.4 Turnover frequencies of CH_4, CH_3OH, CH_3CHO, and CH_3CH_2OH on Cu_{2ML}/Co(111) under different reaction conditions.

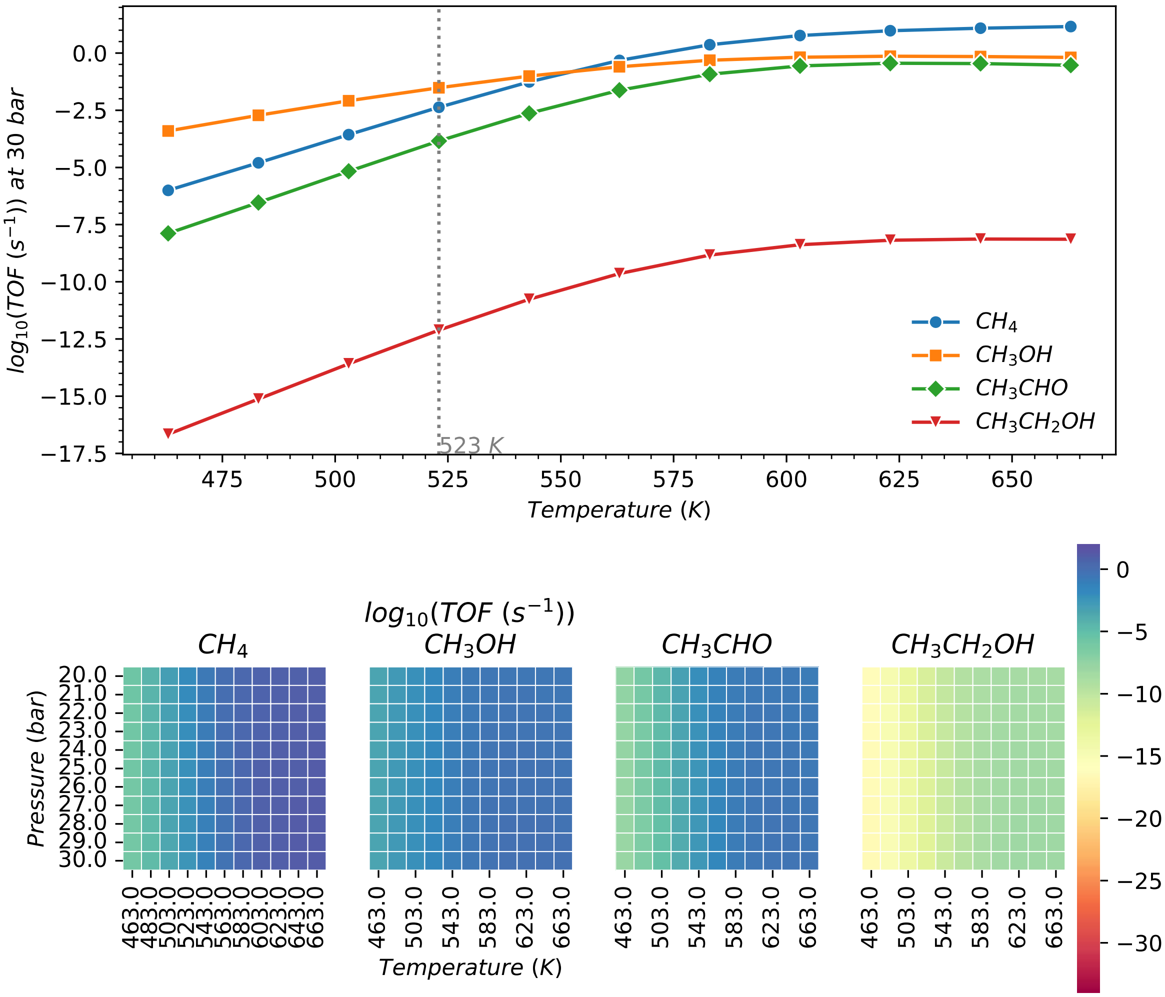

Figure A2.4 Turnover frequencies of CH_4, CH_3OH, CH_3CHO, and CH_3CH_2OH on Co_{2ML}/Cu(111) under different reaction conditions.

Table A2.1 Energy profile of Cu/Co(111).

Site	Species	Energies	Formation energy	Frequencies
gas	CO	-12.09	2.52	[14.0, 48.8, 2127.1]
gas	H2	-7.15	0.00	[75.2, 103.7, 4431.0]
gas	CH4	-23.26	0.00	[4.3, 1321.3, 1321.7, 1323.5, 1538.3, 1540.7, 3040.1, 3106.2, 3107.6, 3120.1]
gas	H2O	-12.81	0.00	[3873.6, 3758.0, 1623.8, 138.2, 105.4, 31.9]
gas	CH3OH	-27.75	1.18	[14.6, 30.6, 60.4, 292.1, 1004.5, 1062.3, 1150.3, 1351.1, 1455.5, 1476.5, 1487.8, 2947.3, 2999.7, 3075.9, 3775.6]
gas	CH3CHO	-35.42	2.47	[30.9, 59.2, 70.2, 163.2, 502.3, 756.6, 872.5, 1103.1, 1109.5, 1354.5, 1398.9, 1442.5, 1449.3, 1757.3, 2815.2, 2981.5, 3036.3, 3102.2]
gas	CH3CH2OH	-43.33	1.70	[0.5, 10.6, 99.6, 239.6, 288.5, 415.2, 807.9, 875.1, 1008.2, 1070.1, 1153.8, 1245.1, 1269.1, 1382.0, 1419.4, 1465.1, 1479.6, 1501.6, 2929.4, 2958.0, 2991.9, 3065.2, 3068.1, 3765.1]
111	H	-197.74	-0.04	[748.4, 751.2, 1089.1]
111	H2O	-207.06	-0.13	[12.0, 12.0, 12.0, 21.2, 39.9, 65.9, 1604.1, 3720.6, 3841.1]
111	O	-198.80	0.98	[316.8, 318.4, 463.1]
111	OH	-203.18	0.17	[169.4, 178.1, 336.0, 398.6, 401.2, 3735.1]
111	C	-198.94	4.14	[430.3, 432.9, 517.5]
111	CO	-206.85	1.89	[106.5, 108.6, 219.4, 220.1, 275.8, 1824.9]
111	COH	-209.25	3.07	[94.2, 131.8, 147.6, 325.4, 351.3, 391.6, 1100.2, 1252.4, 3605.2]
111	CHO	-209.68	2.64	[19.0, 119.7, 122.9, 185.5, 401.4, 586.6, 1248.9, 1421.7, 2845.8]
111	CH	-203.96	2.70	[338.1, 352.7, 559.8, 602.5, 605.1, 3062.3]
111	CH2O	-213.65	2.25	[53.0, 86.3, 124.6, 148.0, 285.4, 518.8, 828.4, 1166.7, 1224.0, 1491.2, 2967.9, 3065.7]
111	CHCO	-217.60	3.67	[52.7, 71.8, 119.4, 202.1, 316.2, 514.3, 528.8, 554.4, 1027.3, 1165.8, 2082.2, 3063.7]
111	CHCHO	-221.45	3.40	[62.1, 76.1, 208.4, 245.0, 250.5, 379.2, 666.7, 745.4, 919.8, 1071.9, 1220.7, 1317.3, 1406.7, 2957.3, 3019.2]
111	CHOH	-213.07	2.82	[63.9, 88.9, 206.4, 213.2, 326.4, 416.2, 712.9, 1035.7, 1196.9, 1378.0, 2953.0, 3648.1]
111	CH2	-208.17	2.07	[119.3, 194.0, 290.7, 429.7, 469.2, 664.7, 1348.8, 2918.3, 3020.8]
111	CH3O	-218.27	1.20	[12.0, 66.7, 78.3, 229.2, 232.2, 265.8, 987.1, 1136.4, 1140.5, 1438.0, 1466.5, 1467.1, 2950.0, 3025.1, 3027.4]
111	CH2CO	-221.08	3.78	[87.7, 127.8, 137.9, 170.1, 254.3, 382.7, 517.1, 684.9, 797.8, 977.2, 1058.8, 1383.8, 1436.9, 3040.0, 3149.5]
111	CH2CHO	-225.59	2.84	[77.0, 87.6, 112.6, 175.9, 214.5, 318.9, 517.3, 736.5, 820.5, 928.9, 969.4, 1186.9, 1270.1, 1397.8, 1480.9, 2990.7, 3050.0, 3162.9]
111	CH3	-212.76	1.05	[106.4, 109.4, 222.4, 281.1, 561.8, 568.7, 1168.8, 1400.3, 1401.2, 2934.5, 3007.8, 3012.3]
111	CH3OH	-222.05	0.99	[12.0, 12.0, 27.5, 60.9, 73.6, 86.3, 283.5, 1005.6, 1059.2, 1148.9, 1347.1, 1450.4, 1468.9, 1481.6, 2927.9, 2976.7, 3075.7, 3668.9]
111	CH3CO	-225.67	2.76	[61.2, 79.6, 95.0, 117.7, 206.5, 234.4, 345.3, 554.7, 899.2, 951.0, 1068.9, 1336.5, 1422.0, 1433.4, 1534.7, 2971.2, 3048.2, 3072.3]
111	CH4	-217.48	-0.10	[12.0, 12.0, 12.0, 23.2, 47.6, 100.9, 1313.9, 1318.6, 1319.9, 1531.0, 1534.1, 2975.3, 3082.6, 3092.1, 3094.0]
111	CH3CHO	-229.77	2.24	[12.0, 12.0, 12.0, 46.1, 58.7, 78.9, 149.3, 501.7, 752.8, 876.1, 1098.3, 1111.3, 1351.3, 1392.8, 1434.1, 1443.0, 1727.5, 2822.4, 2969.6, 3028.4, 3095.5]
111	CH3CH2O	-234.01	1.57	[12.0, 51.9, 59.6, 156.1, 221.9, 249.5, 297.4, 466.5, 799.1, 862.3, 1007.9,

				1082.3, 1139.8, 1271.0, 1355.2, 1384.0, 1461.5, 1466.7, 1483.8, 2948.6, 2972.9, 2986.6, 3049.4, 3050.6]
111	CH3CH2OH	-237.77	1.39	[32.0, 44.3, 46.8, 83.1, 93.2, 118.7, 248.2, 376.0, 417.8, 801.2, 851.1, 1004.8, 1052.5, 1144.8, 1243.0, 1274.8, 1381.9, 1411.0, 1460.8, 1472.7, 1491.3, 2957.9, 2984.0, 3001.6, 3055.7, 3066.3, 3684.1]
111	H-CO	-209.40	2.92	[22.7, 106.4, 179.1, 232.3, 407.6, 554.9, 1366.8, 1743.6]
111	CO-H	-208.09	4.22	[106.8, 152.7, 227.6, 290.4, 332.2, 460.8, 1017.6, 1460.1]
111	O-C	-202.77	5.97	[249.4, 293.9, 396.6, 432.3, 475.6]
111	O-CH	-207.79	4.53	[185.1, 291.3, 377.8, 414.1, 516.4, 596.0, 840.4, 3104.7]
111	H-CHO	-212.86	3.03	[50.5, 74.0, 140.1, 182.3, 355.2, 661.2, 813.4, 1132.4, 1181.2, 1688.2, 2870.1]
111	CHO-H	-212.47	3.43	[70.2, 90.0, 154.3, 305.6, 446.6, 585.1, 814.1, 999.1, 1278.7, 1441.8, 2887.2]
111	CO-CH	-215.98	5.30	[15.1, 107.7, 221.8, 290.9, 337.7, 339.9, 546.7, 622.5, 794.5, 1841.6, 3048.2]
111	CHO-CH	-162.87	61.99	[113.8, 186.4, 284.8, 338.9, 369.8, 514.1, 533.7, 570.6, 786.7, 914.0, 1245.9, 1346.6, 2913.3, 2999.7]
111	H-CH	-207.01	3.23	[268.3, 367.6, 524.3, 545.0, 609.1, 813.0, 1377.9, 3072.9]
111	O-CH2	-212.23	3.67	[138.1, 192.4, 288.0, 413.9, 421.7, 503.4, 651.4, 865.3, 1356.7, 2997.1, 3075.4]
111	H-CH2O	-217.00	2.47	[47.5, 87.3, 165.0, 208.6, 303.9, 439.5, 786.7, 1047.6, 1180.9, 1232.7, 1313.2, 1506.4, 2948.5, 3031.3]
111	H-CHCO	-220.16	4.69	[20.7, 35.0, 93.2, 122.1, 239.0, 421.7, 525.8, 552.8, 712.2, 985.8, 1112.6, 1193.4, 2077.1, 3108.1]
111	CO-CH2	-220.24	4.62	[12.0, 98.8, 148.9, 236.6, 255.8, 324.7, 440.3, 450.0, 629.5, 813.8, 1325.0, 1891.0, 2964.2, 3033.9]
111	CHO-CH2	-166.92	61.51	[87.1, 168.4, 243.9, 282.6, 348.0, 411.1, 469.1, 538.3, 720.3, 778.0, 881.3, 1243.7, 1269.3, 1338.6, 2761.4, 2927.3, 2972.3]
111	H-CH2	-211.21	2.60	[120.9, 220.2, 395.8, 439.7, 489.9, 613.9, 819.1, 1359.5, 1386.4, 2969.6, 3033.7]
111	O-CH3	-216.36	3.11	[79.6, 136.0, 187.6, 268.1, 286.5, 396.8, 669.8, 760.1, 1062.4, 1403.9, 1409.2, 3004.6, 3159.8, 3225.6]
111	H-CH3O	-220.76	2.29	[44.1, 46.2, 69.3, 132.9, 161.1, 307.3, 758.9, 948.7, 989.5, 1124.7, 1129.1, 1426.6, 1458.1, 1460.3, 2919.9, 2982.8, 3010.8]
111	H-CH2CO	-224.01	4.42	[101.1, 131.3, 147.9, 216.4, 249.7, 329.8, 396.1, 533.3, 805.4, 927.5, 983.7, 1067.0, 1276.3, 1344.9, 1421.0, 3028.6, 3154.7]
111	CO-CH3	-224.39	4.04	[67.7, 70.9, 90.9, 192.2, 236.6, 253.0, 259.0, 417.2, 757.7, 785.4, 1147.5, 1413.7, 1426.3, 1715.1, 2983.5, 3087.0, 3143.7]
111	CHO-CH3	-227.74	4.26	[84.2, 106.8, 121.1, 148.7, 259.1, 309.0, 346.6, 447.7, 621.0, 762.8, 914.3, 1147.0, 1222.5, 1308.6, 1411.8, 1434.5, 2941.3, 2970.9, 3066.2, 3123.3]
111	H-CH3	-215.63	1.76	[12.0, 79.8, 151.1, 309.1, 476.6, 659.7, 771.7, 1095.6, 1322.3, 1428.2, 1440.7, 3008.8, 3122.5, 3134.4]
111	H-CH3CO	-228.69	3.32	[19.2, 34.8, 76.4, 109.6, 164.2, 188.3, 435.0, 513.1, 706.7, 924.2, 949.5, 1042.7, 1193.7, 1346.1, 1430.5, 1440.9, 1592.8, 2972.2, 3046.7, 3091.6]
111	H-CH3CHO	-232.76	2.82	[45.8, 65.5, 98.3, 121.2, 196.5, 210.4, 366.0, 487.4, 571.8, 885.8, 937.2, 1039.9, 1105.2, 1264.5, 1321.3, 1369.4, 1403.6, 1451.5, 1459.1, 2946.5, 2967.0, 3040.8, 3079.8]
111	H-CH3CH2O	-236.44	2.72	[12.0, 36.0, 60.7, 95.7, 150.3, 218.1, 277.8, 417.7, 530.6, 791.5, 844.5, 991.8, 1022.7, 1080.3, 1138.9, 1272.0, 1352.9, 1381.4, 1461.8, 1464.5, 1480.8, 2954.1, 2977.2, 2992.0, 3051.0, 3059.5]
111	O-H	-201.39	1.97	[178.6, 285.7, 431.3, 449.2, 942.6]
111	OH-H	-205.70	1.24	[45.4, 104.3, 269.0, 395.0, 497.5, 760.6, 965.7, 3655.7]

Table A2.2 Energy profile of Cu$_{2ML}$/Co(111).

Site	Species	Energies	Formation energy	Frequencies
gas	CO	-12.09	2.52	[14.0, 48.8, 2127.1]
gas	H2	-7.15	0.00	[75.2, 103.7, 4431.0]
gas	CH4	-23.26	0.00	[4.3, 1321.3, 1321.7, 1323.5, 1538.3, 1540.7, 3040.1, 3106.2, 3107.6, 3120.1]
gas	H2O	-12.81	0.00	[3873.6, 3758.0, 1623.8, 138.2, 105.4, 31.9]
gas	CH3OH	-27.75	1.18	[14.6, 30.6, 60.4, 292.1, 1004.5, 1062.3, 1150.3, 1351.1, 1455.5, 1476.5, 1487.8, 2947.3, 2999.7, 3075.9, 3775.6]
gas	CH3CHO	-35.42	2.47	[30.9, 59.2, 70.2, 163.2, 502.3, 756.6, 872.5, 1103.1, 1109.5, 1354.5, 1398.9, 1442.5, 1449.3, 1757.3, 2815.2, 2981.5, 3036.3, 3102.2]
gas	CH3CH2OH	-43.33	1.70	[0.5, 10.6, 99.6, 239.6, 288.5, 415.2, 807.9, 875.1, 1008.2, 1070.1, 1153.8, 1245.1, 1269.1, 1382.0, 1419.4, 1465.1, 1479.6, 1501.6, 2929.4, 2958.0, 2991.9, 3065.2, 3068.1, 3765.1]
111	H	-140.13	0.02	[769.9, 770.7, 1083.9]
111	H2O	-149.50	-0.12	[12.0, 12.0, 12.0, 12.0, 22.2, 51.6, 1608.0, 3720.6, 3838.6]
111	O	-141.21	1.02	[331.9, 335.3, 441.6]
111	OH	-145.57	0.24	[171.2, 188.2, 351.3, 392.1, 394.7, 3735.8]
111	C	-141.23	4.30	[450.1, 453.1, 504.3]
111	CO	-149.15	2.04	[97.3, 105.7, 217.8, 224.6, 253.7, 1828.4]
111	COH	-151.52	3.25	[85.8, 128.4, 135.9, 328.5, 348.6, 399.7, 1106.0, 1247.1, 3603.8]
111	CHO	-152.00	2.76	[12.0, 78.2, 110.5, 173.2, 390.8, 603.4, 1248.2, 1480.8, 2811.7]
111	CH	-146.26	2.84	[360.6, 365.0, 549.7, 609.3, 610.4, 3065.9]
111	CH2O	-156.29	2.05	[12.0, 12.7, 48.2, 59.7, 97.8, 110.1, 1147.1, 1229.6, 1501.5, 1746.1, 2835.4, 2889.9]
111	CHCO	-159.96	3.76	[19.8, 44.4, 90.9, 208.9, 308.0, 517.5, 539.5, 554.5, 1026.2, 1164.3, 2085.2, 3084.0]
111	CHCHO	-163.77	3.53	[67.6, 77.6, 206.9, 256.1, 267.8, 376.0, 668.3, 741.9, 919.2, 1075.7, 1220.3, 1316.3, 1405.2, 2951.5, 3029.3]
111	CHOH	-155.40	2.94	[60.7, 100.2, 211.8, 233.8, 343.6, 416.4, 725.7, 1041.4, 1202.3, 1383.5, 2968.7, 3652.1]
111	CH2	-150.50	2.18	[117.5, 201.1, 291.7, 435.1, 464.3, 666.5, 1350.5, 2932.3, 3018.1]
111	CH3O	-160.65	1.26	[12.0, 80.1, 88.5, 228.9, 234.9, 265.0, 986.2, 1139.9, 1143.2, 1441.0, 1465.9, 1467.2, 2949.2, 3023.8, 3026.6]
111	CH2CO	-163.36	3.94	[96.4, 124.9, 128.5, 158.3, 242.9, 370.4, 517.3, 689.5, 796.5, 980.7, 1063.6, 1383.3, 1441.7, 3039.2, 3159.3]
111	CH2CHO	-167.89	2.98	[60.6, 71.4, 96.2, 147.3, 191.8, 305.8, 512.7, 731.0, 813.2, 934.6, 968.6, 1191.2, 1271.6, 1399.4, 1486.5, 2979.5, 3069.7, 3175.2]
111	CH3	-155.11	1.15	[83.9, 98.2, 225.7, 285.7, 579.6, 582.8, 1172.4, 1405.6, 1406.8, 2937.2, 3014.3, 3015.1]
111	CH3OH	-164.50	1.00	[12.0, 12.0, 12.0, 31.5, 69.3, 76.6, 278.0, 1004.1, 1055.8, 1148.6, 1343.0, 1450.0, 1468.2, 1480.8, 2921.1, 2973.2, 3071.0, 3684.8]
111	CH3CO	-167.98	2.89	[12.0, 71.5, 77.2, 109.7, 189.6, 222.1, 341.3, 545.9, 894.1, 949.1, 1062.9, 1333.2, 1421.0, 1433.6, 1554.2, 2966.6, 3045.5, 3073.3]
111	CH4	-159.93	-0.10	[12.0, 12.0, 12.0, 12.0, 60.6, 79.1, 1317.1, 1319.3, 1320.4, 1533.5, 1534.2, 2980.2, 3083.0, 3093.7, 3098.9]
111	CH3CHO	-172.18	2.27	[12.0, 12.0, 17.9, 44.2, 74.5, 143.7, 181.0, 575.1, 766.9, 892.2, 1076.2, 1135.0, 1328.1, 1376.8, 1439.4, 1467.4, 1743.1, 2880.5, 2972.6, 3034.4, 3112.0]
111	CH3CH2O	-176.36	1.67	[53.3, 77.1, 96.0, 168.0, 223.0, 249.8, 298.6, 463.0, 798.7, 862.4, 1006.5,

				1082.7, 1140.2, 1272.1, 1355.6, 1384.2, 1462.6, 1466.6, 1484.0, 2948.4, 2975.1, 2986.9, 3050.3, 3052.2]
111	CH3CH2OH	-180.14	1.47	[12.0, 27.2, 49.5, 51.7, 56.9, 91.8, 237.7, 281.5, 410.3, 807.9, 869.7, 1010.1, 1059.3, 1149.2, 1246.6, 1272.9, 1381.9, 1417.0, 1463.3, 1479.5, 1499.2, 2942.4, 2977.7, 2984.3, 3054.8, 3056.9, 3738.4]
111	H-CO	-151.69	3.07	[34.1, 120.3, 171.1, 229.9, 375.0, 509.7, 1356.5, 1753.6]
111	CO-H	-150.43	4.34	[114.3, 169.1, 240.5, 319.9, 335.9, 472.3, 1029.7, 1456.5]
111	O-C	-145.08	6.11	[259.5, 305.6, 395.8, 436.9, 460.9]
111	O-CH	-150.14	4.63	[208.9, 307.6, 382.0, 407.4, 510.2, 602.4, 839.8, 3105.1]
111	H-CHO	-155.19	3.15	[28.4, 62.8, 145.4, 170.7, 347.2, 656.4, 804.2, 1141.0, 1172.8, 1697.7, 2873.8]
111	CHO-H	-154.80	3.54	[75.5, 101.0, 151.3, 292.9, 429.4, 570.6, 815.9, 989.2, 1274.8, 1462.5, 2880.7]
111	CO-CH	-158.26	5.46	[12.0, 110.3, 238.4, 281.6, 355.5, 358.8, 549.4, 621.5, 807.7, 1853.3, 3043.9]
111	CHO-CH	-161.75	5.55	[23.7, 116.0, 225.3, 326.8, 380.6, 441.6, 498.6, 589.9, 690.0, 858.9, 1179.8, 1702.2, 2851.8, 3050.6]
111	H-CH	-149.31	3.37	[272.3, 390.9, 535.8, 577.4, 616.9, 812.8, 1350.9, 3074.2]
111	O-CH2	-154.55	3.80	[130.1, 213.3, 294.8, 405.0, 418.9, 532.4, 651.7, 867.4, 1369.2, 2999.8, 3071.6]
111	H-CH2O	-159.33	2.58	[49.6, 80.1, 158.3, 186.8, 297.5, 427.5, 795.5, 1036.2, 1181.4, 1209.9, 1318.9, 1507.7, 2938.1, 3022.3]
111	H-CHCO	-162.50	4.80	[25.9, 55.6, 96.7, 103.4, 268.4, 448.8, 544.1, 552.8, 717.9, 954.2, 1064.5, 1166.3, 2072.8, 3133.1]
111	CO-CH2	-162.53	4.77	[32.6, 97.6, 157.8, 239.0, 252.5, 324.2, 443.3, 451.5, 618.3, 802.2, 1324.9, 1902.2, 2966.0, 3032.8]
111	CHO-CH2	-165.91	4.96	[43.7, 120.7, 153.8, 224.8, 279.4, 421.4, 441.3, 456.5, 565.0, 695.4, 800.2, 1209.9, 1348.2, 1490.7, 2871.4, 2965.0, 3020.8]
111	H-CH2	-153.51	2.75	[99.1, 231.2, 408.1, 444.2, 510.1, 601.8, 817.3, 1360.0, 1379.9, 2979.2, 3040.8]
111	O-CH3	-158.76	3.16	[74.8, 125.3, 200.2, 267.7, 282.3, 396.3, 686.7, 771.6, 1075.0, 1403.2, 1412.0, 3009.8, 3157.9, 3226.8]
111	H-CH3O	-163.15	2.35	[13.7, 46.1, 92.7, 124.4, 162.5, 287.1, 712.5, 953.4, 981.2, 1121.9, 1135.5, 1424.8, 1455.8, 1465.3, 2928.2, 2993.7, 3019.4]
111	H-CH2CO	-166.27	4.60	[101.0, 122.9, 134.6, 210.8, 234.6, 354.1, 386.4, 527.3, 793.6, 906.9, 983.4, 1068.6, 1225.9, 1354.0, 1422.3, 3026.5, 3161.3]
111	CO-CH3	-166.73	4.15	[58.3, 65.3, 91.2, 197.3, 241.2, 259.6, 267.5, 411.6, 758.8, 782.1, 1143.4, 1415.7, 1426.9, 1740.2, 2997.6, 3100.7, 3148.7]
111	CHO-CH3	-170.09	4.36	[60.5, 81.6, 94.9, 132.3, 233.8, 323.3, 341.5, 464.6, 616.1, 755.8, 908.6, 1138.5, 1223.1, 1321.6, 1409.6, 1434.7, 2931.1, 2982.1, 3079.4, 3122.9]
111	H-CH3	-157.97	1.86	[12.0, 73.2, 161.3, 316.1, 459.7, 662.5, 771.3, 1091.8, 1325.6, 1426.8, 1438.3, 3014.7, 3129.0, 3143.0]
111	H-CH3CO	-171.05	3.40	[41.4, 58.4, 70.3, 113.2, 160.6, 188.4, 436.3, 489.9, 668.0, 900.2, 958.3, 1036.5, 1183.8, 1344.0, 1426.2, 1438.6, 1736.3, 2975.2, 3053.8, 3086.9]
111	H-CH3CHO	-175.13	2.90	[19.3, 74.4, 88.9, 132.2, 197.9, 212.1, 341.6, 490.1, 645.2, 890.7, 943.9, 1009.6, 1098.9, 1218.9, 1292.2, 1369.9, 1399.0, 1453.2, 1458.2, 2917.1, 2971.2, 3044.4, 3079.2]
111	H-CH3CH2O	-178.80	2.80	[12.0, 41.2, 57.4, 90.3, 143.6, 220.4, 278.7, 419.4, 546.3, 791.9, 847.7, 989.5, 1012.6, 1080.0, 1138.1, 1272.6, 1352.3, 1380.8, 1461.0, 1464.1, 1480.6, 2949.2, 2974.0, 2985.1, 3048.4, 3053.0]
111	O-H	-143.75	2.05	[178.9, 278.7, 394.1, 448.7, 926.1]
111	OH-H	-148.07	1.31	[76.5, 104.1, 272.4, 396.5, 497.6, 753.0, 939.6, 3657.4]

Table A2.3 Energy profile of Co/Cu(111).

Site	Species	Energies	Formation energy	Frequencies
gas	CO	-12.09	2.52	[14.0, 48.8, 2127.1]
gas	H2	-7.15	0.00	[75.2, 103.7, 4431.0]
gas	CH4	-23.26	0.00	[4.3, 1321.3, 1321.7, 1323.5, 1538.3, 1540.7, 3040.1, 3106.2, 3107.6, 3120.1]
gas	H2O	-12.81	0.00	[3873.6, 3758.0, 1623.8, 138.2, 105.4, 31.9]
gas	CH3OH	-27.75	1.18	[14.6, 30.6, 60.4, 292.1, 1004.5, 1062.3, 1150.3, 1351.1, 1455.5, 1476.5, 1487.8, 2947.3, 2999.7, 3075.9, 3775.6]
gas	CH3CHO	-35.42	2.47	[30.9, 59.2, 70.2, 163.2, 502.3, 756.6, 872.5, 1103.1, 1109.5, 1354.5, 1398.9, 1442.5, 1449.3, 1757.3, 2815.2, 2981.5, 3036.3, 3102.2]
gas	CH3CH2OH	-43.33	1.70	[0.5, 10.6, 99.6, 239.6, 288.5, 415.2, 807.9, 875.1, 1008.2, 1070.1, 1153.8, 1245.1, 1269.1, 1382.0, 1419.4, 1465.1, 1479.6, 1501.6, 2929.4, 2958.0, 2991.9, 3065.2, 3068.1, 3765.1]
111	H	-79.47	-0.39	[793.4, 797.5, 1043.3]
111	H2O	-88.46	-0.14	[12.0, 12.0, 12.0, 12.0, 47.9, 86.2, 1608.7, 3725.0, 3842.5]
111	O	-81.59	-0.42	[333.1, 359.8, 360.6]
111	OH	-85.41	-0.67	[247.2, 251.7, 377.6, 584.8, 592.2, 3716.9]
111	C	-82.81	1.66	[241.9, 492.5, 647.9]
111	CO	-89.24	0.89	[118.0, 126.4, 230.6, 239.9, 259.0, 1732.8]
111	COH	-92.30	1.40	[12.0, 130.9, 150.9, 347.4, 363.4, 424.3, 1072.7, 1200.9, 3620.3]
111	CHO	-92.14	1.56	[105.7, 171.0, 194.4, 321.4, 453.7, 612.4, 1192.0, 1220.1, 2899.7]
111	CH	-86.92	1.12	[12.0, 369.1, 615.8, 650.3, 716.2, 2981.5]
111	CH2O	-96.03	1.25	[113.9, 135.7, 270.5, 292.2, 401.8, 627.2, 866.3, 1106.8, 1146.4, 1454.7, 3005.6, 3109.3]
111	CHCO	-100.11	2.55	[115.1, 192.1, 223.1, 270.8, 295.1, 427.2, 731.3, 825.3, 949.7, 1223.9, 1470.3, 3300.9]
111	CHCHO	-104.00	2.24	[120.4, 185.6, 244.2, 309.4, 360.2, 408.5, 611.7, 733.2, 847.7, 958.8, 1159.9, 1200.1, 1335.5, 2943.8, 3053.8]
111	CHOH	-95.43	1.85	[138.5, 162.9, 263.8, 331.6, 396.7, 470.1, 614.9, 816.0, 1103.0, 1275.9, 2953.0, 3608.6]
111	CH2	-90.60	1.03	[12.0, 293.0, 324.0, 525.8, 654.5, 809.7, 1042.9, 2630.0, 3141.1]
111	CH3O	-100.53	0.33	[12.0, 12.0, 114.7, 133.1, 292.9, 532.6, 963.5, 1142.1, 1144.1, 1459.6, 1463.3, 1472.2, 2973.0, 3057.8, 3060.8]
111	CH2CO	-103.74	2.50	[120.0, 176.3, 224.2, 275.1, 316.3, 406.7, 556.9, 629.4, 839.2, 910.2, 1065.5, 1231.4, 1427.9, 3039.1, 3144.9]
111	CH2CHO	-107.97	1.84	[12.0, 161.0, 218.3, 240.9, 287.0, 433.8, 520.3, 538.5, 734.3, 892.8, 1026.5, 1102.3, 1178.2, 1364.0, 1440.3, 2733.1, 3052.9, 3219.2]
111	CH3	-94.63	0.57	[178.4, 192.3, 294.9, 388.8, 435.3, 456.3, 1196.9, 1339.9, 1348.2, 2807.1, 2860.7, 2885.1]
111	CH3OH	-103.44	0.99	[12.0, 12.0, 12.0, 44.9, 78.6, 272.1, 774.7, 876.2, 1011.1, 1232.3, 1333.5, 1431.0, 1475.7, 2153.6, 2883.2, 2985.0, 3525.2, 4608.2]
111	CH3CO	-107.92	1.89	[70.8, 110.1, 119.2, 126.6, 211.8, 242.4, 289.7, 562.6, 916.6, 936.2, 1047.2, 1253.8, 1350.3, 1434.5, 1437.8, 2960.0, 3027.6, 3078.1]
111	CH4	-98.88	-0.11	[12.0, 12.0, 12.0, 37.6, 49.3, 82.9, 1317.3, 1320.6, 1322.0, 1534.5, 1536.0, 2974.7, 3080.7, 3089.8, 3091.7]
111	CH3CHO	-111.36	2.03	[47.0, 54.5, 117.5, 159.4, 209.2, 262.5, 301.1, 519.7, 678.2, 881.3, 1003.8, 1079.2, 1176.9, 1314.5, 1368.5, 1446.1, 1447.1, 2833.8, 2947.9, 3022.1, 3073.9]
111	CH3CH2O	-116.26	0.71	[35.5, 83.5, 97.6, 199.0, 241.0, 278.7, 326.1, 480.7, 801.8, 843.7, 993.1, 1082.4,

				1144.8, 1275.0, 1356.1, 1386.1, 1460.9, 1466.3, 1483.4, 2968.4, 2977.9, 3012.4, 3054.2, 3057.5]
111	CH3CH2OH	-119.33	1.21	[12.0, 12.0, 47.9, 54.9, 111.2, 182.6, 259.5, 375.1, 436.8, 797.8, 832.5, 998.2, 1048.5, 1139.0, 1245.3, 1280.6, 1379.7, 1404.3, 1459.0, 1470.4, 1487.0, 2979.3, 2983.7, 3025.6, 3054.4, 3069.1, 3658.1]
111	H-CO	-91.97	1.73	[89.0, 161.7, 266.0, 333.9, 549.5, 1115.3, 1243.3, 2577.4]
111	CO-H	-91.24	2.47	[116.9, 176.1, 265.5, 296.6, 455.7, 531.6, 1263.7, 1425.2]
111	O-C	-87.16	2.97	[155.4, 305.0, 426.8, 598.8, 820.2]
111	O-CH	-91.59	2.11	[212.6, 249.3, 308.2, 383.1, 509.9, 719.3, 980.5, 3053.6]
111	H-CHO	-95.69	1.59	[177.1, 192.8, 252.2, 325.2, 536.2, 614.0, 893.3, 1126.4, 1242.2, 1758.2, 2983.3]
111	CHO-H	-94.71	2.57	[124.6, 167.0, 241.2, 258.0, 424.0, 591.6, 692.5, 978.8, 1108.6, 1211.4, 2918.0]
111	CO-CH	-99.65	3.01	[12.0, 188.4, 251.0, 271.6, 287.4, 415.6, 561.1, 715.9, 953.3, 1607.9, 3013.1]
111	CHO-CH	-103.18	3.06	[12.0, 12.0, 232.8, 329.8, 383.2, 424.4, 587.6, 683.1, 841.9, 1198.3, 1226.3, 1736.7, 2884.9, 3533.9]
111	H-CH	-90.30	1.32	[57.3, 329.3, 409.7, 671.1, 807.8, 919.0, 2009.4, 2586.4]
111	O-CH2	-95.18	2.10	[12.0, 149.8, 297.6, 390.6, 453.8, 564.7, 694.0, 968.5, 1353.2, 3009.3, 3087.1]
111	H-CH2O	-99.47	1.39	[121.4, 160.0, 215.8, 276.1, 311.6, 437.1, 877.4, 1005.8, 1180.4, 1203.4, 1453.7, 1748.7, 3004.9, 3094.4]
111	H-CHCO	-103.33	2.91	[12.0, 205.3, 268.3, 270.3, 281.0, 395.2, 585.5, 773.5, 835.7, 919.3, 1016.8, 1288.9, 1420.7, 3043.2]
111	CO-CH2	-103.46	2.78	[44.2, 124.0, 206.9, 323.6, 356.9, 412.3, 422.3, 520.3, 861.0, 914.9, 1300.2, 1825.6, 2831.6, 2894.3]
111	CHO-CH2	-107.08	2.74	[146.3, 200.6, 263.3, 307.1, 376.8, 477.0, 522.3, 568.1, 754.9, 811.2, 921.2, 1193.4, 1251.6, 1376.3, 2558.4, 2963.8, 2999.4]
111	H-CH2	-93.96	1.24	[187.7, 246.5, 308.3, 495.6, 512.7, 726.7, 906.7, 1407.7, 1807.9, 2490.9, 2998.2]
111	O-CH3	-99.12	1.73	[111.8, 142.4, 189.9, 250.1, 338.2, 344.3, 663.8, 825.2, 1115.0, 1389.2, 1409.0, 2962.2, 3133.6, 3212.7]
111	H-CH3O	-102.77	1.66	[12.0, 54.3, 89.5, 140.7, 187.1, 343.2, 584.0, 846.8, 970.7, 1125.3, 1136.9, 1431.2, 1456.2, 1464.0, 2943.5, 3014.4, 3025.7]
111	H-CH2CO	-107.17	2.65	[92.7, 172.0, 214.9, 284.1, 329.0, 388.9, 454.3, 648.5, 843.7, 936.0, 1046.1, 1082.5, 1182.3, 1442.4, 1770.5, 3032.8, 3123.4]
111	CO-CH3	-107.00	2.81	[97.1, 143.7, 162.4, 195.9, 278.5, 320.7, 333.4, 439.1, 781.0, 810.2, 1191.4, 1403.9, 1425.9, 1442.4, 2977.2, 3073.2, 3130.4]
111	CHO-CH3	-110.52	2.87	[112.4, 158.2, 174.7, 190.3, 311.9, 326.9, 381.9, 530.2, 675.9, 812.1, 971.1, 1099.6, 1199.6, 1267.3, 1405.4, 1424.9, 2895.6, 2986.7, 3029.6, 3100.4]
111	H-CH3	-97.78	0.99	[12.0, 75.0, 131.8, 354.9, 364.6, 692.7, 791.6, 1165.9, 1381.1, 1431.4, 1566.6, 2991.1, 3086.0, 3112.4]
111	H-CH3CO	-111.45	1.95	[86.8, 127.2, 152.5, 186.2, 232.0, 319.4, 423.7, 564.8, 691.5, 925.1, 984.8, 1073.4, 1192.8, 1362.3, 1440.7, 1446.7, 1737.4, 2972.4, 3044.4, 3087.1]
111	H-CH3CHO	-115.18	1.79	[80.2, 120.1, 154.5, 198.1, 225.1, 271.2, 344.6, 486.1, 528.7, 853.2, 999.8, 1064.5, 1090.6, 1184.5, 1343.4, 1382.7, 1449.8, 1452.2, 1743.4, 2969.7, 3012.9, 3044.2, 3068.0]
111	H-CH3CH2O	-118.60	1.95	[12.0, 55.3, 79.7, 140.3, 187.4, 243.0, 281.2, 431.2, 578.2, 794.9, 810.5, 982.0, 1072.6, 1116.7, 1179.3, 1276.1, 1360.5, 1388.9, 1459.1, 1466.3, 1481.1, 2982.3, 2987.5, 3032.7, 3056.6, 3066.2]
111	O-H	-84.20	0.54	[244.8, 277.5, 412.2, 477.4, 954.1]
111	OH-H	-87.70	0.62	[164.6, 205.1, 268.7, 336.8, 550.6, 563.0, 1032.0, 3611.6]

Table A2.4 Energy profile of Co_{2ML}/Cu(111).

Site	Species	Energies	Formation energy	Frequencies
gas	CO	-12.09	2.52	[14.0, 48.8, 2127.1]
gas	H2	-7.15	0.00	[75.2, 103.7, 4431.0]
gas	CH4	-23.26	0.00	[4.3, 1321.3, 1321.7, 1323.5, 1538.3, 1540.7, 3040.1, 3106.2, 3107.6, 3120.1]
gas	H2O	-12.81	0.00	[3873.6, 3758.0, 1623.8, 138.2, 105.4, 31.9]
gas	CH3OH	-27.75	1.18	[14.6, 30.6, 60.4, 292.1, 1004.5, 1062.3, 1150.3, 1351.1, 1455.5, 1476.5, 1487.8, 2947.3, 2999.7, 3075.9, 3775.6]
gas	CH3CHO	-35.42	2.47	[30.9, 59.2, 70.2, 163.2, 502.3, 756.6, 872.5, 1103.1, 1109.5, 1354.5, 1398.9, 1442.5, 1449.3, 1757.3, 2815.2, 2981.5, 3036.3, 3102.2]
gas	CH3CH2OH	-43.33	1.70	[0.5, 10.6, 99.6, 239.6, 288.5, 415.2, 807.9, 875.1, 1008.2, 1070.1, 1153.8, 1245.1, 1269.1, 1382.0, 1419.4, 1465.1, 1479.6, 1501.6, 2929.4, 2958.0, 2991.9, 3065.2, 3068.1, 3765.1]
111	H	-139.72	-0.34	[840.1, 840.8, 1045.2]
111	H2O	-148.76	-0.14	[12.0, 12.0, 12.0, 12.0, 24.0, 47.7, 1604.7, 3720.1, 3838.7]
111	O	-141.74	-0.27	[357.0, 358.5, 443.1]
111	OH	-145.55	-0.51	[246.8, 249.5, 377.0, 497.7, 506.0, 3740.3]
111	C	-142.70	2.07	[482.3, 489.0, 491.5]
111	CO	-149.24	1.18	[88.1, 106.1, 134.5, 137.7, 297.4, 1707.9]
111	COH	-152.23	1.77	[110.2, 140.4, 149.0, 352.9, 365.9, 418.2, 1078.7, 1192.0, 3615.9]
111	CHO	-152.23	1.77	[137.7, 167.7, 214.6, 289.1, 489.8, 687.2, 1184.3, 1217.4, 2915.2]
111	CH	-146.97	1.38	[390.6, 394.7, 532.0, 614.6, 616.5, 2979.7]
111	CH2O	-156.11	1.47	[75.1, 132.4, 265.0, 284.3, 366.4, 619.9, 872.9, 1118.8, 1146.1, 1459.6, 3002.2, 3103.2]
111	CHCO	-160.15	2.81	[111.9, 168.2, 209.9, 270.7, 337.6, 355.0, 527.4, 685.9, 937.7, 974.6, 1551.4, 3025.1]
111	CHCHO	-163.91	2.63	[98.7, 131.1, 225.0, 288.3, 319.4, 401.8, 631.0, 750.3, 876.6, 994.9, 1190.9, 1216.3, 1354.7, 2907.0, 3029.9]
111	CHOH	-155.46	2.12	[108.2, 131.5, 218.3, 317.1, 381.6, 449.0, 540.4, 859.8, 1109.9, 1276.5, 2929.5, 3612.0]
111	CH2	-150.62	1.30	[224.3, 266.5, 288.0, 476.1, 546.2, 637.8, 1406.5, 2535.8, 3005.1]
111	CH3O	-160.64	0.51	[12.0, 105.2, 110.5, 275.7, 283.8, 286.6, 970.7, 1140.1, 1145.2, 1438.8, 1464.6, 1465.9, 2966.8, 3049.9, 3051.3]
111	CH2CO	-163.63	2.91	[95.8, 163.4, 188.7, 240.9, 313.3, 410.7, 556.1, 607.8, 821.9, 922.7, 1070.7, 1254.5, 1429.9, 3038.1, 3145.3]
111	CH2CHO	-167.97	2.15	[81.3, 133.8, 197.9, 239.8, 279.3, 404.6, 525.3, 735.5, 811.8, 928.1, 955.6, 1126.4, 1195.1, 1353.6, 1402.1, 2802.3, 3054.3, 3096.7]
111	CH3	-154.95	0.54	[182.1, 192.5, 320.5, 383.7, 523.2, 526.0, 1199.8, 1358.5, 1360.5, 2823.8, 2883.1, 2891.2]
111	CH3OH	-163.74	0.99	[12.0, 12.0, 12.0, 16.0, 53.9, 67.2, 265.9, 1002.3, 1056.4, 1147.2, 1344.1, 1449.3, 1469.0, 1481.2, 2933.1, 2983.6, 3070.5, 3695.1]
111	CH3CO	-167.98	2.14	[68.3, 105.7, 124.3, 147.3, 217.1, 294.0, 335.1, 548.1, 914.5, 954.7, 1064.5, 1230.0, 1350.7, 1432.7, 1440.8, 2960.6, 3028.2, 3071.1]
111	CH4	-159.18	-0.11	[12.0, 12.0, 12.0, 12.0, 34.9, 53.5, 1314.3, 1318.3, 1319.6, 1531.6, 1533.0, 2972.7, 3072.7, 3092.6, 3093.9]
111	CH3CHO	-171.59	2.10	[12.0, 35.0, 56.2, 103.2, 116.3, 123.4, 153.0, 521.2, 767.7, 892.9, 1084.8, 1121.1, 1352.0, 1383.9, 1433.9, 1442.4, 1650.4, 2897.1, 2971.3, 3025.6, 3106.1]
111	CH3CH2O	-176.24	1.03	[12.0, 46.2, 66.3, 184.1, 225.5, 263.5, 302.2, 469.6, 799.1, 859.2, 1002.7, 1081.5,

				1141.2, 1272.0, 1355.7, 1384.2, 1459.9, 1466.0, 1482.4, 2959.4, 2976.2, 3000.5, 3050.7, 3056.5]
111	CH3CH2OH	-179.38	1.47	[12.0, 12.0, 12.0, 19.5, 39.0, 60.6, 229.9, 271.7, 413.0, 807.8, 869.8, 1008.3, 1066.8, 1151.2, 1244.5, 1271.6, 1381.4, 1418.3, 1462.1, 1474.9, 1499.5, 2930.8, 2960.4, 2983.8, 3058.1, 3059.4, 3749.2]
111	H-CO	-152.08	1.92	[12.0, 113.6, 173.0, 274.1, 569.3, 1123.4, 1330.8, 2612.1]
111	CO-H	-151.17	2.83	[115.1, 188.7, 281.4, 320.6, 390.3, 484.2, 1207.9, 1359.8]
111	O-C	-146.86	3.57	[129.5, 307.3, 394.0, 434.5, 586.0]
111	O-CH	-151.44	2.57	[159.4, 244.7, 276.3, 395.0, 524.9, 679.6, 944.8, 3076.4]
111	H-CHO	-155.71	1.87	[144.5, 191.3, 238.5, 305.5, 517.9, 583.4, 871.1, 1188.4, 1244.2, 1719.0, 2966.5]
111	CHO-H	-154.87	2.71	[93.6, 147.3, 218.3, 305.3, 422.7, 580.8, 676.2, 1105.0, 1178.4, 1197.3, 2736.4]
111	CO-CH	-159.60	3.36	[12.8, 142.2, 338.5, 365.7, 376.8, 452.1, 544.7, 581.1, 937.0, 1802.0, 3011.7]
111	CHO-CH	-162.87	3.67	[113.8, 186.4, 284.8, 338.9, 369.8, 514.1, 533.7, 570.6, 786.7, 914.0, 1245.9, 1346.6, 2913.3, 2999.7]
111	H-CH	-150.27	1.66	[250.3, 351.6, 389.1, 555.6, 619.7, 931.7, 1845.1, 3009.1]
111	O-CH2	-155.27	2.31	[163.4, 234.7, 296.3, 406.5, 426.2, 527.6, 726.2, 911.1, 1345.7, 2774.3, 3057.0]
111	H-CH2O	-159.53	1.62	[109.3, 154.6, 226.7, 273.5, 285.4, 415.4, 867.8, 1013.2, 1179.0, 1185.1, 1458.3, 1677.1, 2993.7, 3086.5]
111	H-CHCO	-163.27	3.27	[120.8, 165.7, 208.0, 266.2, 319.0, 366.0, 560.5, 759.1, 820.2, 940.7, 1009.7, 1309.2, 1498.9, 3047.5]
111	CO-CH2	-163.61	2.93	[51.1, 119.1, 213.6, 349.9, 372.6, 422.0, 451.4, 510.5, 848.7, 908.4, 1317.1, 1827.0, 2860.9, 2929.6]
111	CHO-CH2	-166.92	3.20	[87.1, 168.4, 243.9, 282.6, 348.0, 411.1, 469.1, 538.3, 720.3, 778.0, 881.3, 1243.7, 1269.3, 1338.6, 2761.4, 2927.3, 2972.3]
111	H-CH2	-154.03	1.47	[163.7, 234.0, 275.6, 334.9, 475.8, 700.9, 862.1, 1340.4, 1743.8, 2758.6, 2960.1]
111	O-CH3	-159.20	1.96	[82.8, 145.6, 167.6, 240.6, 331.1, 351.8, 638.2, 772.7, 1071.7, 1396.0, 1405.6, 2996.0, 3145.8, 3214.3]
111	H-CH3O	-162.94	1.79	[12.0, 48.9, 84.6, 174.7, 192.4, 305.5, 678.3, 950.9, 985.5, 1131.6, 1133.5, 1429.7, 1453.6, 1463.6, 2915.1, 2972.1, 3004.1]
111	H-CH2CO	-167.03	3.08	[87.2, 169.2, 191.8, 256.5, 308.1, 329.7, 438.1, 558.5, 831.7, 950.1, 1032.8, 1079.5, 1214.4, 1422.0, 1710.6, 3023.5, 3122.3]
111	CO-CH3	-167.18	2.94	[12.0, 85.6, 103.6, 174.8, 290.8, 302.5, 349.7, 459.3, 788.8, 813.5, 1192.9, 1405.0, 1420.6, 1709.8, 2953.5, 3063.2, 3127.2]
111	CHO-CH3	-170.58	3.11	[89.6, 144.3, 167.0, 199.8, 299.9, 315.8, 377.5, 532.0, 664.4, 793.5, 963.1, 1152.8, 1199.4, 1268.0, 1400.7, 1432.4, 2850.1, 2960.5, 3016.8, 3091.0]
111	H-CH3	-157.90	1.17	[12.0, 94.3, 134.1, 330.0, 440.6, 671.5, 778.5, 1154.4, 1390.8, 1434.1, 1595.8, 2986.9, 3080.6, 3105.2]
111	H-CH3CO	-171.48	2.21	[67.1, 115.9, 142.7, 158.0, 246.5, 303.5, 422.7, 555.3, 626.2, 936.9, 976.4, 1071.0, 1244.2, 1359.4, 1440.7, 1447.0, 1707.6, 2966.4, 3037.9, 3079.5]
111	H-CH3CHO	-175.24	2.03	[69.9, 110.4, 162.4, 195.7, 222.8, 249.4, 335.8, 481.2, 526.4, 866.0, 976.8, 1060.6, 1094.4, 1171.5, 1344.0, 1382.0, 1450.3, 1454.8, 1679.0, 2970.2, 3004.5, 3042.5, 3069.1]
111	H-CH3CH2O	-178.68	2.16	[12.0, 33.8, 62.1, 133.5, 175.2, 222.7, 277.0, 427.8, 616.2, 793.2, 829.3, 986.2, 1073.6, 1114.1, 1172.7, 1272.4, 1354.9, 1385.0, 1460.5, 1465.4, 1481.0, 2970.3, 2979.1, 3013.3, 3051.8, 3061.0]
111	O-H	-144.37	0.68	[259.5, 287.2, 423.3, 566.7, 1031.9]
111	OH-H	-147.87	0.75	[55.9, 113.0, 272.7, 321.0, 545.0, 571.8, 1117.8, 3631.4]

A3. Kinetic Assessment of Partially Segregated CoCu Catalysts for CO Hydrogenation

Table A3.1 Energy profile of CoCu/Co(111).

Site	Species	Energies	Formation energy	Frequencies
gas	CO	-12.09	2.52	[14.0, 48.8, 2127.1]
gas	H2	-7.15	0.00	[75.2, 103.7, 4431.0]
gas	CH4	-23.26	0.00	[4.3, 1321.3, 1321.7, 1323.5, 1538.3, 1540.7, 3040.1, 3106.2, 3107.6, 3120.1]
gas	H2O	-12.81	0.00	[3873.6, 3758.0, 1623.8, 138.2, 105.4, 31.9]
gas	CH3OH	-27.75	1.18	[14.6, 30.6, 60.4, 292.1, 1004.5, 1062.3, 1150.3, 1351.1, 1455.5, 1476.5, 1487.8, 2947.3, 2999.7, 3075.9, 3775.6]
gas	CH3CHO	-35.42	2.47	[30.9, 59.2, 70.2, 163.2, 502.3, 756.6, 872.5, 1103.1, 1109.5, 1354.5, 1398.9, 1442.5, 1449.3, 1757.3, 2815.2, 2981.5, 3036.3, 3102.2]
111	H	-202.28	-0.09	[706.4, 1051.1, 1271.7]
111	H2O	-211.76	-0.33	[102.3, 176.6, 248.2, 425.2, 526.2, 632.0, 1607.6, 3547.3, 3630.5]
111	O	-203.12	1.16	[295.7, 404.1, 503.1]
111	CO	-211.50	1.74	[100.3, 199.9, 351.1, 376.2, 462.8, 1910.1]
111	CHO	-214.48	2.34	[12.0, 12.0, 97.5, 220.8, 779.8, 1099.3, 1518.1, 2471.2, 3291.3]
111	CH	-209.70	1.46	[12.0, 12.0, 604.8, 728.1, 1213.9, 6181.7]
111	CH2O	-217.75	2.64	[135.6, 143.3, 158.8, 293.4, 329.5, 555.4, 1012.8, 1181.3, 1296.5, 1525.1, 3075.0, 3221.7]
111	CHCO	-208.89	2.27	[47.8, 166.2, 239.2, 285.8, 312.6, 414.7, 582.5, 627.1, 728.0, 1059.3, 1807.9, 3034.8]
111	CH2	-213.10	1.63	[12.0, 179.2, 446.7, 609.7, 700.2, 1002.8, 1376.9, 2825.2, 4179.8]
111	CH3O	-222.80	1.17	[159.9, 258.7, 271.7, 283.8, 312.1, 404.7, 910.5, 1137.7, 1142.6, 1455.1, 1463.8, 1475.8, 3012.6, 3104.9, 3163.2]
111	CH2CO	-212.38	2.35	[96.8, 151.2, 158.0, 219.2, 285.1, 329.3, 555.0, 611.9, 870.7, 913.9, 981.3, 1378.5, 1645.3, 3043.6, 3134.7]
111	CH3	-216.65	1.66	[150.6, 260.0, 317.4, 431.9, 631.2, 682.8, 1221.8, 1358.2, 1454.8, 2968.8, 3054.4, 3139.4]
111	CH3OH	-226.79	0.75	[59.8, 96.9, 117.4, 121.6, 147.7, 181.1, 298.3, 997.0, 1087.4, 1152.2, 1362.0, 1464.2, 1475.9, 1487.2, 2935.9, 3022.2, 3105.4, 3780.0]
111	CH3CO	-217.26	1.05	[12.0, 12.0, 12.0, 12.0, 12.0, 12.0, 444.3, 584.9, 872.8, 1036.5, 1165.9, 1277.5, 1627.1, 1934.0, 2363.3, 2988.1, 4057.2, 7218.6]
111	CH4	-222.10	-0.22	[67.9, 79.0, 88.7, 755.9, 926.1, 928.8, 1351.3, 1459.8, 1460.2, 3007.6, 3089.8, 3091.3]
111	CH3CHO	-221.20	0.69	[33.8, 70.0, 111.2, 126.1, 132.4, 154.6, 185.3, 526.3, 770.1, 909.7, 1096.2, 1133.7, 1357.7, 1395.1, 1428.3, 1445.6, 1660.7, 2954.0, 2964.4, 3030.4, 3109.9]
111	H-CO	-214.68	2.14	[12.0, 267.6, 339.4, 561.4, 744.8, 1122.6, 2865.3, 5287.3]
111	O-CH	-212.71	4.10	[208.0, 362.0, 431.9, 452.1, 623.2, 859.5, 961.1, 3107.2]
111	H-CHO	-217.13	3.26	[164.1, 184.9, 246.9, 320.4, 439.2, 760.3, 952.1, 1310.7, 1392.5, 1967.0, 2978.5]
111	CO-CH	-208.06	3.09	[59.1, 150.1, 354.8, 382.0, 428.3, 497.5, 608.8, 650.2, 978.0, 1836.3, 3034.2]
111	H-CH	-212.48	2.25	[394.0, 497.8, 645.3, 796.7, 911.3, 1315.4, 1980.0, 3029.4]

111	O-CH2	-216.89	3.50	[178.5, 207.3, 316.3, 469.8, 514.6, 696.7, 848.3, 1029.6, 1401.9, 2986.5, 3095.4]
111	H-CH2O	-221.10	2.87	[156.2, 177.6, 226.6, 315.9, 407.8, 511.0, 901.6, 1160.1, 1173.0, 1224.3, 1511.3, 1552.5, 3057.6, 3168.8]
111	H-CHCO	-211.98	2.75	[12.0, 162.6, 192.4, 291.4, 335.7, 410.9, 503.4, 635.5, 745.7, 932.9, 1202.8, 1653.6, 1823.9, 2999.6]
111	CO-CH2	-211.90	2.83	[86.9, 145.6, 232.3, 326.0, 383.4, 445.8, 526.9, 635.7, 804.1, 1011.6, 1396.3, 1864.6, 3033.6, 3107.3]
111	H-CH2	-216.06	2.25	[223.9, 448.3, 553.4, 630.5, 749.3, 924.1, 1044.2, 1427.7, 1687.7, 2992.0, 3020.1]
111	O-CH3	-220.86	3.11	[121.0, 176.9, 222.5, 251.8, 378.0, 441.6, 661.0, 783.5, 1110.8, 1386.9, 1423.9, 3073.6, 3215.4, 3219.7]
111	H-CH3O	-225.31	2.23	[104.8, 141.8, 207.0, 229.5, 270.6, 296.6, 779.4, 899.5, 1082.1, 1133.0, 1157.0, 1445.0, 1460.7, 1466.3, 3013.9, 3082.2, 3097.0]
111	H-CH2CO	-215.81	2.50	[12.0, 139.0, 186.8, 263.8, 283.0, 435.1, 582.7, 681.5, 820.8, 931.9, 943.7, 1081.4, 1374.2, 1495.0, 1664.1, 3040.4, 3139.0]
111	CO-CH3	-216.12	2.19	[98.0, 136.3, 166.7, 265.9, 283.1, 331.0, 380.4, 473.6, 768.3, 831.1, 1206.5, 1417.2, 1436.5, 1813.5, 3010.9, 3097.6, 3138.0]
111	H-CH3	-219.86	2.02	[124.7, 203.7, 252.7, 284.6, 654.9, 721.5, 965.8, 1196.1, 1351.9, 1434.5, 1488.2, 3013.2, 3114.1, 3144.7]
111	H-CH3CO	-220.23	1.65	[68.1, 122.8, 176.9, 205.9, 243.8, 292.3, 473.2, 575.1, 712.7, 929.0, 975.2, 1075.2, 1350.7, 1374.5, 1435.4, 1448.6, 1895.2, 2966.2, 3056.3, 3119.6]

Acknowledgments

First of all, I would like to acknowledge my supervisor, Prof. Dr. Felix Studt, for giving me the opportunity to work in his group. I learned a lot not only from his erudition but also from his personality. He is always kind-hearted, patient, and supportive. He is my role model. The past four years is the most important period in my life. I become more independent and mature. I believe I will benefit from this period for my whole life. Without my supervisor, none of these would be possible. I would like to show my most sincere appreciation to him.

I would like to thank Dr. Dmitry I. Sharapa for his guidance and helping me with calculations. I would like to thank Eduard Araujo and Amir Hakimioun, two contemporaries of mine as PhD student, for all the support and help. I would like to thank all my colleagues for creating such a nice working environment: Tiago Goncalves, Michal Fecik, Jonas Amsler, Lucas Spiske, Dr. Philipp Plessow, Dr. Jelena Jelic, Elisabeth Dietze, Philipp Huber, Sarah Bernart, Jiachen Chen, Thanh-Nam Huynh, and Claude Coppex. I would like to thank all the lovely people I met in Germany for making my stay a pleasant journey.

I also would like to thank the German Research Foundation for the financial support, and bwHPC (bwUniCluster and bwForCluster JUSTUS) for the technical support.

Finally, I would like to thank all my family members, especially, my mother and my little cousin for always being there for me.

Acronyms

ACSF	Atom-centered Symmetry Function
B3LYP	Becke, 3-parameter, Lee-Yang-Parr hybrid functional
BEEF	Bayesian Error Estimation Functional
BEP	Brønsted–Evans–Polanyi
DFT	Density Functional Theory
EDS	Energy Dispersive X-ray Spectroscopy
FT	Fischer-Tropsch
GGA	Generalized Gradient Approximation
IKFT	Institute of Catalysis Research and Technology
IS	Initial State
KIT	Karlsruher Instituts für Technologie
kMC	Kinetic Monte Carlo
LDA	Local Density Approximation
MAE	Mean Absolute Error
MC	Monte Carlo
PBE	Perdew-Burke-Ernzerhof functional
PES	Potential Energy Surface
PW91	Perdew-Wang 1991
RPBE	Revised Perdew-Burke-Ernzerhof functional
STEM	Scanning Transmission Electron Microscopy
TEM	Transmission Electron Microscopy
TPSS	Tao–Perdew–Staroverov–Scuseria functional
TS	Transition State
VASP	Vienna Ab initio Simulation Package
vdW	Van der Waals
VSSM	Variable Step-size Method
wACSF	Weighted Atom-centered Symmetry Functions
ZPE	Zero-point Energy

List of Publications

[1] **Zha, S.**; Sharapa, D.; Liu, S.; Zhao, Z.-J.; Studt, F. Modeling CoCu Nanoparticles Using Neural Network Accelerated Monte Carlo Simulations, submitted.

[2] **Zha, S.**; Sharapa, D.; Liu, S.; Zhao, Z.-J.; Studt, F. Insights into the Mechanism of CO Hydrogenation on Segregated CoCu Catalysts, in preparation.

[3] **Zha, S.**; Sharapa, D.; Liu, S.; Zhao, Z.-J.; Studt, F. Kinetic Assessment of Partially Segregated CoCu Catalysts for CO Hydrogenation, in preparation.

[4] Liu, S.; Zhao, Z.-J.; Yang, C.; **Zha, S.**; Neyman, K. M.; Studt, F.; Gong, J. Adsorption Preference Determines Segregation Direction: A Shortcut to More Realistic Surface Models of Alloy Catalysts. ACS Catal. 2019, 9 (6), 5011–5018.

[5] Liu, S.; Yang, C.; **Zha, S.**; Sharapa, D.; Studt, F.; Zhao, Z.; Gong, J. Moderate Surface Segregation Promotes Selective Ethanol Production in CO_2 Hydrogenation Reaction over CoCu Catalysts. *Angew. Chem. Intl. Ed.* **2022**, *61* (2).

Eidesstattliche Erklärung

Hiermit versichere ich eidesstattlich, dass ich die vorgelegte Dissertation selbständig angefertigt habe und keine anderen als die angegeben Quellen und Hilfsmittel benutzt habe. Die wörtlichen onder inhaltlich übernommenen Stellen wurden als solche kenntlich gemacht. Weiterhin habe ich die Satzung des Karlsruher Instituts für Technologie (KIT) zur Sicherung guter wissenschaftlicher Praxis in der gültigen Fassung beachtet und die Primärdaten gemäß Abs.A (6) gesichert. Die elektronische Version der Arbeit stimmt mit der schriftlichen überein. Die Arbeit wurde in gleicher oder anderer Form keiner anderen Prüfungsbehörde zur Erlangung eines akademischen Grades vorgelegt.

Karlsruhe, den 31.05.2022

Shenjun Zha